



Calhoun: The NPS Institutional Archive DSpace Repository

Theses and Dissertations

1. Thesis and Dissertation Collection, all items

1991-12

Acoustic Sensing of Ocean Turbulence

Coelho, Emanuel F.

Monterey, California. Naval Postgraduate School

<http://hdl.handle.net/10945/38241>

Downloaded from NPS Archive: Calhoun



<http://www.nps.edu/library>

Calhoun is the Naval Postgraduate School's public access digital repository for research materials and institutional publications created by the NPS community.

Calhoun is named for Professor of Mathematics Guy K. Calhoun, NPS's first appointed -- and published -- scholarly author.

Dudley Knox Library / Naval Postgraduate School
411 Dyer Road / 1 University Circle
Monterey, California USA 93943

(2)

NAVAL POSTGRADUATE SCHOOL

Monterey , California

AD-A246 752



DTIC
SELECTED
MARCH 3 1992
S D

THEESIS

ACOUSTIC SENSING
OF
OCEAN TURBULENCE

by

Emanuel Ferreira Coelho

December, 1991

Thesis Advisor:
Second Reader:

T.P. Stanton
E.B. Thornton

Approved for public release, distribution is unlimited

S 4 3 11 063

92-05249



REPORT DOCUMENTATION PAGE				Form Approved GMBN: 0704 0188				
1a REPORT SECURITY CLASSIFICATION Unclassified		1b RESTRICTIVE MARKINGS						
2a SECURITY CLASSIFICATION AUTHORITY		2b DISTRIBUTION AVAILABILITY OF ABSTRACT						
2b DECLASSIFICATION/DOWNGRADING SCHEDULE		Approved for public release, distribution is unlimited						
4 PERFORMING ORGANIZATION REPORT NUMBER(S)		5 MONITORING ORGANIZATION REPORT NUMBER(S)						
6a NAME OF PERFORMING ORGANIZATION Naval Postgraduate School	6b OFFICE SYMBOL (If applicable)	7a NAME OF MONITORING ORGANIZATION Naval Postgraduate School						
6c ADDRESS (City, State, and ZIP Code) Monterey, CA 93943-5000		7b ADDRESS (City, State, and ZIP Code) Monterey, CA 93943-5000						
8a NAME OF FUNDING/SPONSORING ORGANIZATION	8b OFFICE SYMBOL (If applicable)	9 DATES COVERS (Year Month Day) 10 PERIODICITY OF REPORT						
8c ADDRESS (City, State, and ZIP Code)		10a. REGULAR, IRREGULAR, OR SPECIAL <table border="1" style="width: 100%; border-collapse: collapse;"> <tr> <td style="width: 25%;">PERIODIC</td> <td style="width: 25%;">IRREGULAR</td> <td style="width: 25%;">SPECIAL</td> <td style="width: 25%;">NOT APPLICABLE</td> </tr> </table>			PERIODIC	IRREGULAR	SPECIAL	NOT APPLICABLE
PERIODIC	IRREGULAR	SPECIAL	NOT APPLICABLE					
11 TITLE (Include Security Classification) ACOUSTIC SENSING OF OCEAN TURBULENCE								
12 PERSONAL AUTHOR(S) Coelho, Emanuel F.								
13a TYPE OF REPORT Master's Thesis	13b TIME COVERED FROM _____ TO _____	14 DATE OF REPORT (Year Month Day) December 1991		15 APPROVAL NUMBER 130				
16 SUPPLEMENTARY NOTATION The views expressed in this thesis are those of the author and do not reflect the official policy or position of the Department of Defense or the U.S. Government								
17 COSAT CODES		18 SUBJECT TERMS (Continue on reverse if necessary and identify by block number) TURBULENCE MEASUREMENTS WAVE SPECTRA OCEAN FLUXES ACOUSTIC METHODS CURRENTMETERS REYNOLDS' CDV STRESSES						
19 ABSTRACT (Continue on reverse if necessary and identify by block number) The need for direct turbulence measurements in the upper ocean arise from widespread requirements to correctly parameterize momentum and scalar fluxes across the air/ocean interface. Until recently these observations were limited by a lack of instrumentation capable of measuring the fine-structure velocity field down to dissipation scales. The recently developed CDV package allows simultaneous sub-centimeter resolution measurements of temperature, conductivity, pressure, shear and the 3 component velocity field. As part of the development of this system a Monte-Carlo simulation was used to analyze the performance of several spectral estimators of the mean acoustic doppler shifts, from which the velocity components are derived. The selected algorithms were implemented on a digital signal processor allowing real-time estimation of the velocity, shear and scalar quantities.								
20 DISTRIBUTION AVAILABILITY OF ABSTRACT <input checked="" type="checkbox"/> UNCLASSIFIED UNLIMITED <input type="checkbox"/> SAME AS REPORT <input type="checkbox"/> DTIC USERS		21 APPROVAL NUMBER						
22a NAME OF RESPONSIBLE INDIVIDUAL T. P. Stanton		22b APPROVAL NUMBER 64-3144 OC/St						

19. ABSTRACT

To verify the performance of the CDV package, it was deployed off Wharf 2 in Monterey for 24 hours while simultaneously recording meteorological data. Reynold's stresses, buoyancy fluxes and fine scale stratification were characterized and the surface gravity wave field identified.

Approved for public release; distribution is unlimited.

Acoustic Sensing
of
Ocean Turbulence

by

Emanuel Ferreira Coelho
Lieutenant , Portuguese Navy
B.S., Portuguese Naval Academy

Submitted in partial fulfillment
of the requirements for the degree of

MASTER OF SCIENCE IN PHYSICAL OCEANOGRAPHY

from the

NAVAL POSTGRADUATE SCHOOL
December 1991

Author:

Emanuel Ferreira Coelho

Approved by:

T.P.Stanton, Thesis Advisor

E.B.Thorton, Second Reader

C.A.Collins, Chairman
Department of Oceanography



Accession For	
NTIS	NSA&I
DTI	NSB
Uncontrolled	<input type="checkbox"/>
J. Control	<input checked="" type="checkbox"/>
Distribution	
Availability Codes	
Dist	W.M. Polymer
Sp. Cont	
P-1	

ABSTRACT

The need for direct turbulence measurements in the upper ocean arise from widespread requirements to correctly parameterize momentum and scalar fluxes across the air/ocean interface. Until recently these observations were limited by a lack of instrumentation capable of measuring the fine-structure velocity field down to dissipation scales.

The recently developed CDV package allows simultaneous sub-centimeter resolution measurements of temperature, conductivity, pressure, shear and the 3 component velocity field. As part of the development of this system a Monte-Carlo simulation was used to analyze the performance of several spectral estimators of the mean acoustic Doppler shifts, from which the velocity components are derived. The selected algorithms were implemented on a Digital Signal Processor allowing real-time estimation of the velocity, shear and scalar quantities.

To verify the performance of the CDV package, it was deployed off Wharf 2 in Monterey for 24 hours while simultaneously recording meteorological data. Reynold's stresses, buoyancy fluxes and fine scale stratification were characterized and the surface gravity waves field identified.

TABLE OF CONTENTS

I.	INTRODUCTION	1
II.	MOTIVATION FOR MICROSTRUCTURE OBSERVATIONS	5
A.	REYNOLDS EQUATIONS	5
1.	Basic Governing Equations	6
2.	Reynolds Averaging	11
3.	Turbulent Closure	15
4.	Turbulence Kinetic Energy (TKE)	21
B.	MIXING LAYER ANALYSIS	24
C.	SPECTRAL DESCRIPTION OF TURBULENCE	29
III.	DOPPLER SPECTRUM ESTIMATION	34
A.	ESTIMATION OF A SINGLE COMPONENT COMPLEX SIGNAL SUPERIMPOSED ON GAUSSIAN WHITE NOISE	36
1.	Peak FFT	36
2.	Pulse Pair	38
3.	Zero Cross	39
4.	AR Modeling (Burg's method)	41
5.	Minimum Variance Method	42
6.	Multiple Signal Classification (MUSIC Algorithm)	44
B.	MONTE-CARLO SIMULATION	46

1. Discussion of Some Results	49
2. Conclusions	51
IV. THE CDV MICROSTRUCTURE PACKAGE	60
A. RECENT METHODS FOR TURBULENCE OBSERVATIONS . . .	60
1. Rapid Sampling Vertical Profiler (RSVP) . . .	60
2. Pulse to Pulse Coherent Sonar	61
3. Bistatic Acoustic Doppler Profiler	61
B. SPECIFICATIONS OF THE CDV SYSTEM	62
C. SIGNAL PROCESSING OVERVIEW	64
D. ACOUSTIC CHANNELS - VELOCITY ESTIMATIONS . . .	66
1. Doppler Velocities Estimation	66
2. Velocities on an Orthogonal Reference Frame	72
E. NON-ACOUSTIC DATA	73
F. CALIBRATION AND ERROR ANALYSIS	76
V. TURBULENCE OBSERVATIONS USING THE CDV PACKAGE . . .	84
A. WHARF #2 EXPERIMENT	84
B. METEOROLOGICAL DATA	87
C. CDV DATA	90
D. OCEAN FLUXES AND STRATIFICATION	92
VI. CONCLUSIONS	112
LIST OF REFERENCES	116

LIST OF FIGURES

Figure 3.B.1 - Monte-Carlo Simulation: Peak FFT algorithm, Bias and Variance plots.	52
Figure 3.B.2 - Monte-Carlo Simulation: Pulse Pair algorithm, Bias and Variance plots.	53
Figure 3.B.3 - Monte-Carlo Simulation: Zero Cross algorithm, Bias and Variance plots.	54
Figure 3.B.4 - Monte-Carlo Simulation: AR Model order 4 algorithm, Bias and Variance plots	55
Figure 3.B.5 - Monte-Carlo Simulation: MUSIC order 4 algorithm, Bias and Variance plots	56
Figure 3.B.6 - Monte-Carlo Simulation: MUSIC order 2 algorithm, Bias and Variance plots	57
Figure 4.C.1 - CDV Signal Processing overview.	67
Figure 4.D.1.1 - Scheme of a Bistatic 2 transducer system.	68
Figure 4.D.1.2 - Velocity projections scheme for a 2 transducers bistatic system.	70
Figure 4.D.2.1 - CDV Package, Orthogonal Reference Frame fixed to the instrument.	71
Figure 4.F.1 - Reciprocal Bistatic channels, doppler frequencies, received powers and bandwidth.	79
Figure 4.F.2 - Calibrated Temperature data. Simultaneous to the data shown in figure 4.F.1	80

Figure 4.F.3 - Reciprocal Bistatic channels, first differences histogram.	81
Figure 4.F.5 - Bistatic channels deglitching function. Whenever the difference curves go higher than the threshold curves, in the lower plot, that point was assumed as bad data.	82
Figure 4.F.4 - Reciprocal Bistatic channels, Scatter plots between first differences and received power.	83
Figure 5.A.1 - Wharf #2 Experiment set-up	85
Figure 5.B.1 - Wharf #2 Experiment: depth of the top of the CDV package at 2 August 1991.	88
Figure 5.B.2 - Wharf #2 Experiment: Wind stress and short wave radiation, from 1200 to 2000 at 2 Aug 1991.	90
Figure 5.C.1 - Wharf #2 Experiment: Velocity data, sampled at 44 Hz.	93
Figure 5.C.2 - Wharf #2 Experiment: Temperature data, sampled at 44 Hz.	94
Figure 5.D.1 - Wharf #2 Experiment - Spectral evolution of temperature.	95
Figure 5.D.2 - Wharf #2 Experiment - Spectral evolution of u-velocity.	96
Figure 5.D.3 - Wharf #2 Experiment - Spectral evolution of v-velocity.	97
Figure 5.D.4 - Wharf #2 Experiment - Spectral evolution of w-velocity.	98
Figure 5.D.5 - Wharf #2 Experiment - High resolution	

spectra at 15:30.	99
Figure 5.D.6 - Wharf #2 Experiment - Time evolution of the co-spectrum, between temperature and vertical velocity	102
Figure 5.D.7.a - Wharf #2 Experiment - Time evolution of the co-spectrum, between horizontal velocity components	103
Figure 5.D.7.b - Wharf #2 Experiment - Time evolution of the co-spectrum, between u and w velocity components	104
Figure 5.D.7.c - Wharf #2 Experiment - Time evolution of the co-spectrum, between v and w velocity components	105
Figure 5.D.8 - Wharf #2 Experiment - Phase spectra between velocity components and temperature at 15:30.	109
Figure 5.D.9 - Wharf #2 Experiment - Coherence of velocity components and temperature at 15:30.	109
Figure 5.D.10 - Wharf #2 Experiment - Horizontal fluxes of temperature at 15:30.	111

I. INTRODUCTION

Turbulence is a feature of flows and is characterized by its irregularity or randomness, diffusivity, large Reynolds numbers (highly nonlinear) and by three-dimensional vorticity fluctuations. Turbulent flows are also dissipative, requiring a continuous supply of energy, and limiting the smallest scales to be far larger than any molecular length scale. The smallest scale occurring in turbulent flows is called the Kolmogorov length scale [Ref.1]. These characteristics make any deterministic approach to the description of turbulent flow impossible, and observations very difficult. On the other hand, statistical approaches to the equations of motion lead to an unresolved system, requiring extra assumptions in order to obtain closure [Ref.2].

In order to characterize turbulence, we need to perform measurements of mean quantities and of fast varying quantities, requiring high spatial resolution, fast response sensors and stable observation platforms. A classical approach to separating mean quantities from turbulent fluctuation, is to assume a spectral gap, so that by using a running mean we are able to isolate perturbations from the mean flow (Reynolds averaging) [Ref.2].

A more complex procedure is required if one wants to separate a linear wave field from superimposed turbulence

[Ref.3 and Ref.4]. One method is just to subtract, from the fast varying variables, the components that are coherent to the wave field. The cross spectral variables and its coherency are used to identify the wave components and the correspondant frequency ranges. This method will only demodulate superimposed turbulence from the wave field assuming that no energy is being transferred (linear approach), and non-linear interaction between the two fields are not identified.

Turbulence velocity observations are frequently limited by a lack of instrumentation capable of measuring the fine-structure temperature, salinity and velocity field, down to dissipation scales. The CDV package recently developed at the Naval Postgraduate School allows simultaneous sub-centimeter resolution measurements of temperature, conductivity, pressure, shear and the 3 component velocity field. These concurrent high resolution ocean microstructure measurements will aid our understanding of a range of phenomena that requires the determination of momentum or scalar fluxes. Unresolved problems include layer stability characterizations, turbulent closure problems, dissipation and energy cascade estimations, observation of entrainment and turbulence development, air-sea interaction, and the superposition and coupling of turbulence to mean advection and/or wave fields.

As part of this work, real time signal processing programs, programed in C environment are developed, for the CDV package. This work is focused in creating and implementing

algorithms that estimate mean doppler shifts, from which the velocity components are derived; on the real time processing and filtering of the analog variables, including temperature, conductivity and shear; and on the continuous real time graphical monitoring of selected variables. Also, using a Monte-Carlo simulation, the performance of several spectral estimators of the mean acoustic doppler shifts are analyzed to guide the real-time processing algorithm choice.

The CDV package, after being tested and calibrated, was deployed on the 2 and 3 August 1991, in shallow water off a Wharf in Monterey to test its ability to measure momentum and scalar fluxes. It was fixed to a 2 meter high bottom mounted tripod, with the instrument facing the surface at depths of the order of 0.5 meters, while simultaneously recording meteorological data. Small swell, weak winds and overcast sky were observed throughout the observation period.

A procedure is developed that allows the estimation of Reynolds stresses and buoyancy fluxes based on the measured quantities. Spectral methods are used to characterize which part of the observed scalar variance fields are turbulent v.s. advected by the surface gravity wave field.

This thesis is organized as follows. Chapter II summarizes the theoretical background and motivations for microstructure observations. Chapter III describes a series of Monte-Carlo simulations that study the performance of several spectral estimators for the mean acoustic doppler shifts used to

estimate velocities. Chapter IV describes some recent methods and equipment that led to the development of the CDV package; the CDV package; the signal processing developed algorithms; and some validation tests and error analysis performed with real data. Chapter V describes the Monterey Wharf #2 experiment presenting the Reynolds stresses and ocean fluxes estimation procedures. Finally chapter VI presents some conclusions and recommendations for future work.

II. MOTIVATION FOR MICROSTRUCTURE OBSERVATIONS

Microstructure measurements are required for oceanography problems such as the study of mixing parameterizations, dissipation and energy cascade, surface layer entrainment, air-sea interaction and coupling, upwelling systems and mixing layer models. This chapter will introduce some theoretical background to ocean turbulence emphasizing the experimental needs.

A. REYNOLDS EQUATIONS

The dynamics and thermodynamics of the ocean are described by a set of non-linear basic governing equations containing time and space derivatives requiring the definition of initial and boundary conditions [Ref.5]. Usually we do not have enough information to solve these conditions at smaller scales, so we must choose a cut-off eddy size below which we include only the statistical effects of these smaller scales. The resulting non-linear equations will be underdetermined with no analytical solution. Therefore, we are limited to approximations or numerical solutions after closing the system with additional assumptions [Ref.2].

1. Basic Governing Equations

The governing equations are the set of equations describing the general physical laws of fluid dynamics and their application to the particular case of ocean dynamics [Ref.6 and 2]:

a. Equation of State

This equation describes the thermodynamic state of water relating the several basic variables of density, pressure, temperature and salinity. A complete empirical relation in polynomial form is given, for example, by Millero et.al. 1980 [Ref.6]. However, this equation is difficult to handle and interpret. An approximation widely used is based on the fact that the water is nearly incompressible near the surface so that density changes of a constant volume are only due to temperature or salinity changes (Brian and Cox 1972) [Ref.5],

$$\rho = \rho_0 \times [1 - \alpha \times (T - T_0) + \beta \times (S - S_0)]$$

where $\alpha = 2139 \times 10^{-7} \text{K}^{-1}$ is the thermal expansion coefficient and $\beta = 0.751 \times 10^{-3}$ is the salinity expansion coefficient and $\rho_0 = 1025.96 \text{ kg/m}^3$ is the density correspondent to the temperature $T_0 = 15^\circ\text{C}$ and salinity $S_0 = 35 \text{ psu}$ [Ref.5].

b. Conservation of Mass (continuity)

The conservation of mass for fluids, also called the continuity equation, states that the local rate of change of density is equal to minus the mass divergence, or:

$$\frac{\partial \rho}{\partial t} + \frac{\partial}{\partial x_j} (\rho U_j) = 0$$

If the fluctuations of density are much smaller than the mean density it can be shown that the incompressibility assumption is valid and this equation becomes:

$$\frac{d\rho}{dt} = \frac{\partial U_j}{\partial x_j} = 0$$

i.e. non-divergent flow and constant density following the motion.

c. Conservation of Momentum

This balance describes Newton's second law of motion. If we assume that the vertical and horizontal scales are much smaller than the earth radius, this conservation law can be written using the tangent plane approximation [Ref.2]:

$$\frac{\partial U_i}{\partial t} + U_j \frac{\partial U_i}{\partial x_j} = -\delta_{ij}g - \epsilon_{ijk}f_c U_k - \frac{1}{\rho} \frac{\partial P}{\partial x_i} + \frac{1}{\rho} \frac{\partial \tau_{ij}}{\partial x_j}$$

$$\text{where: } \delta = \begin{cases} 1 & m = n \\ -1 & m \neq n \end{cases} \quad \epsilon = \begin{cases} 1 & mnq=123 \ 231 \ 312 \\ -1 & mnq=321 \ 213 \ 132 \\ 0 & \text{otherwise} \end{cases}$$

Water can be assumed to be a newtonian fluid so that:

$$\tau_{ij} = \mu \left(\frac{\partial U_i}{\partial x_j} + \frac{\partial U_j}{\partial x_i} \right) + (\mu_b - \frac{2}{3}\mu) \frac{\partial U_k}{\partial x_k} \delta_{ij}$$

where $\mu = 1.4 \times 10^{-3} \text{ kgm}^{-1}\text{s}^{-1}$ and μ_b are the molecular viscosity and the bulk viscosity respectively [Ref.2].

However if we assume that the fluid is incompressible and defining kinematic viscosity (ν) as $\mu/\rho = 1.4 \times 10^{-6} \text{ m}^2\text{s}^{-1}$ we obtain:

$$\frac{1}{\rho} \frac{\partial \tau_{ij}}{\partial x_j} = \nu \frac{\partial^2 U_i}{\partial x_j^2}$$

If we assume that the motion is shallow, we can neglect density changes associated with the mass of the fluid, though we must retain their effect on the fluid weight, and we can further simplify the equations of motion in the so called Boussinesq approximation [Ref.2]:

$$\frac{\partial U_i}{\partial t} + U_j \frac{\partial U_i}{\partial x_j} = -\delta_{ij} g \frac{\rho}{\rho} - \epsilon_{ijk} f_c U_k - \frac{1}{\rho} \frac{\partial p}{\partial x_i} + \nu \frac{\partial^2 U_i}{\partial x_j^2}$$

These equations represent the balance of the inertia and advection (LHS) by gravity, coriolis acceleration, pressure gradient and viscous stresses.

d. Conservation of Heat

The conservation of heat describes the first law of thermodynamics. If we neglect the change of internal energy due to viscous dissipation and assume incompressibility, it can be represented by:

$$\frac{\partial T}{\partial t} + U_j \frac{\partial T}{\partial x_j} = K_t \frac{\partial^2 T}{\partial x_j^2} + \frac{Q}{C_p}$$

where the left hand side represents the storage and advection of heat, $K_t=1\times10^{-7} \text{ m}^2\text{s}^{-1}/(\rho C_p)$ is the coefficient of thermal diffusivity, Q represents the rate of heat addition per unit mass by internal heat sources and $C_p=3990 \text{ J.Kg}^{-1}\text{K}^{-1}$ is the specific heat at atmospheric pressure and 15°C [Ref.5].

The term Q can be summarized by [Ref.2,5 and 6]:

$$Q = (1-\alpha) Q_s + Q_{bc} - Q_t - Q_h - Q_e + Q_v$$

where:

Q_s - short wave solar radiation (α = surface albedo)

Q_{bc} - net heat gain by long wave radiation

Q_b - net heat loss by long wave radiation

Q_h - net heat loss/gain by conduction

Q_e - net heat loss/gain by evaporation or condensation

Q_v - net heat loss/gain by advection

The terms Q_e and Q_h will only be significant at the surface and can be estimated by the aerodynamical bulk formulas, based on bulk meteorological measurements [Ref.2].

The term Q_v representing the heat associated with the mass transport is usually parameterized by an eddy diffusion coefficient of the form:

$$Q_v = K' \cdot z \frac{\partial^2 T}{\partial x_j^2}$$

The terms associated with the downward long wave and short wave radiation are more difficult to analyze. We must use empirical relations describing the penetration and absorption of radiation with depth as a function of wavelength.

Finally the heat loss by long wave radiation can be estimated using Steffans law where ($Q_e \propto T^4$).

e. Conservation of Salt

Because of the form of the equation of state used, a salinity budget must be introduced of the form:

$$\frac{\partial S}{\partial t} + U_j \frac{\partial S}{\partial x_j} = K_s \frac{\partial^2 S}{\partial x_j^2} + S_s$$

stating that the storage and advection of salt (LHS) must be balanced by the molecular diffusivity of salt and by the net salt gain/loss by internal sources.

The term S_s corresponds to the balance due to evaporation, precipitation and runoff effects.

2. Reynolds Averaging

The randomness found in the smaller scales of motion in a turbulent fluid makes a deterministic approach to solving these equations very difficult. If we assume that the energy at these scales is the superposition of a variety of small size, band limited eddies, we can separate these components from the other mean effects by averaging over a sufficiently large interval corresponding to a stationary low frequency energy spectral component. This concept presumes the existence of a spectral gap in the component variance spectra [Ref.2]. However, the presence of internal waves, surface gravity waves and many other phenomena, does not always allow us to assume the existence of this gap between forcing and dissipation frequency ranges. Nevertheless, we can assume that each variable is composed by a mean and a perturbed part, which averages out to zero. However, the turbulent part of the variance will have non-zero covariances with the other turbulent components.

Starting from the previous basic governing equations and after separating the mean and perturbed components and averaging, the resultant set of equations is:

1. equation of state

$$\bar{\rho} = \rho_0 \times [1 - \alpha \times (\bar{T} - T_0) + \beta \times (\bar{S} - S_0)]$$

2. conservation of mass (continuity)

$$\frac{\partial \bar{U}_i}{\partial x_j} = \frac{\partial u'_i}{\partial x_j} = 0$$

3. conservation of momentum

$$\frac{\partial \bar{U}_i}{\partial t} + \bar{U}_j \frac{\partial \bar{U}_i}{\partial x_j} = -\delta_{ik} g - \epsilon_{ijk} f_c \bar{U}_k - \frac{1}{\bar{\rho}} \frac{\partial P}{\partial x_i} + v \frac{\partial^2 \bar{U}_i}{\partial x_j^2} - \frac{\partial}{\partial x_j} (\bar{u}'_i \bar{u}'_j)$$

4. conservation of heat

$$\frac{\partial \bar{T}}{\partial t} + \bar{U}_j \frac{\partial \bar{T}}{\partial x_j} = K_e \frac{\partial^2 \bar{T}}{\partial x_j^2} + \frac{\bar{Q}}{C_p} - \frac{\partial}{\partial x_j} (\bar{u}'_j \bar{\tau}')$$

5. conservation of salt

$$\frac{\partial \bar{S}}{\partial t} + \bar{U}_j \frac{\partial \bar{S}}{\partial x_j} = K_s \frac{\partial^2 \bar{S}}{\partial x_j^2} + \bar{S}_s - \frac{\partial}{\partial x_j} (\bar{u}'_j \bar{s}')$$

The new terms introduced by this procedure are the divergences of momentum, temperature and salinity fluxes, and they represent the interaction between the mean and the perturbed flow. For these terms to be significant, we must have a large Reynolds number (R_e = advection terms / molecular viscosity terms), so that it is usual to neglect the viscosity terms in this set of equations. The set of equations represent an unresolved system of 7 non-linear equations with 22 unknowns and are known as the Reynolds equations.

Before looking for any type of solutions we first must close the system by finding prognostic equations for the new variables in the form of fluxes and variances, eventually reducing the number of unknowns. To obtain the forecast equations for the fluxes and variances we must first find prognostic equations for the perturbations. Following the procedure described in Stull, 1988 [Ref.2], this can be achieved by subtracting the Reynolds equations from the governing equations, resulting in the system:

$$\begin{aligned} \frac{\partial u'_i}{\partial t} + \bar{U}_j \frac{\partial u'_i}{\partial x_j} + u'_j \frac{\partial \bar{U}_i}{\partial x_j} + u'_j \frac{\partial u'_i}{\partial x_j} &= \\ = -\delta_{ij} g \frac{\rho'}{\rho} + \epsilon_{ij}, f_c u'_j - \frac{1}{\rho} \frac{\partial p'}{\partial x_i} + v \frac{\partial^2 u'_i}{\partial x_j^2} + \frac{\partial}{\partial x_j} (\bar{u}'_i u'_j) \end{aligned}$$

$$\frac{\partial T'}{\partial t} + \bar{U}_j \frac{\partial T'}{\partial x_j} + u'_{\cdot j} \frac{\partial \bar{T}}{\partial x_j} + u'_{\cdot j} \frac{\partial T'}{\partial x_j} = K_t \frac{\partial^2 T'}{\partial x_j^2} + Q' + \frac{\partial}{\partial x_j} (\bar{u}'_{\cdot j} T')$$

$$\frac{\partial S'}{\partial t} + \bar{U}_j \frac{\partial S'}{\partial x_j} + u'_{\cdot j} \frac{\partial \bar{S}}{\partial x_j} + u'_{\cdot j} \frac{\partial S'}{\partial x_j} = K_s \frac{\partial^2 S'}{\partial x_j^2} + S'_{\cdot s} + \frac{\partial}{\partial x_j} (\bar{u}'_{\cdot j} S')$$

In order to obtain equations for the reynolds stresses and for the scalar fluxes, the following procedure was developed by Stull, 1988 [Ref.2]:

1. Multiply the equations for a generic variable q' , by $u'_{\cdot k}$, and Reynolds' average.
2. Sum these resultant equations, obtained by Reynolds' averaging the perturbed momentum equations multiplied by $q'_{\cdot k}$.
3. Use the continuity balance to transform advective terms into flux form.
4. Neglect the coriolis terms and the pressure, radiation and molecular diffusion.

The resultant equations, are:

$$\begin{aligned} \frac{\partial \bar{u}'_{\cdot i} u'_{\cdot k}}{\partial t} + \bar{U}_j \frac{\partial \bar{u}'_{\cdot i} u'_{\cdot k}}{\partial x_j} &= - \bar{u}'_{\cdot k} \bar{u}'_{\cdot j} \frac{\partial \bar{U}_i}{\partial x_j} - \bar{u}'_{\cdot i} \bar{u}'_{\cdot j} \frac{\partial u'_{\cdot k}}{\partial x_j} - \frac{\partial}{\partial x_j} (\bar{u}'_{\cdot i} \bar{u}'_{\cdot j} \bar{u}'_{\cdot k}) \\ &+ \frac{g}{\rho} [\delta_{k,j} \bar{u}'_{\cdot i} \bar{\rho}' + \delta_{i,j} \bar{u}'_{\cdot k} \bar{\rho}'] + \frac{\bar{\rho}'}{\rho} \left(\frac{\partial \bar{u}'_{\cdot i}}{\partial x_k} + \frac{\partial \bar{u}'_{\cdot k}}{\partial x_i} \right) - 2\epsilon_{u_i u_r} \end{aligned}$$

$$\frac{\partial \overline{T' u'_i}}{\partial t} + \overline{U_j} \frac{\partial \overline{T' u'_j}}{\partial x_j} = - \overline{T' u'_j} \frac{\partial \overline{U_i}}{\partial x_j} - \overline{u'_j u'_i} \frac{\partial \overline{T}}{\partial x_j} - \frac{\partial}{\partial x_j} (\overline{T' u'_j u'_i}) \\ + \delta_{ij} \left(\frac{\overline{T' p'}}{\rho} \right) g + \frac{\overline{P'}}{\rho} \frac{\partial \overline{T'}}{\partial x_i} - 2 \epsilon_{u,T}$$

$$\frac{\partial \overline{S' u'_i}}{\partial t} + \overline{U_j} \frac{\partial \overline{S' u'_j}}{\partial x_j} = - \overline{S' u'_j} \frac{\partial \overline{U_i}}{\partial x_j} - \overline{u'_j u'_i} \frac{\partial \overline{S}}{\partial x_j} - \frac{\partial}{\partial x_j} (\overline{S' u'_j u'_i}) \\ + \delta_{ij} \left(\frac{\overline{S' p'}}{\rho} \right) g + \frac{\overline{P'}}{\rho} \frac{\partial \overline{S'}}{\partial x_i} - 2 \epsilon_{u,S}$$

As we can see, these equations do not close the system because they introduce new variables in the form of statistical third moments. If we proceed looking for prognostic equations for these third moments, they will introduce in a similar way fourth order type moments and so forth.

Therefore in order to be able to use these Reynolds equations additional assumptions must be used.

3. Turbulent Closure

If there was no turbulence and the statistical second moments of the Reynolds equations were negligible, they would form a closed system of equations describing the mean motion. This is typical of the deep ocean, where turbulence events are episodic and of a low mean level [Ref.6].

However, these second moments are generally not negligible on the upper layer of the ocean, where atmospheric fluxes can be strong. The upper layer, where the Reynolds stresses and other turbulent fluxes are important, is known as the turbulent ocean mixing layer. It is not necessarily equal to the well mixed upper layer of nearly constant density known as the remnant mixed layer [Ref.7]. Therefore, in this study, our closure problem is essentially a boundary layer problem where mixing processes and air-sea interactions take place.

In order to close the system of equations, we must first decide to what order we want to go to in our prognostic equations, and at that point parameterize the statistical moments based on known variables. Hence parameterizations are an important tool that rely essentially on observations of slow varying variables. However, a complete study of these parameterizations, to see how the observed variables relate to the fast varying ones and to validate the procedure, will involve the simultaneous observation at a wide range of scales. Until recently these type of observations suffered from a lack of instrumentation capable of providing a complete picture of the ocean microstructure, similar to those that exist for micrometeorology observations.

The turbulent closure approximation may be made to order 0, 1, 2, etc, depending on the highest order moment in the prognostic equations. Some theories only use a portion of

the available equations introducing what is known as the half-order closures.

Two major approaches of turbulent closures are used that are applicable at any order [Ref.2]. In local closure, we parameterize unknown quantities at one point by values or gradients of known quantities at the same point. It assumes that turbulence has a similar nature to molecular diffusion. This is like K-theory, where we assume the stresses are directly proportional to the mean shear. In the other approach, known as nonlocal closure, an unknown quantity at a particular point is parameterized by known quantities at many points in space. It assumes turbulence as a superposition of eddies transporting fluid and its properties, like an advective process. Examples of nonlocal first order closure like the Transient Turbulence Theory and the Spectral Diffusivity Theory are described in Stull, 1988 [Ref.2]. Usually higher order local closures and nonlocal closures yield more accurate results, but they do so by adding computational expense and complexity [Ref.2].

1. Local Zero-Order Closure

In this approach, no prognostic equations are retained, not even equations for mean quantities. Mean flow, temperature and salinity are parameterized directly as functions of space and time. Adimensional variables are usually defined for certain classes of problems.

2. Local Half-Order Closure

This closure scheme uses only a subset of the first moment equations. A variation of this method yield the so called Bulk Models, where temperature profiles are assumed to have a certain shape, exploring homogeneity in the mixing layer and using vertically integrated equations [Ref.8].

3. Local First-Order Closure

In this scheme we retain the prognostic equations for the mean quantities and we parameterize the statistical second moments (variances and cross-variances).

For a generic variable "l" one possible parameterization of its turbulent flux will be:

$$\overline{u' j l'} = -K_l \frac{\partial \bar{l}}{\partial x_j}$$

where K_l with units $m^2 s^{-1}$ is known as eddy viscosity for the velocity case and as eddy diffusivity coefficient for the scalar variables. This approximation is called K-Theory and frequently fails whenever large eddies are present or when there is not a dominant scale [Ref.2]. A useful interpretation of these approaches can be made by looking at analogies to the viscous stress expressions for Newtonian fluids. We can express the Reynolds stresses in terms of the shear, by substituting the molecular viscosity coefficient with an eddy viscosity coefficient, obtaining:

$$\tau_{reynolds} = \rho K_m \frac{\partial \bar{U}}{\partial z}$$

Since turbulent mixing is much more effective than viscosity, the eddy viscosity should be much greater than the molecular viscosity [Ref.2]. Also while molecular viscosity is a property of the fluid, the eddy viscosity is a property of the flow so that this coefficient should vary as turbulence level varies. Good parameterizations should rely on the Monin-Obukhov length scale, on the Richardson number (Ri) and on the stratification, as we can see in the examples presented in Stull, 1988 [Ref.2].

Another useful interpretation of this theory is the so called Mixing-Length Theory derived by Prandtl (1925) [Ref.2] for neutral conditions. If a turbulent eddy moves a water parcel upward by a distance z' and if we assume that there is no other mixing or changes on "l" within the parcel, then the perturbation of "l" can be written as:

$$l' = l_{surrounding} - l_{parcel} = - \left(\frac{\partial \bar{l}}{\partial z} \right) z'$$

similarly

$$u' = u_{surrounding} - u_{parcel} = - \left(\frac{\partial \bar{U}}{\partial z} \right) z'$$

In order to have upward motion we must have some vertical velocity w' . If turbulence is such that it can be assumed that

$$w' = c \cdot u' \quad \text{for} \quad \frac{\partial \bar{U}}{\partial z} < 0$$

$$w' = -c \cdot u' \quad \text{for} \quad \frac{\partial \bar{U}}{\partial z} > 0$$

where "c" represents a positive constant. Then we can define mixing length "Ml" as

$$Ml^2 = Cz^2$$

A vertical eddy flux of the scalar variable "l" will have the form:

$$\overline{w' l'} = -Cz^2 \left| \frac{\partial \bar{U}}{\partial z} \right| \left(\frac{\partial \bar{l}}{\partial z} \right)$$

$$= -Ml^2 \left| \frac{\partial \bar{U}}{\partial z} \right| \left(\frac{\partial \bar{l}}{\partial z} \right)$$

$$\text{so that } K_l = Ml^2 \left| \frac{\partial \bar{U}}{\partial z} \right|$$

Therefore K_l should increase as shear increases or turbulence increases and as the ability of turbulence to cause mixing increases. Finally a remark should be made about the

assumption of linear gradients valid only over small distances, noting that this theory is a small-eddy theory.

4. Turbulence Kinetic Energy (TKE)

TKE measures the intensity of turbulence and is directly related to the momentum, heat and salt transport through the mixing layer. Its balance is important in the physical interpretation of the fluxes that are present on the Reynolds equations, and in describing the physical processes that generate and maintain turbulence. The total kinetic energy per unit mass (KE) is given by:

$$KE = \sum_{j=1}^3 \frac{1}{2} u_j^2$$

using Reynolds averaging we can identify the following components on the mean KE:

$$\bar{k} = \sum_{j=1}^3 \frac{1}{2} \overline{U_j^2} \quad KE \text{ of the mean flow}$$

$$\bar{k} = \sum_{j=1}^3 \frac{1}{2} \overline{u_j'^2} \quad KE \text{ of turbulence (TKE)}$$

From the Reynolds equations we can obtain the budget for the KE of the mean flow on the form [Ref.2]:

$$\frac{\partial K}{\partial t} + \overline{U}_j \frac{\partial K}{\partial x_j} = -\bar{\rho} \cdot \overline{U}_j \frac{\partial}{\partial x_i} (\overline{u'}_j \overline{u'}_i) - \frac{1}{\bar{\rho}} \overline{U}_j \frac{\partial \bar{p}}{\partial x_j} - \bar{W}g + \overline{U}_i v \frac{\partial^2 \overline{U}_i}{\partial x_j^2}$$

Interesting features in this equation are the fact that Coriolis has no effect on the TKE, showing that it is only a redistribution term. Another important feature is the explicit form of the Reynolds stresses representing the transformation of energy between the large scales of the mean flow and the smaller scales of turbulence.

From the definition of potential energy (Φ) and by using the Reynolds averaging procedure we can obtain the following potential energy budget:

$$\frac{d\Phi}{dt} = \bar{W}g + \frac{1}{\bar{\rho}} \overline{w' \rho' g}$$

We can see from this budget that the scalar turbulent fluxes represent the transformation between the mean potential energy and turbulence.

After identifying the role of the Reynolds stresses and scalar fluxes it is important to see how they balance, interact and develop in time. This can be accomplished by establishing a TKE budget. Using the prognostic equations for the perturbations and using an analogous procedure to that which we used to obtain the prognostic equations for the

Reynolds stresses and scalar fluxes, we can obtain prognostic equations for the variances of the perturbed velocity components that yield the following TKE balance [Ref.2]:

$$\frac{\partial \bar{k}}{\partial t} + \bar{U}_j \frac{\partial \bar{k}}{\partial x_j} = \frac{g}{\bar{\rho}} \bar{w' p'} - \bar{u'_i u'_j} \frac{\partial \bar{U}_i}{\partial x_j} - \frac{\partial (\bar{u'_j k})}{\partial x_j} - \frac{1}{\bar{\rho}} \frac{\partial (\bar{u'_i p'})}{\partial x_i} - \epsilon$$

The LHS of the budget represents the storage and advection of TKE by the mean flow. This latter term is often assumed negligible by assuming homogeneous turbulence over the mixing layer.

The first term on the RHS represents the buoyancy production/consumption. Corresponds to the transformation of TKE into potential energy and vice versa. Usually it is positive during the day and negative during the night due to diurnal solar heating.

The second term represents the mechanical or shear production and is directly related to the Reynolds stresses, reflecting any energy sources due to stirring or mixing and the interaction with the kinetic energy of the mean flow.

The third term represents the eddy transport of TKE, acting as a source or loss whenever there is a convergence or divergence.

The fourth term represents the pressure correlation term, describing how TKE is redistributed by pressure perturbations. It is this term that is responsible for the

interaction of turbulence with internal or surface gravity waves. The small scale perturbations can be due either to waves or turbulence and from linear wave theory (u', p') represents energy flux or power; therefore we can expect interaction between these two phenomena to exist by sourcing, sinking and redistributing TKE.

The last term represents the viscous dissipation rate or the transformation of TKE into heat.

B. MIXING LAYER ANALYSIS

Mixed layer depth can be defined as the depth at which density increases by some predetermined amount above the surface value, while mixing layer depth can be defined as the depth at which the dissipation rate drops monotonically below some arbitrary small value [Ref.8]. This definition for mixed layer is useful for observational purposes, but do not reflect the depth range of mixing, i.e. the layer that is dynamically unstable. Static stability is a measure of the capacity for buoyant convection that is independent on the flow and based only on density profiles. Dynamic stability measures the tendency for mean flow to break into smaller scales, even under statically stable conditions [Ref.6]. While statically unstable flows become or remain turbulent, statically stable flows may be laminar or turbulent depending on many factors that can be interpreted based on the TKE balance.

We can view the dynamic stability in terms of a balance between the two different effects of stratification and shear whenever the inertia is much greater than the viscous effects (high R_e) and the reynolds stresses and scalar fluxes are significant. While stratification will tend to damp out any perturbation, the shear of the mean flow will tend to enhance perturbations by supplying the required energy.

A description of a mechanism for the dynamic generation of turbulence is summarized by Stull, 1988 [Ref.2] based on laboratory experiments. He describes the following sequence of events:

1. shear across a density interface (laminar flow)
2. a critical value of shear is reached and flow becomes dynamically unstable, generating gentle waves at the interface
3. waves grow in amplitude and eventually break
4. between waves crests lighter fluid entrains the denser one and patches of static instability results
5. this static instability combines with continuous dynamical instability causing each wave to become turbulent
6. turbulence at the interface causes mixing of the two different fluids (entrainment)
7. mixing can reduce shear below critical value and eliminate dynamical instability
8. if there is no continuous supply of energy to restore the shear, turbulence will decay and flow will become laminar again.

This conceptual model for generation of turbulence seems consistent, however due to the episodic and 3 dimensional nature of turbulent events in the ocean, observations of all the processes are very difficult to perform. Also the lack of microstructure instrumentation able to directly observe the velocity field is a major limitation on our understanding of these processes.

Usually we rely on nondimensional parameters to compare these factors, like the Reynolds number and the Richardson numbers. The Reynolds number compares the inertial and the viscous terms in the equations of motion, evaluated when the Reynolds stresses are more important than viscous stresses. This happens only when the non-linear effects are significant. For turbulence to exist, it is therefore necessary to have a high Reynolds number, but this by itself it is not a sufficient condition, because it makes no requirements about the supply of energy necessary for turbulence to persist.

The Richardson number compares the buoyancy production to the mechanical production terms of the TKE balance, and evaluates when the shear will be able to overcome stratification to allow dynamical instabilities to exist [Ref.2]. Usually we have high Reynolds numbers in the ocean; therefore, the Richardson number is the critical criteria to determine if the flow is turbulent or not.

The flux Richardson number is defined as [Ref.2]:

$$R_f = \frac{\frac{g}{\rho} (\overline{w'p'})}{(\overline{u'_i u'_j}) \frac{\partial U_i}{\partial x_j}}$$

For R_f less than zero we have static instability (hence turbulent) flows. R_f equal to zero corresponds to neutral flows. The critical conditions below which flows are turbulent is $R_f = 1$.

Using K-theory, we can parameterize the fluxes based on the mean shear and obtain the gradient Richardson number [Ref.2]:

$$R_i = \frac{\frac{g}{\rho} \frac{\partial p}{\partial z}}{[(\frac{\partial U}{\partial z})^2 + (\frac{\partial V}{\partial z})^2]}$$

The critical value below which laminar flows become turbulent is accepted as 0.25, while the critical value for turbulent flows to become laminar is 1 [Ref.2]. This hysteresis is due to the fact that, for turbulence to start, we need the instability and a trigger mechanism; while instabilities will start at R_i near 1, the trigger mechanism will only occur near $R_i = 0.25$ [Ref.2].

Because usually we are limited to discrete observations at a certain depth, the bulk Richardson number is defined as [Ref.2]:

$$R_t = \frac{g\Delta\bar{\rho}\Delta z}{\bar{\rho}[\Delta\bar{U}^2 + \Delta\bar{V}^2]}$$

This discretization will change the critical values but the same critical value of 0.25 is generally used.

From this discussion we can conclude that direct microstructure observations are very important on the characterization of the mixing layer. Mixing processes have a special importance in coastal processes, controlling the rate of cooling or warming of the surface waters and the dispersion or diffusion of other scalar quantities. The role of vertical turbulent mixing on the coastal upwelling systems is determinant in the characterization and understanding of these type of phenomena, as we can see in the paper by Brink (1980) [Ref.9]. Therefore mixing layer observations, are need in order to study: mixing layer deepening or entrainment; and air sea interactions, as we can see in the papers by Dewey et.al. and Moum et.al. [Ref.7 and 10], characterizing coastal eddies and the enhancement of ocean fronts by turbulent mixing, and in the paper by Uwe et.al., analyzing upwelling relaxations during the CODE experiment [Ref.11].

C. SPECTRAL DESCRIPTION OF TURBULENCE

The spectrum, defined as the Fourier transform of the autocorrelation function, gives a picture of how variance or energy is distributed over frequency or wavelength. An eddy of a certain wavenumber "k" can be defined as a linear superposition of the disturbances containing energy in the vicinity of "k" [Ref.1]. These eddies will be exposed to the strain-rate field of larger ones, and nonlinear interactions and consequent energy transfers are expected. As a result, the eddies will loose their identity within one or two periods or wavelengths.

The Fourier Transform is a decomposition into wave components of different wavelengths associated with the fourier coefficients. An eddy, however, has many fourier coefficients changing in time. Therefore more sophisticated transforms and a nonstationary approach should be used if we want to decompose the velocity field into individual eddies.

When analyzing the wavenumber spectra, i.e. how energy or variance is distributed in scale, we can expect to find contributions down to the sub-centimeter scales of dissipation, after which the mechanical energy is transformed into heat by viscous processes, and the energy drops down to zero [Ref.1]. If our data is not sampled below these scales the spectra will be aliased. Therefore to understand both momentum fluxes and dissipation we must measure a wide range of scales, including sub-centimeter dissipation scales.

a. Velocity Spectrum

Large eddies are affected by the mean flow, such that they have a steady anisotropy, whereas no permanent anisotropy is induced at an appropriately small scales. As the eddy size becomes smaller, we can expect that the strain-rate field becomes isotropic in a mean sense. This concept is called local isotropy and it can not exist if the Reynolds number is not large enough (at least 100 [Ref.1]). When local isotropy prevails, the time scales are much shorter than those of the mean flow, so that small eddies respond quickly to changing conditions. This area of the spectrum is called the equilibrium range and includes all high wavenumbers. In this area of the spectra the scales are too small to receive energy directly from the mean flow. Because energy is finally dissipated, the amount of energy arriving to this scale should correspond to the total energy being dissipated by viscosity. The smallest scale that can be reached on this range is called the Kolmogorov microscale defined as [Ref.1]:

$$\eta = \left(\frac{v^3}{\epsilon} \right)^{\frac{1}{4}}$$

where v is the kinematic viscosity coefficient and ϵ is the dissipation rate given by [Ref.1]:

$$\epsilon = 2 \cdot v \int_0^{\infty} k^2 \cdot S \cdot dk$$

and "S" is the observed velocity spectrum.

For small wavenumbers, viscosity is not important.

The important parameters to be considered are those relating transfer of energy from the mean flow to turbulence, and the energy transfer to the smaller scales. The area of the spectrum corresponding to the superposition of these scales with the Kolmogorov spectrum is often called the Inertial Subrange and exists only for large Reynolds numbers (bigger than 10^5). At this range, no energy is added or dissipated, so that the energy flux across each wavenumber is constant. It is characterized by a slope of $-5/3$ on a loglog plot and is scaled by dissipation. Therefore, from observed spectral estimates in this range, we can estimate the total dissipation.

Spectral estimates will depend only on the wavenumber and on the total dissipation. Using similarity theory [Ref.2], we can expect the spectral estimate to be:

$$S(k) = \alpha_k \cdot \epsilon^{2/3} \cdot k^{-5/3}$$

$$\text{where } \begin{aligned} [S] &= m^3 s^{-2} \\ [\epsilon] &= m^2 s^{-3} \\ [k] &= m^{-1} \end{aligned}$$

where α_k is known as the Kolmogorov constant with ranges from 1.53 to 1.68 [Ref.2, pp.390].

For time spectra of velocity, two cases should be considered. The Lagrangian time spectra related to the temporal evolution seen by an observer moving with the turbulent velocity fluctuations and the Eulerian spectrum related to the evolution at a fixed point where the mean velocity is zero. Their shape is usually different due to advection, but we can still define the inertial and equilibrium sub-ranges in a similar way.

b. Temperature Spectrum

The temperature spectrum is defined in a similar way to the velocity spectrum, and shows the same nonstationary character, with energy being added, dissipated and transferred between different scales. If the Reynolds number is high enough, there is also an equilibrium range, an inertial subrange and an inertial-convective subrange where the temperature fluctuations are simply convected and where the spectral transfer of temperature variance is constant. In certain cases when thermal diffusivity becomes important within the inertial sub-range and where viscosity is not yet important, there is a Inertial-Diffusive subrange; this occurs in fluids with small Prandtl number (ratio of kinematic viscosity to heat conductivity). For large Prandtl number fluids, like water, viscous effects occur first and then

thermal diffusive effects; therefore we can also define Viscous-Convective and Viscous-Diffusive subranges.

c. Batchelor Spectrum

The Batchelor spectrum corresponds to a theoretical shape of the wavenumber spectrum of the temperature gradient fluctuations for homogeneous, locally isotropic turbulence in a homogeneous fluid with a large Prandtl number [Ref.12 and 1]. It is defined by the temperature variance dissipation rate, molecular diffusivity and by the Batchelor wavenumber defined as:

$$k_b = (\epsilon v^{-1} D^{-2})^{\frac{1}{4}}$$

This wavenumber has been identified as the cutoff wavenumber [Ref.12].

The effect of stratification was studied by Dillon and Caldwell, 1980 [Ref.12], who proposed that its effect should be more noticeable in the low viscous-convective wavenumber ranges when turbulence is weak compared with stratification. One of the most important applications of this theoretical spectrum is the estimation of the kinetic energy dissipation rates from the spectral cutoff wavenumber, as we can find in the work of Dillon and Caldwell, 1980 [Ref.12].

III. DOPPLER SPECTRUM ESTIMATION

The bistatic velocity estimation that will be discussed in the next chapter, requires a fast but accurate doppler spectral estimator. This estimator must rely on a small number of data points and be reliable even for weak signals submerged in strong noise. Several spectral estimators will be analyzed and Monte-Carlo simulations performed in order to study their performances.

Spectral estimation corresponds to the estimation of a function that is, by definition, the Fourier Transform of the autocorrelation function. The performance of a spectral estimator should be based on how well we are estimating this function over a continuous range of frequencies [Ref.13].

The use of Spectral Estimators to detect the presence of signals superimposed in white random noise demands a trade off between detectability and confidence of the detected values. Usually confidence is obtained by dividing the whole data set into smaller subsets, estimating the spectrum of each subset and then averaging the ensemble of estimates. If we consider that each spectral estimate corresponds to 2 Fourier coefficients and therefore has 2 degrees of freedom, the ensemble average based on N subsets will increase the number of degrees of freedom to $2N$, improving the viability of the overall estimate. However the spectrum based on these subsets

will have less resolution and the spectral estimate will be a smoothed but more accurate version of the unsegmented one [Ref.14].

There are applications where we need only the behavior of the spectral estimator at a specific frequency or in a specific region, such as the frequency estimation of a sinusoidal signal superimposed in white noise. In this case, the smoothed version of the spectrum will be a poor estimator of the sinusoidal frequency as we are seeking a parameter estimation (and not spectral estimation), that involves different statistics [Ref.13].

The frequency estimator based on a finite number of data points represents an estimate of the true frequency that we would have if we had an infinite number of points. Therefore we need to characterize, in statistical terms, the behavior of these estimates. In this work, the Bias and Variance of the frequency estimates will be the statistics that we will use to compare the performance of several estimators.

Because determination of these statistics for a wide variety of algorithms is not analytically treatable, Monte Carlo simulations are used to obtain estimates of these statistics in terms of the Signal to Noise Ratio (SNR) of the input signal and of the record length used in the estimator. The results of this simulation will be used to determine the appropriate doppler frequency estimator, for the bistatic data stream.

A. ESTIMATION OF A SINGLE COMPONENT COMPLEX SIGNAL SUPERIMPOSED ON GAUSSIAN WHITE NOISE

1. Peak FFT

This approach can be interpreted as an estimation of the parameters of a single component sinusoidal signal of frequency f , superimposed in gaussian white noise, of the form [Ref.15]:

$$x(n) = A \exp(j2\pi fn + \Phi) + z(n)$$

where $z(n)$ corresponds to complex gaussian white noise and "A", " φ " and "f" (amplitude, phase and frequency), assumed constant but unknown, are the parameters to be estimated.

The probability distribution function (PDF) of $x(n)$ corresponds to a shift in the multivariate gaussian distribution function associated with the white noise, and has the form:

$$P(x-s) = \frac{1}{\prod^N \det(R_{zz})} \exp[-(x-s)^H R^{-1} z (x-s)]$$

where " R_{zz} " is the noise correlation matrix and " s " the sinusoidal signal. Since we are assuming white noise, " R_{zz} " will be a diagonal matrix. The sinusoidal signal can be represented by the vector:

$$\begin{aligned} s &= A \exp(j\Phi) [1 \exp(j2\pi f) \exp(j2\pi f2) \dots \exp(j2\pi f(N-1))]^T = \\ &= A \exp(j\Phi) e \end{aligned}$$

where \mathbf{e} is a vector containing the values of the complex exponential of frequency f , at the several values of n .

To obtain a maximum likelihood estimator (MLE), we need to find the maximum of the PDF, which will be equivalent to minimize the hermitian form:

$$S = (\mathbf{x} - \mathbf{s})^H (\mathbf{x} - \mathbf{s}) = (\mathbf{x} - \mathbf{A} \text{EXP}(j\Phi) \mathbf{e})^H (\mathbf{x} - \mathbf{A} \text{EXP}(j\Phi) \mathbf{e})$$

First, if we minimize in terms of the complex amplitude $\mathbf{A}_c = \mathbf{A} \text{EXP}(j\varphi)$, we obtain [Ref.15]:

$$A_c = \frac{\mathbf{e}^H \mathbf{x}}{\mathbf{e}^H \mathbf{e}} = \frac{1}{N} \sum_{n=1}^{N_x} x(n) \text{EXP}(-j2\pi f n)$$

which corresponds exactly to the discrete fourier transform of the data evaluated at f (assumed known in this case). Now if we substitute this expression into the hermitian form, we obtain:

$$S(A_c, f) = \mathbf{x}^H \mathbf{x} - \mathbf{A}_c \mathbf{x}^H \mathbf{e} = \mathbf{x}^H \mathbf{x} - \frac{1}{N} |\mathbf{e}^H \mathbf{x}|^2$$

to minimize this expression in terms of the frequency we need to maximize:

$$\frac{1}{N} |\mathbf{e}^H \mathbf{x}|^2 = \frac{1}{N} \left| \sum_{n=0}^{N-1} \mathbf{x}(n) \exp(-j2\pi f n) \right|^2$$

Therefore the MLE of the frequency will be the frequency where the square of the absolute value of the discrete fourier transform (periodogram) attains its maximum.

In this work, we used a 128 point FFT algorithm to estimate the periodogram where the peak frequency will correspond to the MLE estimator.

This procedure will limit our resolution to 7.8×10^{-3} of the sampling frequency, so an interpolating procedure should be used in order to increase the estimator resolution. Nevertheless this estimator suffers from the fact that, for a small number of points, discretization errors are highly emphasized and its performance degraded if one wants to obtain faster estimations.

2. Pulse Pair

Traditionally, the Pulse Pair algorithm is used to estimate the mean frequency of a time series with a single frequency component signal, which corresponds to the frequency of maximum energy [Ref.16]. It is based on a very simple and fast algorithm that has given accurate results even for data sets with a small number of points. However, white noise contamination will induce a deviation from the peak value toward the zero frequency as the SNR decreases.

The algorithm uses the direct evaluation of the phase from the autocorrelation function estimate. In this project only the phase of the first lag autocorrelation function was used and computed using a classical approach based on calculating covariances of two consecutive points averaged over the sequence length. Other valid correlation estimate methods could be used such as the Modified Covariance Method [Ref.15], which has the property of giving estimates without running out of the data set. It will be shown later, that this method is equivalent to an eigenvalue decomposition of an order 2 correlation matrix (MUSIC -order 2 fast algorithm).

Higher lag autocorrelation estimates can be used either to improve the estimates when the frequencies are much smaller than the sampling frequency, or to obtain more credible estimates. However this procedure may create problems with the uniqueness of the estimate, and will be limited by a lag, corresponding to the Nyquist rate of the highest frequency present on the detected signal, after which aliased frequency estimates occur [Ref.16].

3. Zero Cross

This method consists of the evaluation of a dominant frequency by the number of zero crosses or the number of sign changes on a zero mean time series. When working with complex signals, we must start by defining criteria for a zero cross. A point in the real domain corresponds to a line parallel to

the imaginary axis in the complex plane. Then using this generalization, we can define a zero cross (real) as the change of sign on the real components of the time series. On other hand, a point in the imaginary domain is a line parallel to the real axis in the complex domain; then a zero cross (imaginary) corresponds to a change in sign in the imaginary components of the time series. Therefore, we can define a complex zero cross as a change in sign either in the real or imaginary part between consecutive points; therefore the zero crosses can either be determined in the real or imaginary parts. To get a better estimate we can also average both estimates.

By itself, this simple method is highly sensitive to high frequency noise contaminations that will increase the number of zero crosses. This effect can be partially compensated by choosing a hysteresis after each cross in order to minimize the high frequency contaminations [Ref.17]. In order to apply this technique, we must know the maximum possible frequency that we can have in the signal after which no frequency will be detectable.

Another approach developed by B.Kendem [Ref.18] suggests the incorporation of low-pass filters and periodogram analysis to obtain more robust estimates. This procedure was not developed in the present analysis, though some interesting results may be obtained.

4. AR Modeling (Burg's method)

AutoRegressive (AR) modeling is one general class of parametric models that we can use to study time series when some previous information exists [Ref.15]. It is based on the assumption that the value of the record at a particular time is determined by a linear combination of P past values, where P corresponds to the model order, superimposed in white noise ($u[n]$), in the form:

$$x[n] = -\sum_{k=1}^P a[k] x[n-k] + u[n]$$

The model coefficients are usually determined based on the autocorrelation function of the series using any of the estimators (usually the modified covariance method gives the best results) by solving the YULE-WALKER equations.

Another method to compute the model coefficients is based on an extrapolation of the autocorrelation function that has maximum entropy, so that the effects of truncation (spectral smearing) are minimized [Ref.15]. The estimated coefficients are then computed based on this assumption directly using Lagrange Multipliers. This method is known as BURG'S technique and is the one that was used in the present study [Ref.15].

The spectral estimator will correspond to the z-transform of $x[n]$ evaluated on the unit circle, or:

$$P_{AR}(f) = H(z) \Big|_{z=e^{-j2\pi f}} = \frac{1}{f_s} \frac{\rho_w}{|A(f)|^2} = \frac{1}{f_s} \frac{\rho_w}{e_P^H(f) \underline{a} \underline{a}^H e_P(f)}$$

where f_s is the sampling frequency, $H(z)$ the z-transform of the signal $x[n]$, $A(f)$ the denominator polynomial of $H(z)$ after the transformation $z=\text{EXP}(-j \cdot 2 \cdot \pi \cdot f)$, \underline{a} the model coefficients in vector form, and ρ_w the noise power.

The spectral estimators will have singular points for a discrete type spectra (pure sinusoids) corresponding to zeros on the denominator of $H(z)$; therefore, in our case of only one pure complex sinusoid in white noise, we can just look for the frequency that will be closer to a singularity. This can be accomplished by looking for the zeros of the denominator of the general spectral estimation expression and choosing the one that is nearest to the unit circle. In this form, the frequency estimation will be totally determined by the AR model coefficients. This is the method we used for the AR dominant frequency estimation. Because of its complexity, we should expect this method to be computationally intensive, and the results will also depend on the root finder that we use.

5. Minimum Variance Method

This method introduced by Capon [Ref. 13] is also called the Maximum Likelihood Method. It will describe the distribution of variance over frequency, but the area under

this estimate will not correspond to the total variance [Ref.13]. Therefore it is not a true spectral estimator, but is particularly suitable for single frequency estimation. The algorithm computes the spectral estimates in accordance to the output power of a set of narrow band finite impulse response (FIR) filters whose bandwidth or resolution are dependent on the frequency in an adaptative manner (in comparison with the periodogram that has a fixed resolution). The filter coefficients are computed so that the output variance is minimum and its gain is 1 (no distortion). In fact we do not need to compute all these coefficients explicitly because the spectral estimators can be derived directly from the inverse autocorrelation matrix in the form [Ref.13]:

$$P_M(f) = \frac{1}{f_s} \frac{1}{\underline{\epsilon}^H(f) R^{-1} \underline{\epsilon}(f)}$$

where R corresponds to the Toeplitz autocorrelation matrix, that can be estimated in several forms. In the present work the modified covariance method was used.

It can be shown that it gives spectral estimates that, for a given order P, correspond to the average of the spectral estimates of the AR models of order 1 to P [Ref.13], so its performance should result in a smaller variance. Its resolution is between that obtained by the classical spectral estimators and by an equivalent AR model. Therefore, in order

to obtain the single frequency estimate, we just need to compute the maximum of the above expression. However, due to its complexity and dependence on the resolution used in the maximum value determination, we should expect this algorithm to be even more computational intensive than an equivalent order AR method.

6. Multiple Signal Classification (MUSIC Algorithm)

This algorithm is one of several that analyze the column space of the autocorrelation matrix into a signal subspace and an orthogonal noise subspace using a Singular Value Decomposition (SVD) [Ref.15]. This is accomplished by separating the matrix into its eigenvectors so that the eigenvectors with the N largest eigenvalues, span the signal subspace and the others the noise subspace, where N is the number of complex components of the signal.

This estimate, like the minimum variance method, is not a true spectral estimator because it does not preserve the total variance, however it will work as a discrete frequency parameter estimator. Its general expression is [Ref.15]:

$$P_{MUSIC}(f) = \frac{1}{\mathbf{e}^H(f) \left(\sum_{k=M+1}^P \mathbf{V}_k \mathbf{V}_k^H \right) \mathbf{e}(f)}$$

where M is the number of complex sinusoids in the signal and \underline{v}' are the eigenvectors that span the noise subspace (associated with the smaller eigenvalues).

The discrete signal components will be orthogonal to any linear combination of the eigenvectors that form the noise base, and so we could expect singularities at the signal frequencies. In reality, we will not have pure singularities but the spectral estimates will peak. For our purpose of estimating a single frequency component, the procedure used was based on finding the roots of the averaged noise space eigenvectors (taken as polynomials of the complex exponential), whose phases correspond to the peak frequencies. The eigenvector associated with the root closest to the unit circle is the single frequency estimator.

It can be proved that when we use an order 2 matrix in a single complex frequency component signal, the frequency estimator is equivalent to the Pulse Pair algorithm, and so the frequency estimate can be obtained directly from the autocorrelation function.

The autocorrelation function for a single complex component signal superimposed in white noise will have the form:

$$r_{xx}(k) = P \cdot \exp(j2\pi f \frac{k}{f_s}) + \rho_w \delta(k)$$

and the corresponding 2nd order autocorrelation matrix will be:

$$\begin{vmatrix} r_{xx}(0) & r_{xx}^*(1) \\ r_{xx}(1) & r_{xx}(0) \end{vmatrix}$$

The eigenvector associated with the smaller eigenvalue ($-\rho_w$) will be:

$$x_1 = \frac{1}{R(0)\sqrt{2}} \begin{vmatrix} R(0) \\ R(1) \end{vmatrix} = \frac{1}{\sqrt{2}} \begin{vmatrix} 1 \\ \exp(-j2\pi\frac{f}{f_s}) \end{vmatrix}$$

Therefore, the determination of the frequency estimate in this case will correspond to the determination of the phase associated with the first lag autocorrelation function estimate, as in the Pulse Pair estimator.

This analytical solution of the 2nd order eigenvalue problem was implemented for performance comparisons, and a singular value decomposition was used for higher orders. The Modified Covariance Method was used to estimate the autocorrelation matrix at any order.

B. MONTE-CARLO SIMULATION

To evaluate the performance of these spectral estimators for the estimation of the frequency of a complex sinusoid superimposed in complex independent gaussian white noise, a

MONTE CARLO simulation was built within MATLAB environment. This simulation is based on 50 independent trials where the BIAS, VARIANCE and a TIME INDEX are evaluated at each step.

The model has the input variables:

1. Signal to Noise Ratio (scalar or vector)
2. Number of Points (scalar or vector)
3. Signal Frequency (scalar or vector)
4. Type of Spectral Estimator

The model output variables are:

1. Bias
2. Variance
3. Time Index - proportional to the computation time
and are stored at each step.

The algorithm of the simulation program is as follows:

1.SELECT TECHNIQUE

- 1.Peak FFT
- 2.Pulse Pair
- 3.Zero Cross
- 4.Modified Prony's Technique
- 5.AR Model (burg algorithm)
- 6.MV (capon's method)
- 7.Music (eigenvalue decomposition)

2.SELECT PARAMETERS (increments,initial and final values)

- 1.Number points <-> SNR
- 2.Frequency <-> SNR

3.Frequency <-> Number Points

3.RUN MODEL

1. Initialize variables

trials=50

test frequency=20 Hz

sampling frequency=100 Hz

2. Main loop

generate noise

generate new frequency

generate signal

estimate frequency

compute estimate bias and variance

compute processing time

The complex independent gaussian white noise is generated by a function that uses different seeds for the real and imaginary parts at each step, in order to generate independent complex gaussian noise. Each noise component is then averaged from 5 different trials to obtain a pseudo gaussian noise. This number of 5 trials represents a compromise in the computation speed. The generated noise is normalized to guarantee a variance of 1.

Model runs using a 20 Hz signal, a sampling frequency of 100 Hz, over a -20 to 10 SNR and 16 to 128 points time series, were made for the following spectral estimators:

1. Peak FFT

2. Pulse Pair
3. Zero Cross
4. AR Model order 4
5. MUSIC order 4
6. MUSIC order 3
7. MUSIC order 2
8. MUSIC order 2/Pulse Pair (fast algorithm)

The selected plots of the bias and the logarithms of standard deviation are shown on the Figures 3.B.1-6.

1. Discussion of Some Results

The performance of an estimate can be assumed good when its bias is less than 1 Hz and the \log_{10} of the standard deviation is less than 0. Using this criteria the following tables show the SNR at which the bias of the several estimators is equal to 1 Hz, and the log standard deviation equal to 0:

TABLE 1 - SNR at BIAS = 1 Hz

Estimator	20 Points	40 Points	60 Points	80 Points
Peak FFT	-4	-5	-7	-8
Pulse Pair	-3	-8	-8	-8

Estimator	20 Points	40 Points	60 Points	80 Points
Zero Cross	0	0	0	0
AR Model (order 4)	-2	-4	-5	-7
MUSIC (order 4)	2	-2	-5	-4
MUSIC (order 2)	-5	-6	-5	-8

TABLE 2 - SNR at \log_{10} VARIANCE = 0

Estimator	20 Points	40 Points	60 Points	80 Points
Peak FFT	-3	-5	-7	-8
Pulse Pair	5	3	2	0
Zero Cross	5	4	3	2
AR Model (order 4)	8	0	-4	-5

Estimator	20 Points	40 Points	60 Points	80 Points
MUSIC (order 4)	10	5	2	2
MUSIC (order 2)	5	3	2	0

2. Conclusions

For all the estimators, after a sequence length (NP) between 20 and 64, the estimator variance becomes dependent only on the SNR. As a general rule except, for AR modeling, the variance is more restrictive than the bias. This means that we can get some improvement in the performance of this estimators if we take averaged measurements of the estimated frequency. The estimator that seems to work better for low SNR is the PEAK FFT followed by AR modeling (order 4), but AR modeling has poor processing time indexes (too slow). The MUSIC estimator is very sensitive to the noise contamination (SNR). The equivalent PULSE PAIR method and the MUSIC (order 2 fast algorithm) do not show any significant improvement by changing the AUTOCORRELATION estimators, at least between the two that were used in this program (biased and the modified covariance estimators [Ref.15]).

The fastest algorithm is the MUSIC (order 2 fast algorithm) at all sequences lengths followed by the PULSE PAIR

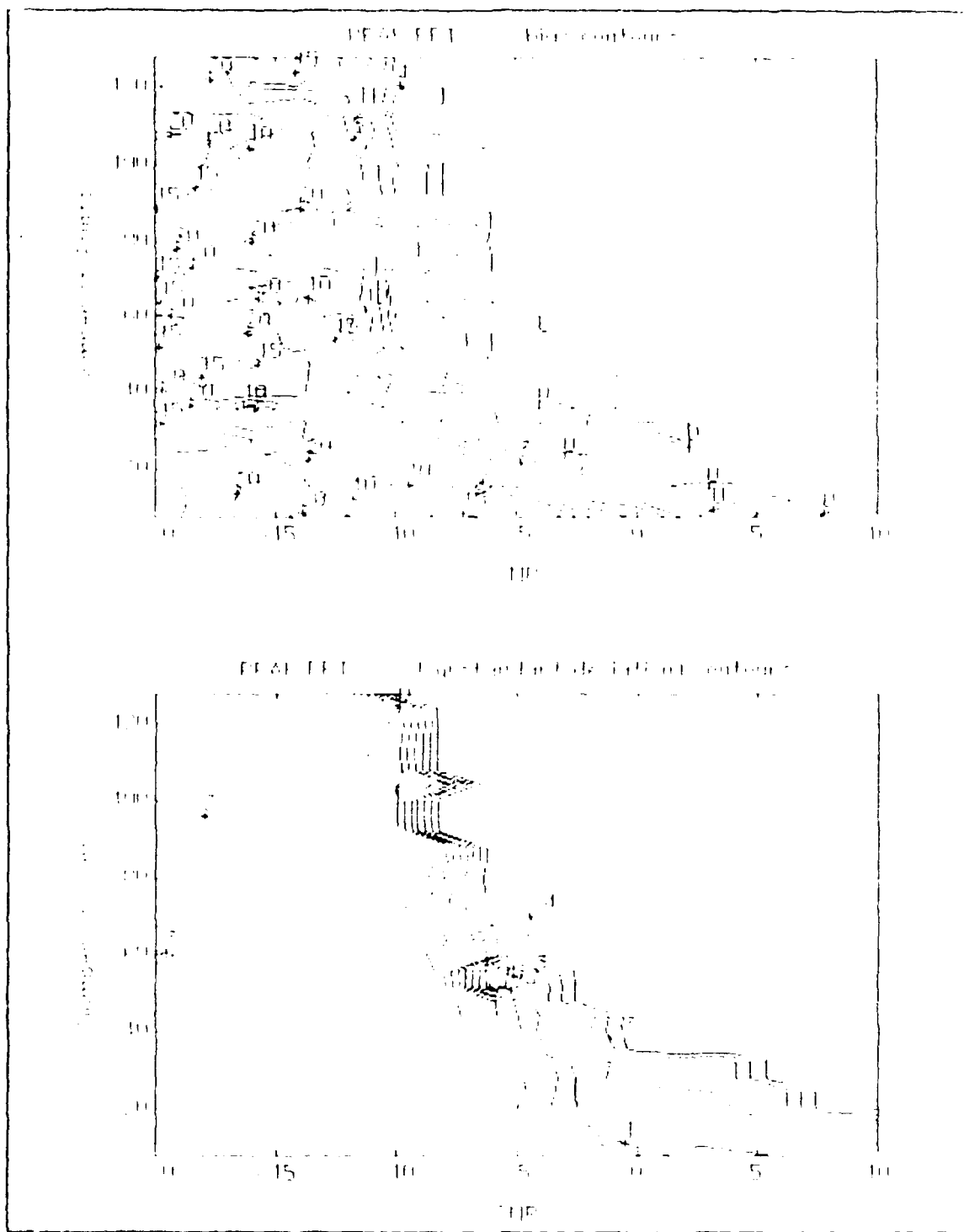


Figure 3.B.1 - Monte-Carlo Simulation: Peak FFT algorithm, Bias and Variance plots.

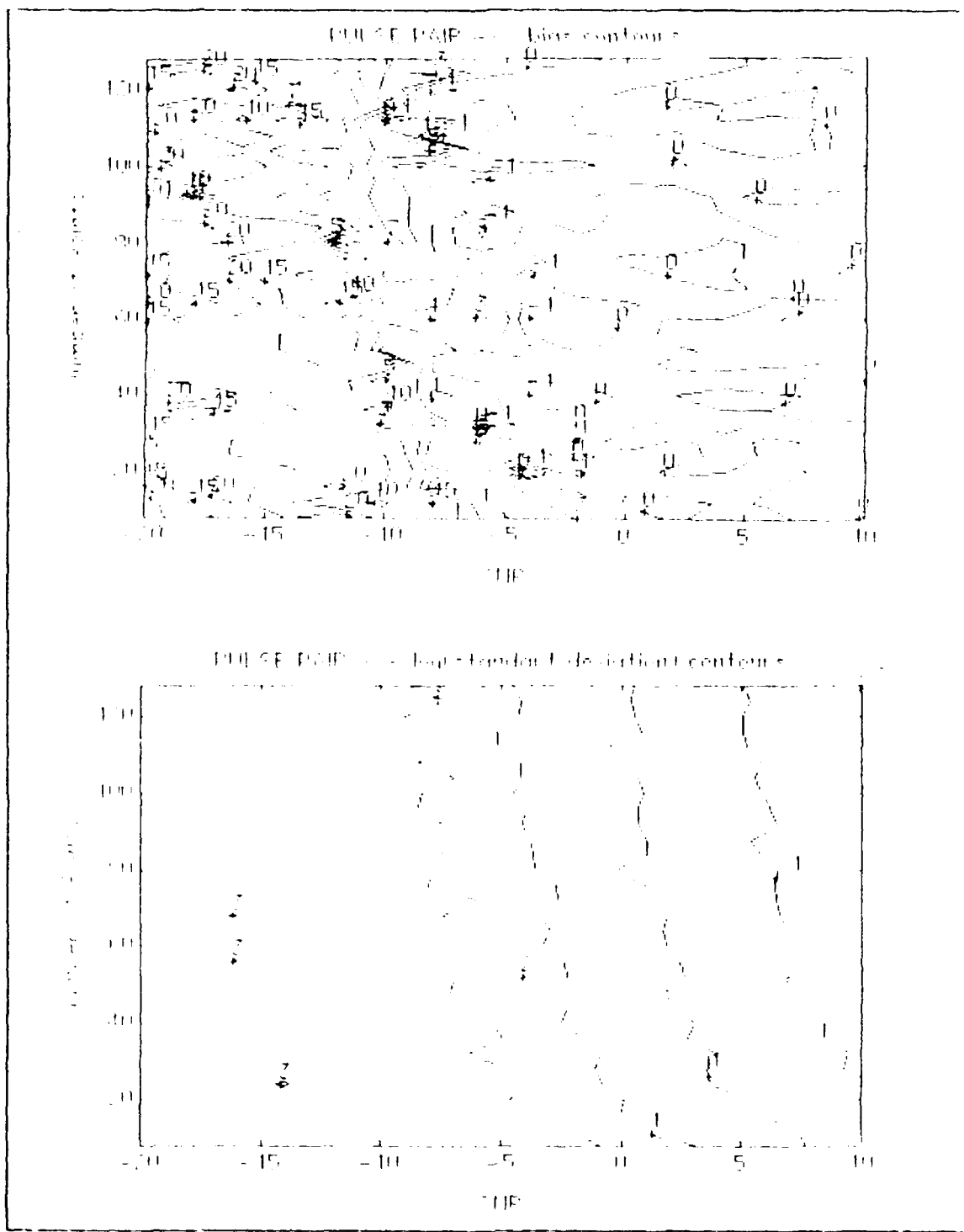


Figure 3.B.2 – Monte-Carlo Simulation: Pulse Pair algorithm, Bias and Variance plots.

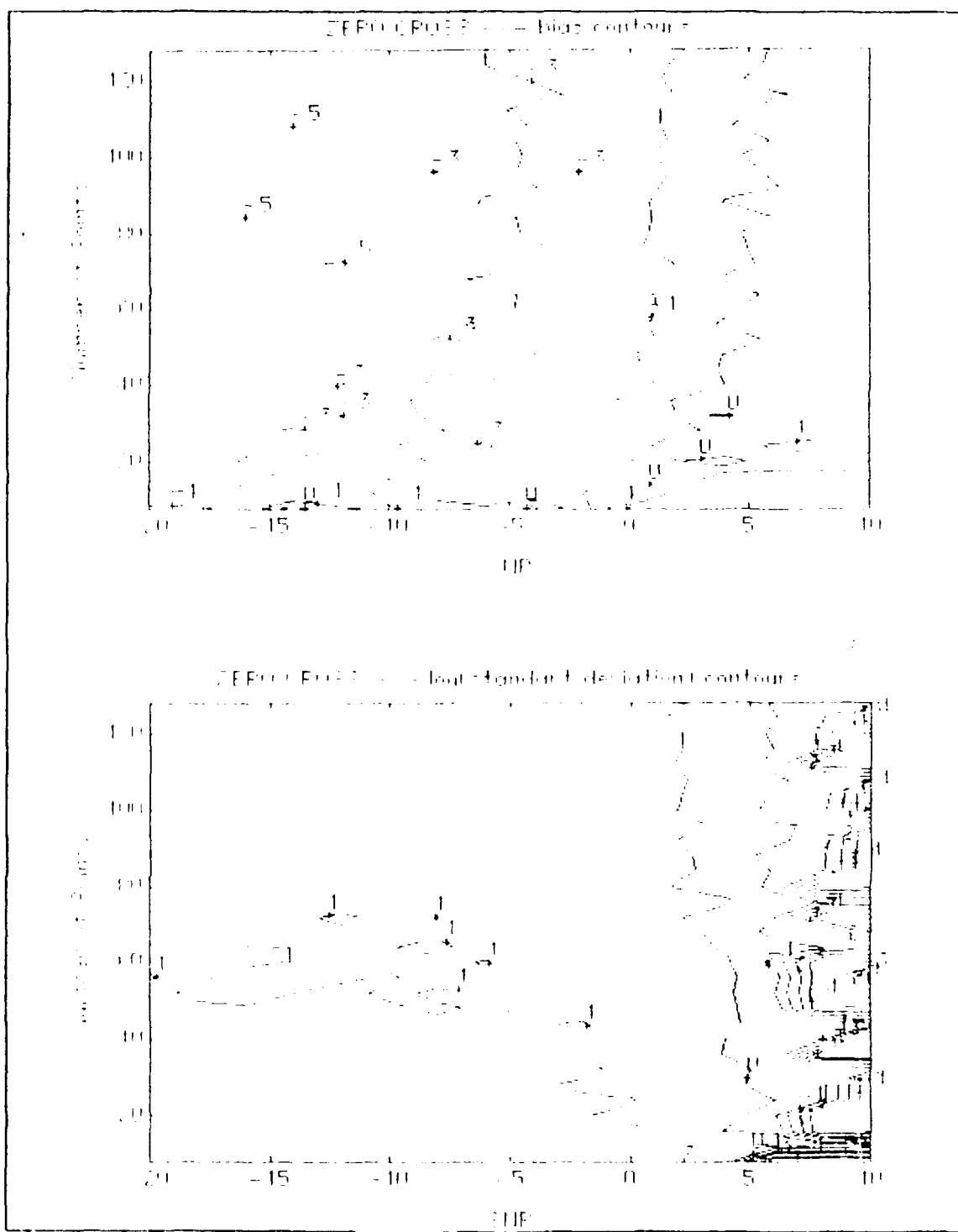


Figure 3.B.3 – Monte-Carlo Simulation: Zero Cross algorithm, Bias and Variance plots.

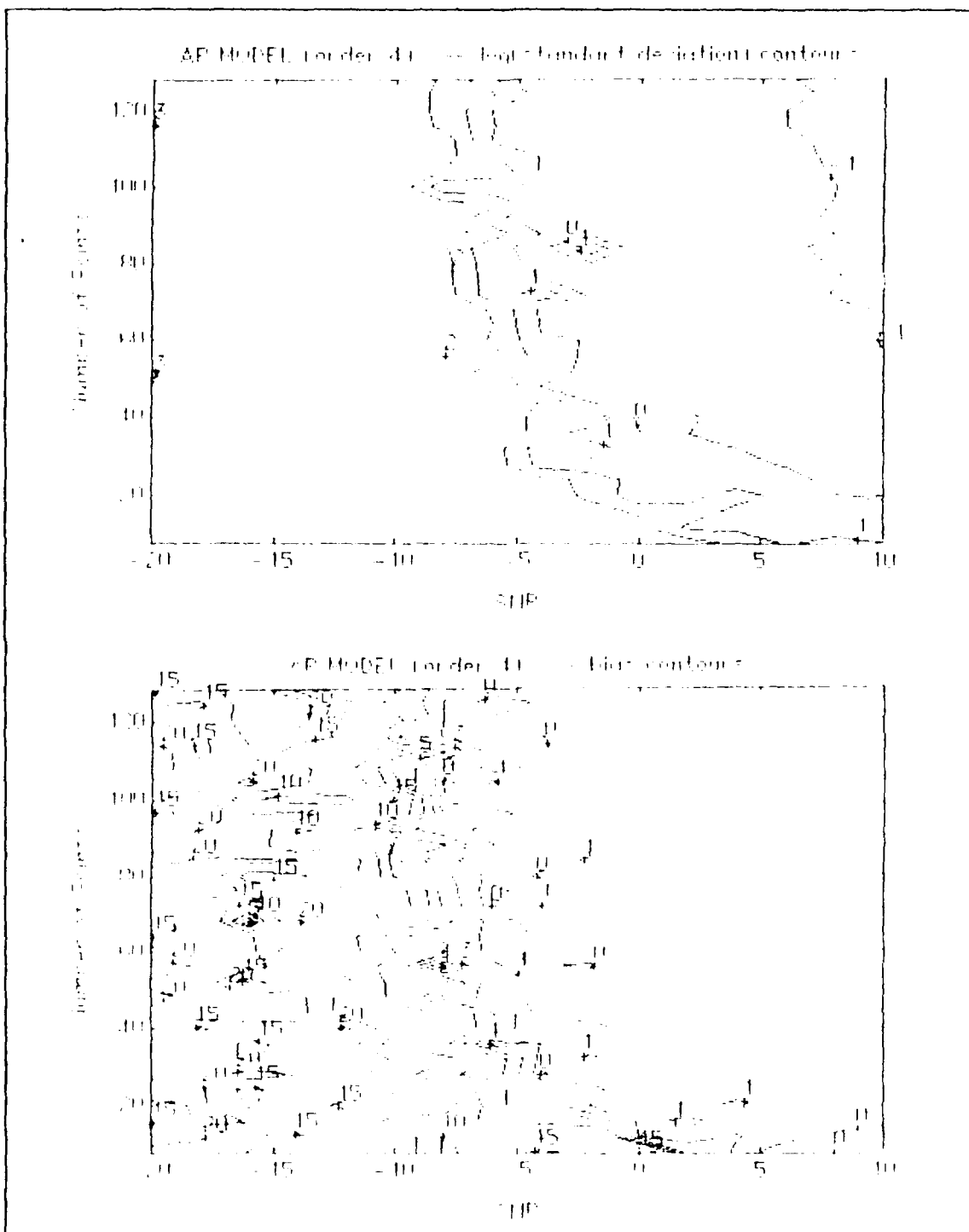


Figure 3.B.4 - Monte-Carlo Simulation: AR Model order 4 algorithm, Bias and Variance plots

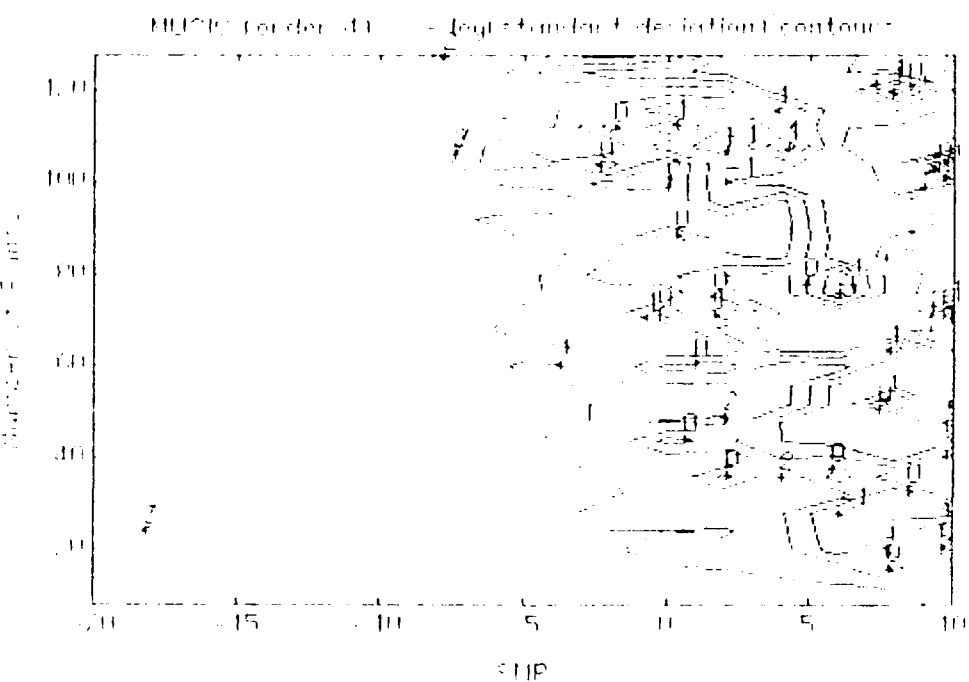
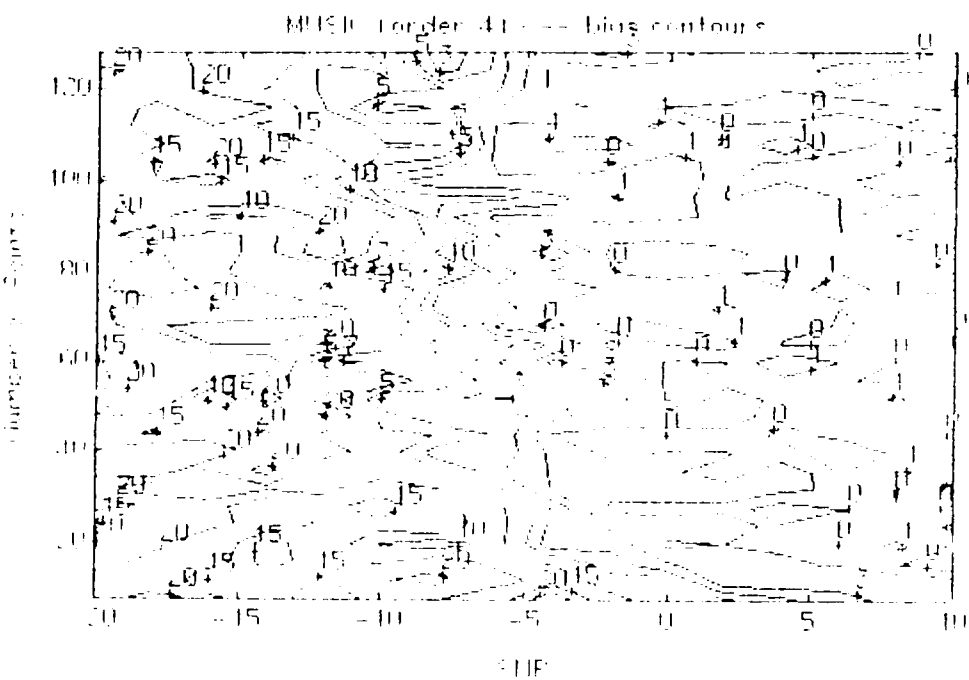


Figure 3.B.5 - Monte-Carlo Simulation: MUSIC order 4 algorithm, Bias and Variance plots

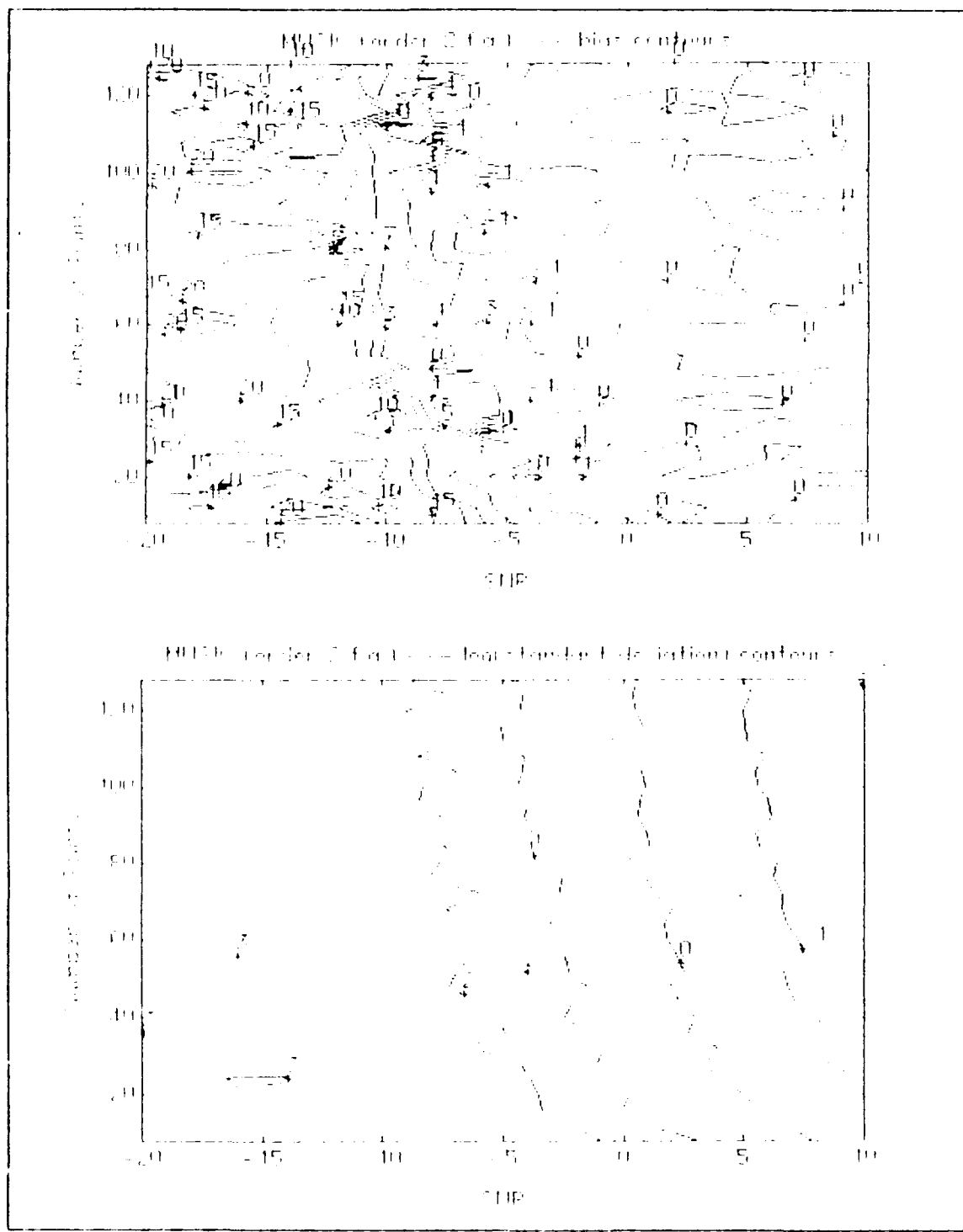


Figure 3.B.6 - Monte-Carlo Simulation: MUSIC order 2 algorithm, Bias and Variance plots

and ZERO CROSS for small sequences and the PEAK FFT for large sequences.

The lowest SNR for which we can get unbiased estimates with a good variance is -10 when using a PEAK FFT with 128 point sequences. Unfortunately this performance indicator does not show the discretization error, which becomes overwhelmingly significant for small FFT lengths. We can try to reduce this error by using interpolation schemes, however this procedure will make this algorithm slower for a small number of points and is very susceptible to low SNR. For SNR between -5 and 0 we should use sequences of at least 32 to 64 data points (PEAK FFT also), but these estimates will have severe discretization errors. For SNR between 0 and 5 we can use either the PEAK FFT or the PULSE PAIR/MUSIC 2 with 128 to 32 sequence length. For SNR greater than 5 the best performance is given by the MUSIC (order 2 fast algorithm) or PULSE PAIR. If we want to emphasize the speed of the estimators, the best results are the ones given by the PULSE PAIR/MUSIC 2, requiring high SNR.

Because the CDV package bistatic doppler frequency estimation is based on 32 points records, and the algorithms run in real time using C compiled code in a DSP, the most suitable algorithms selected from these simulations are the PEAK FFT for poor SNR, and the PULSE PAIR/MUSIC 2 algorithms for higher SNR. When considering discretization noise, the first choice for a spectral estimator to be used in the CDV

real time processing will be the PULSE PAIR estimator, because of its performance, simplicity and velocity.

IV. THE CDV MICROSTRUCTURE PACKAGE

A. RECENT METHODS FOR TURBULENCE OBSERVATIONS

1. Rapid Sampling Vertical Profiler (RSVP)

The RSVP was developed by Caldwell, Dillon and Moum in 1987 [Ref.19] for sampling near microstructure parameters from a moving vessel permitting the study of the horizontal variability of upper layer profiles. The instrument makes near-microscale measurements (3 cm resolution) of temperature, salinity and turbulence dissipation down to 100 m when deployed from a ship moving up to 6 Knots.

The profiler consists of a small retrievable probe at the end of a cable that is also a data link. Damping flaps are used to ensure uniform vertical velocity and orientation. The airfoil shear probe, used to estimate the TKE dissipation rate, is very sensitive to vibrational noise of the profiler, which may dominate the signal in many situations. The process by which it senses shear is based on the deflection of a piezo ceramic beam in a rubber jacket by cross-stream velocity. By careful instrument design, virtually all current measurements of ocean turbulent velocity have been made with this type of sensor.

Moum et.al. [Ref.10] performed upper ocean observations with this instrument where they were able to

characterize the fine structure of transition zone coastal eddys, and Dewey et.al. 1990 [Ref.7] used this type of measurements to study the enhancement of ocean fronts by turbulent mixing. The interesting results obtained in both experiments show the importance and applicability of the RSVP in upper ocean observations.

2. Pulse to Pulse Coherent Sonar

A pulse to pulse coherent sonar was developed by Lohrmann et.al. 1990 [Ref.20], called the High Resolution Current Profiler. This instrument uses four 307 KHz transceivers, mounted 30° off the vertical in 90° azimuthal intervals. Fifty range cells, covering a profiling distance of 10 meters, measure radial current components along the transceiver beams. These measurements do not give the true velocity vector, but assuming a stationary and homogeneous turbulent field, allows an estimation of the Reynolds stresses and turbulent kinetic energy by separating the mean and fluctuating parts of the radial speeds. In this way, this instrument remotely senses the turbulent stresses without inducing any flow distortions and provides moderate vertical resolution.

3. Bistatic Acoustic Doppler Profiler

This instrument, developed by T.P. Stanton (1990), measures the explicit velocity vectors at a very high temporal and spatial sampling rate along one direction. The system

consists of four, 300 KHz fan-beam receiver transducers, radially separated from a central narrow beam-width transmitter transducer, which rapidly emit short duration acoustic pulses. Range gated doppler shifts are evaluated at each receiver using dual interpulse period, coherent doppler estimation methods.

Simultaneous receptions at the four transducers provide an overdetermined estimate of the three velocity components at range bins along the ensonified volume, typically every 10 cm for 10 m ranges. This system allows concurrent measurement of reynolds stress components and fine-scale shear out to ranges of 30 m.

Velocity ambiguities from the coherent velocity estimation limit the unambiguous velocity range and profiling range. Unfortunately, the large frame for mounting the acoustic components restricts applications of the system.

B. SPECIFICATIONS OF THE CDV SYSTEM

The CDV Microstructure Package is a system developed by T.P. Stanton (1991) to measure ocean turbulence variables at a sub-centimeter resolution. It has 3 convergent acoustic transceiver beams operating at 5.296 MHz in a backscatter coherent mode, using both bistatic (0.6 cm focal cube) and monostatic operating modes. In the bistatic mode, one transducer is transmitting, while the other two are receiving the scattered energy from a focal volume. In the monostatic

mode the same transducer that transmits the signal receives the backscattered energy at range bins along the acoustic beam.

The acoustic measurements provide the velocity vector, shear and kinetic energy estimation at a 44 Hz rate, while simultaneous microstructure measurements of temperature, conductivity, pressure, shear and the 3 components of the instrument acceleration are made.

This package operates in a profiling mode at approximately 25 cm/s descending or ascending rate, or fixed to a tripod facing down for bottom layer observations, or facing up for shallow water, near surface, observations. The package has also been attached to an ROV for semi-lagrangian upper ocean turbulence measurements.

The digital data is transmitted to the surface by a 1.4 Mbaud fiber optic data stream that is stored on a PCM/VCR system. The data stream is also passed to an AT&T digital signal processor (DSP) in a 386 based HP VECTRA for real time processing and graphical monitoring of selected channels. This pre-processed data is then stored on optical disks for further processing. A summary of the profiler package technical specifications follows:

TABLE 3 - CDV CHARACTERISTICS

LENGTH	DIAMETER	WEIGHT
1.2 m	12 cm	7 Kg (in air)

TABLE 4 - ACOUSTIC CHANNELS

FREQUENCY	POWER	SAMPLING FREQUENCY	OUTPUT FREQUENCY
5.296 MHz	5 Watt peak, in a 2° beamwidth	11.1 KHz (after demodulation)	44 Hz

TABLE 5 - ANALOG CHANNELS

SAMPLING FREQUENCY	TEMPERATURE PRE- EMPHASIS	CONDUCTIVITY PRE-EMPHASIS	OUTPUT FREQUENCY
1.4 KHZ 5.6 KHz (shear)	0.339 Hz	0.100 Hz	44 Hz

C. SIGNAL PROCESSING OVERVIEW

The acoustic modes are controlled by a programmable sequencer that rotates the transmitting and receiving modes of the three transceivers, such that 3 monostatic and 3 bistatic modes have been selected every 20 ms. This acoustic data is received, complex demodulated to baseband and the complex (in

phase and quadrature) channels sampled at 11.1 KHz, for the bistatic data and 88.2 KHz for each monostatic channel.

The temperature and conductivity variables are pre-emphasized, in order to obtain an improved SNR at small scale and directly estimate gradient quantities, and sampled at 1.4 KHz. The 3 acceleration channels and pressure are sampled at the same rate, while the shear pre-emphasized data is sampled at 5.6 KHz.

The data stream comprises a set of 8 word records, such that the first two are used by the non-acoustic channels and the other 3 pairs correspond to the complex demodulated acoustic data. These 8 word records are contained in a sequence frame of 2051 words (corresponding to 22.7 ms of data) which are passed by DMA to the DSP for processing and to a PCM/VCR system for storage.

Once the DSP acquires the data, the data stream is interpreted and the real time processing is performed.

Further processing, such as:

- 1 - Water salinity computation
- 2 - Water density computation
- 3 - Velocity vector (u, v, w components) estimation
- 4 - Spectral analysis of several variables
- 5 - Reynolds stresses estimation
- 6 - Scalar fluxes estimation
- 7 - Dissipation estimation
- 8 - T.K.E. estimation

is performed by external programs accessing this preprocessed data on the optical disks. The overall flow graph is shown in the figure 4.C.1.

D. ACOUSTIC CHANNELS - VELOCITY ESTIMATIONS

The velocity component estimation in the acoustic bistatic mode is based on the mean doppler shift of the backscattered acoustic energy resulting from the relative velocity of scatterers present in the focal volume. The real-time pre-processed acoustic data stored on the optical drive comprise the mean doppler shifts for the 6 different acoustic paths between pairs of transmitters and receivers. In the bistatic mode, the single transmitter/two receiver configuration is sequenced around the three transducers. In order to obtain the velocity components from this spooled data, the following steps are performed:

- 1 - Clear data of large spikes using a reciprocal channel comparison and a 4th order linear predictor, based on the previous 20 point autocorrelation function estimate.
- 2 - Compute velocities from the doppler frequencies.
- 3 - Transform estimates to an orthogonal frame of reference fixed to the instrument.
- 4 - Rotate estimate to an absolute vertical reference frame.

1. Doppler Velocities Estimation

For two generic transducers, where transducer 1 is transmitting and transducer 2 is receiving, see figure

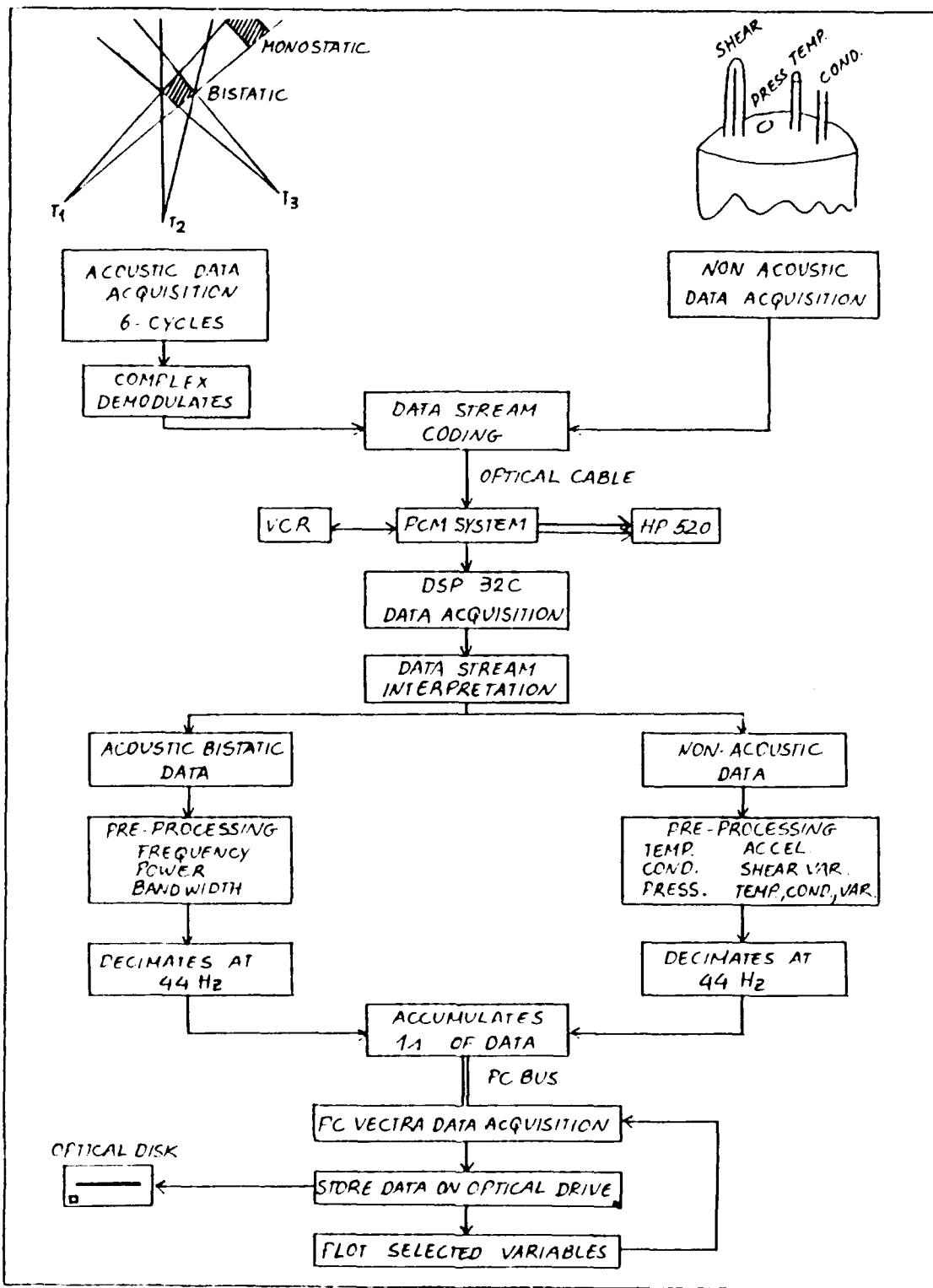


Figure 4.C.1 - CDV Signal Processing overview.

4.D.1.1, and assuming that the equipment is fixed to the bottom, we can derive the following doppler relationships [Ref.21]. If a pulse is transmitted at time $t=0$, it will arrive at BS at time $t=t_1$, that for a sound velocity "c" will be given by:

$$c \cdot t_1 = l + v_{BS}^{T1} \cdot t_1 \rightarrow t_1 = \frac{l}{c - v_{BS}^{T1}}$$

Now, if a second pulse is transmitted at time t_2 , it will arrive at BS at time t_3 , and

$$t_3 = \frac{l + c \cdot t_2}{c - v_{BS}^{T1}} \rightarrow t_3 - t_1 = \frac{c}{c - v_{BS}^{T1}} \cdot t_2$$

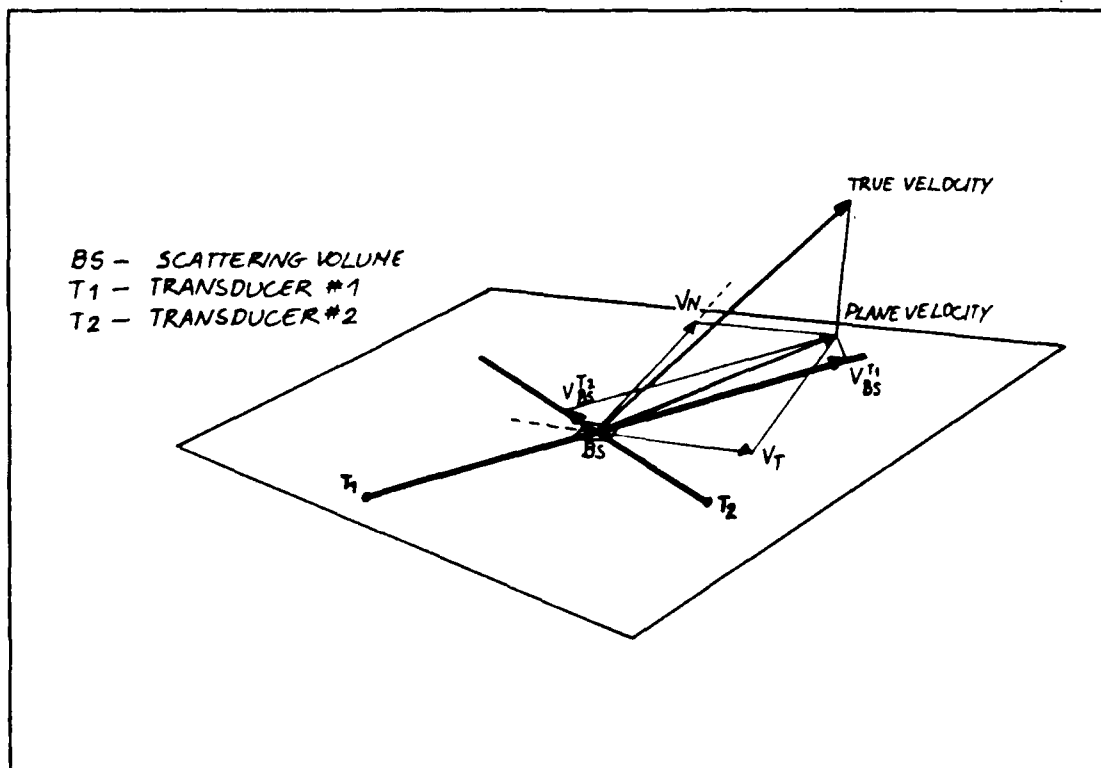


Figure 4.D.1.1 - Scheme of a Bistatic 2 transducer system.

Assuming that during the interval $(0, t_2)$ we are transmitting at a frequency f_{tx} , there will be $f_{tx} \cdot t_2$ wave fronts arriving at BS, during the interval $t_3 - t_1$. Therefore, the frequency detected at BS will be:

$$f_{BS} \cdot (t_3 - t_1) = f_{tx} \cdot t_2 \Rightarrow f_{BS} = \frac{C - v_{BS}^{T_1}}{C} \cdot f_{tx}$$

This frequency corresponds to the frequency of the scattered signal at BS that will be send towards T2. Using the same procedure we arrive at the following expression for the frequency at T2:

$$f_{T2} = \frac{C}{C + v_{BS}^{T_2}} \cdot f_{BS} = \frac{C - v_{BS}^{T_1}}{C + v_{BS}^{T_2}} \cdot f_{tx}$$

If we suppose that the velocity at BS has one component v_N , see figure 4.D.1.2, then $v_{BS}^{T_1} = -v_{BS}^{T_2}$ and $f_{T2} = f_{tx}$. Therefore the only velocity component producing a doppler shift will be along the direction defined by the axis bisection of the two beams i.e. v_r . This component will have equal projections along the two beams, so that:

$$v_{BS}^{T_1} = v_{BS}^{T_2} = V^{12} = V_N \sin \theta$$

Therefore

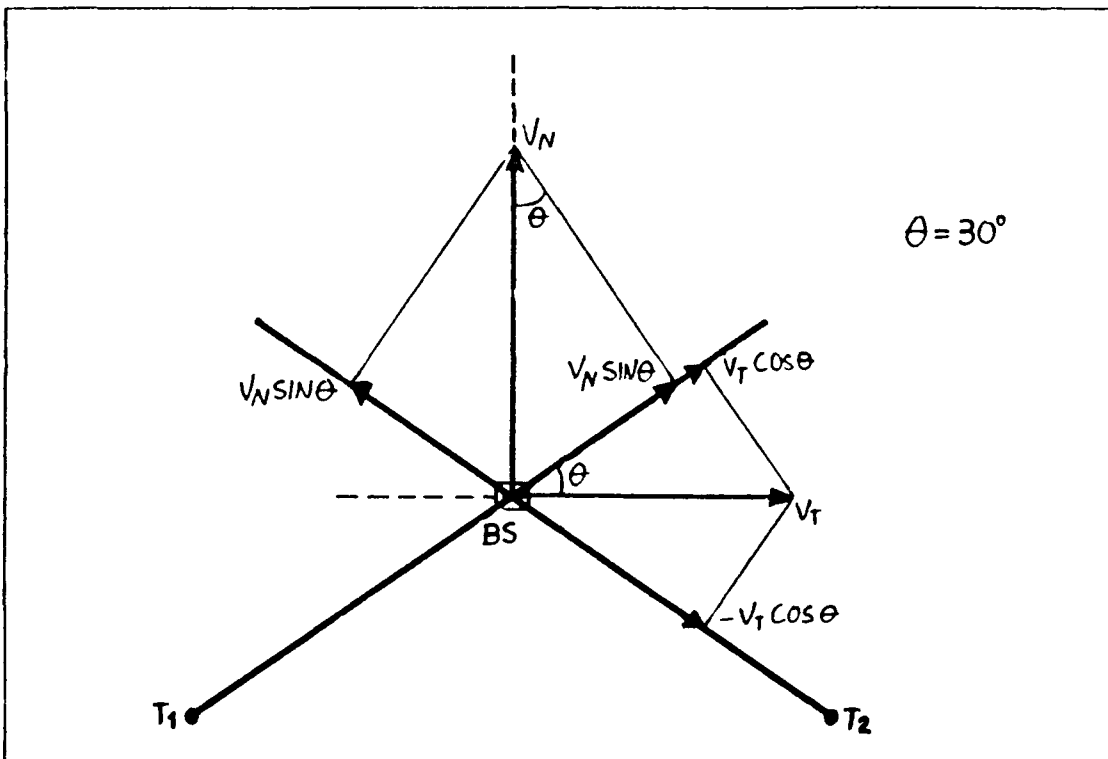


Figure 4.D.1.2 - Velocity projections scheme for a 2 transducers bistatic system.

$$V_{\kappa}^{12} = C \cdot \frac{f_{tx} - f_{rz}}{f_{tx} + f_{rz}} = C \cdot \frac{\Delta f^{12}}{2f_{tx} - \Delta f^{12}} \approx \frac{1}{2} \cdot C \cdot \frac{\Delta f_{12}}{f_{tx}}$$

and

$$V_{\kappa}^{21} = \frac{1}{2 \sin \theta} \cdot C \cdot \frac{\Delta f^{12}}{f_{tx}}$$

Because of the symmetric geometry of this system, this expression will also be true for the case when T2 is transmitting and T1 receiving. This fact creates redundancy in

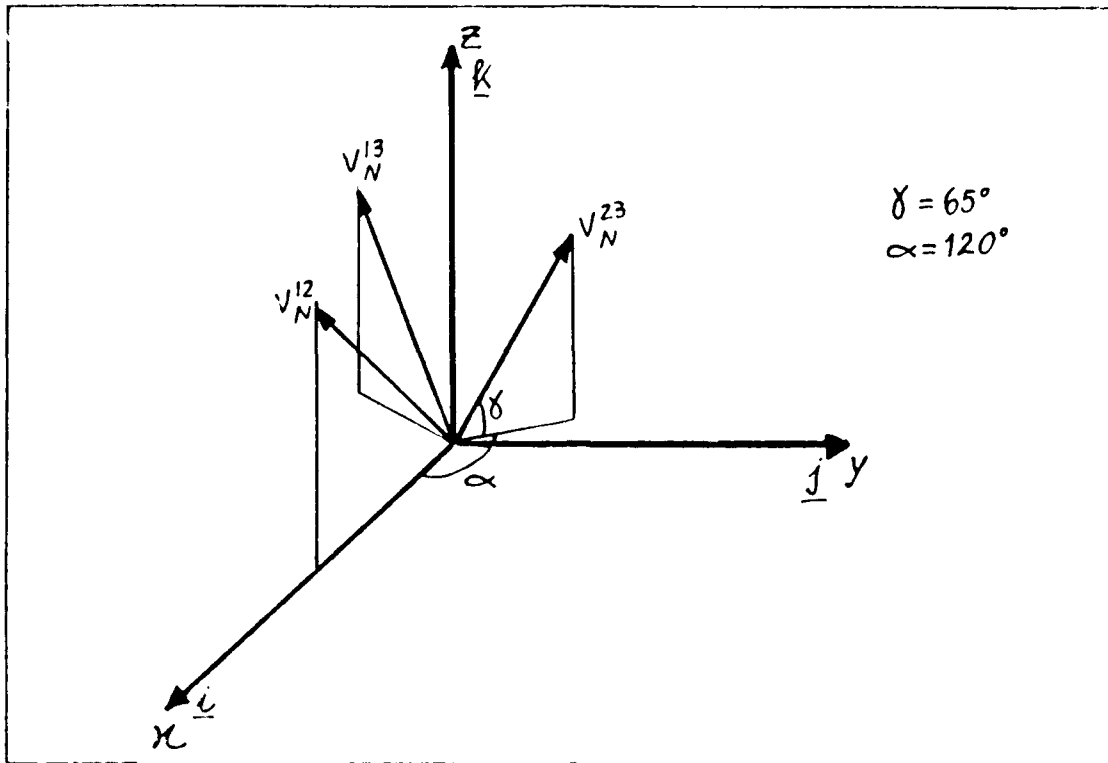


Figure 4.D.2.1 - CDV Package, Orthogonal Reference Frame fixed to the instrument.

the observed doppler frequency, which provides increased confidence of the estimates by averaging, and allows the detection of single spurious wild points. Therefore the six acoustic transceiver modes, will measure three slanted velocity projections along the axes bisecting the acoustic beams.

If the instrument was in motion we would have to add the instrument velocity components along these axis, in order to get absolute values. These operations are implemented by programs external to the real time processing.

2. Velocities on an Orthogonal Reference Frame

The Doppler velocity components must be transformed into an orthogonal frame before the Reynolds stresses or the scalar fluxes can be estimated. We can define the instrumental orthogonal reference frame as in figure 4.D.2.1.

The scatterers velocity will be defined as:

$$\underline{V}_I = u_I \underline{i} + v_I \underline{j} + w_I \underline{k}$$

and the observed velocities will be:

$$\begin{bmatrix} V_N^{1z} \\ V_N^{2z} \\ V_N^{3z} \end{bmatrix} = \begin{bmatrix} \cos\gamma & 0 & \sin\gamma \\ \cos\gamma\cos\alpha & \cos\gamma\cos(\alpha - \frac{\pi}{2}) & \sin\gamma \\ \cos\gamma\cos\alpha & -\cos\gamma\cos(\alpha - \frac{\pi}{2}) & \sin\gamma \end{bmatrix} \times \begin{bmatrix} u_I \\ v_I \\ w_I \end{bmatrix}$$

i.e.

$$\underline{V}_N = T \times \underline{V}_I$$

Therefore, this system may be solved in terms of the unknowns u , v and w by inverting the non-singular matrix "T".

The next step is to rotate this velocity in the x-axis and y-axis in order to obtain a vertical z-axis. This can be

accomplished in several ways depending on each particular deployment. For the case when we have the system fixed to a tripod, we can look for the rotations that minimize the mean vertical velocity, or just measure the platform orientation using the 3 axis accelerometer as tiltmeters.

E. NON-ACOUSTIC DATA

The non-acoustic channels on the CDV package are: 3 component acceleration, pressure, temperature, conductivity and shear. The real time processing for these channels was coded in C language and compiled on the DSP together with the Assembler routines that access the CDV data stream in memory. This DSP program is controlled by another C routine running on the Host computer, that interacts with the user, reads the proper setup files, receives the data from the DSP, plots selected variables of the pre-processed data and sends the output to an optical mass storage unit. The details on the processing of each particular channel are described next.

TEMPERATURE AND CONDUCTIVITY

The temperature variable (T) is measured using a high frequency response FP 07 thermistor, and conductivity (C) using a 2 electrode AC conductivity probe. The analog temperature and conductivity are pre-emphasized at 20 dB per decade for frequencies greater than 0.339 Hz and 0.100 Hz respectively, for SNR optimization. They are sampled at 1.4

KHz and the multiplexed data stream is sent to the DSP by DMA assembly input routine.

A DSP function demultiplexes variables from the data frame to separate selected variables from the stream. A first difference criteria with a threshold set by a setup file, is used to detect spikes on the data. Single bad points are substituted by the previous valid point. Deterministic coherent noise over each frame period (32 words) is subtracted from each data cycle. This coherent noise is computed from the mean of approximately 5000 frames and is entered from an input file. The raw T and C gradient data are then squared and accumulated on 1 second rotary buffers for estimation of gradient variances. Both the T and C data are also de-emphasized by single pole digital Butterworth filters and low pass (LP) filtered by a second order Butterworth filter with a cutoff frequency at 20 Hz. These operations are done in sequence by different functions to avoid round off errors. Finally the de-emphasized data is decimated to 44 Hz and the variances are computed based on the mean of the 1 second rotary buffers. These 44 Hz data are sent every second to a HOST program running on the HP Vectra.

ACCELERATION AND PRESSURE

Acceleration is observed using 3 orthogonal solid state DC response accelerometers in the head of the CDV. Pressure is sensed using a strain gauge pressure sensor. Both Acceleration and Pressure are processed in a similar manner.

The DSP function that demultiplexes the input buffer, also separates these 4 channels from the data stream. The same deglitching procedure is used concurrently with a threshold of 200 raw counts for the four channels. There is negligible observed coherent noise on these channels. The data is then LP filtered by a third order Butterworth with a cutoff frequency at 20 Hz, decimated to 44 Hz and sent to the HOST program every 1 second for monitoring and storage.

SHEAR

To measure the velocity shear, cross-velocity variations are measured with a high sensitivity airfoil probe. Because of its nature, this sensor is easily noise contaminated by variations in the instrument velocity or spurious vibrations. Also, it only works when the instrument is in motion and senses only velocity changes perpendicular to the mean sensor velocity.

The shear probe is sampled at 5.6 KHz and the data send to DSP by DMA assembly input routine. The same DSP function separates the shear from the data stream and applies a 200 count, first difference deglitching criteria. Any deterministic coherent noise is subtracted from each data cycle. Next, the pre-emphasized (gradient) data is squared and accumulated in 1 second rotary buffers, and the variance is computed at a 44 Hz rate and sent to the HOST program.

F. CALIBRATION AND ERROR ANALYSIS

The temperature data was previously calibrated using a third order polynomial fit of the form:

$$TEMP = A \cdot COUNTS^3 + B \cdot COUNTS^2 + C \cdot COUNTS + D$$

where

$$A = 10.662337$$
$$B = -3.957935 \cdot 10^{-4}$$
$$C = 1.216833 \cdot 10^{-9}$$
$$D = -1.345511 \cdot 10^{-14}$$

where TEMP represents temperature values in Degrees Celsius and COUNTS the CDV outputted values.

The pressure sensor was calibrated by recording the pressure values obtained from water columns from 0.10 meter to 2.00 meter, 0.10 meter apart. The calibration transformation was then computed using a least squares fit to a straight line by solving a system of 20 equations on 2 unknowns. The resulting calibration is:

$$DEPTH = 0.000191964 \cdot COUNTS - 0.0218414$$

where DEPTH is the water column height in meters and COUNTS the pressure channel output values. The mean square error is 0.0012 m. The calibration was performed with pure water, so that in order to compute the depth in salty water, this values must be multiplied by a factor related to the density anomaly,

that for practical use can be 0.974 (assuming a density of 1026 Kg/m³).

The acceleration channels were calibrated using the fact that when the equipment is fixed the mean observed value should be the gravitational acceleration. The package was fixed and rotated from -20° to +20°, in 5° intervals on two quasi-orthogonal planes, with one of the planes containing one of the horizontal accelerometers. Least square fits to straight lines were performed, resulting in the following calibration:

$$\begin{aligned} ACC_x &= 0.00108549 . COUNTS_x - 18.0324 \\ ACC_y &= 0.00119582 . COUNTS_y - 19.9673 \\ ACC_z &= -0.00110622 . COUNTS_z + 16.9346 \end{aligned}$$

where ACC_i is the acceleration in m/s² and COUNTS_i the outputed quantities. The observed mean square errors are 0.0532 m/s², 0.0210 m/s² and 0.0634 m/s² in the X, Y and Z channels respectively.

To evaluate the performance of the equipment, two 5 minutes data sets were selected from the WHARF #2 Experiment at the August 2 1991. This experiment will be described in more detail in the next chapter. The calibrated temperature values are very closed to those observed using a mercury thermometer bucket temperature. The accelerometer mean values are reasonably close to the expected. Because there was no in

situ calibration, only mean quantities can be analyzed. A more detailed description of these data will be presented in the next chapter. This experiment was performed with the instrument fixed to the bottom, so no shear probe data was analyzed. No pressure data was available from this deployment.

The first step in the analysis is to look at the pre-processed doppler data. A sample of two bistatic reciprocal channels (frequency, power and bandwidth), and calibrated temperature data is shown in the figures 4.F.1-2.

A careful analysis was required for the velocity estimation, because there was no previous experience with this method. It was necessary to validate all the processing steps (both electronic and software).

The reciprocal channel doppler frequency estimates are generally similar, see figure 4.F.1, except for individual spikes, or in regions of very low signal to noise ratio (SNR) which are also seen by a large bandwidth. Some of these discrepancies will be attenuated by using a variable pulse repetition interval in future deployments, eliminating coherent additive interference.

To increase the confidence and deglitch the acoustic data, an adaptative procedure has been developed. The probability distribution function (PDF) of the differences histogram (see in the Figure 4.F.3), shows that the differences between two consecutive values are smaller than 70 Hz (0.01 m/s) 75% of the time. Also, the scatter plots between the first

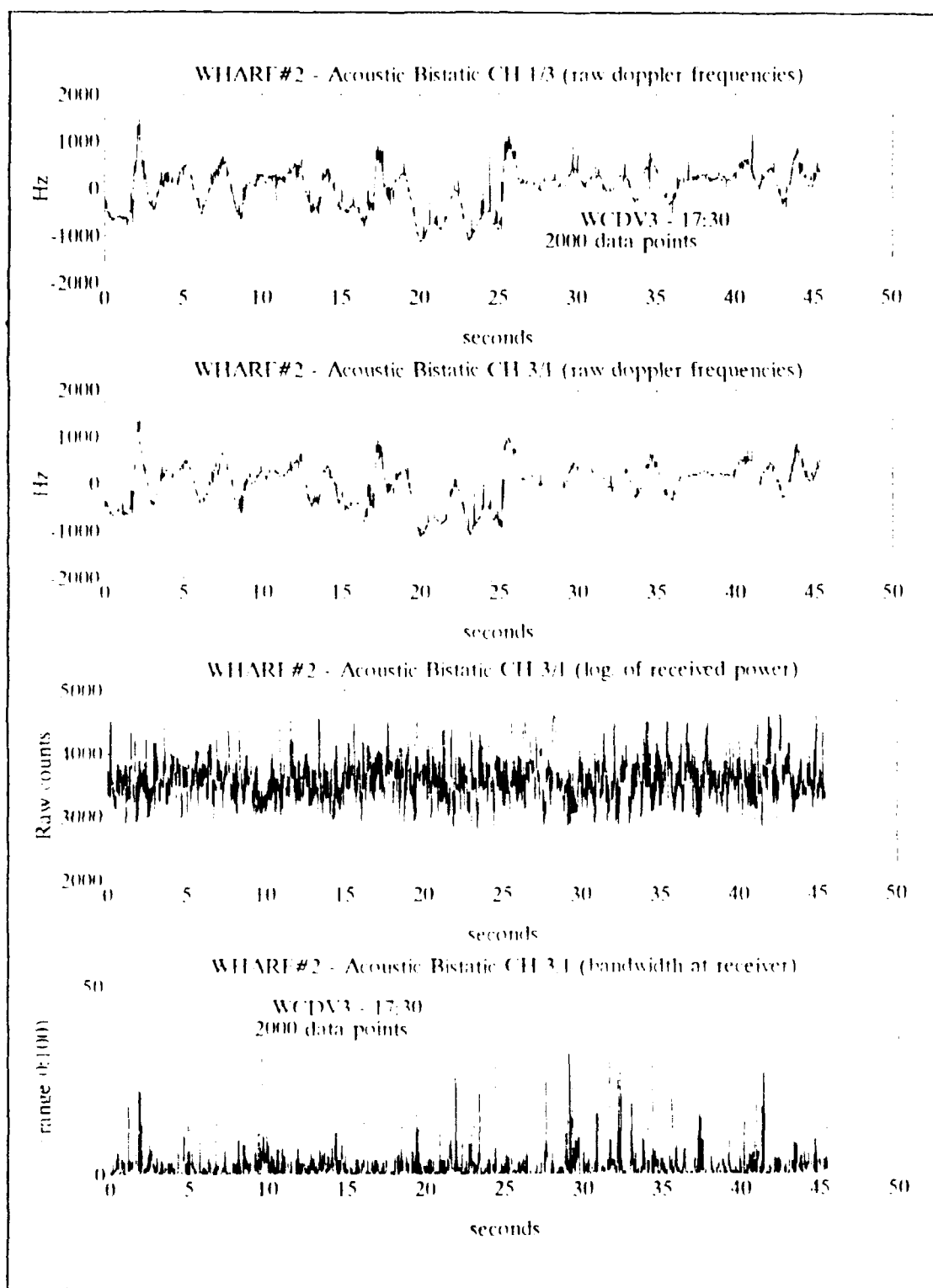


Figure 4.F.1 - Reciprocal Bistatic channels, doppler frequencies, received powers and bandwidth.

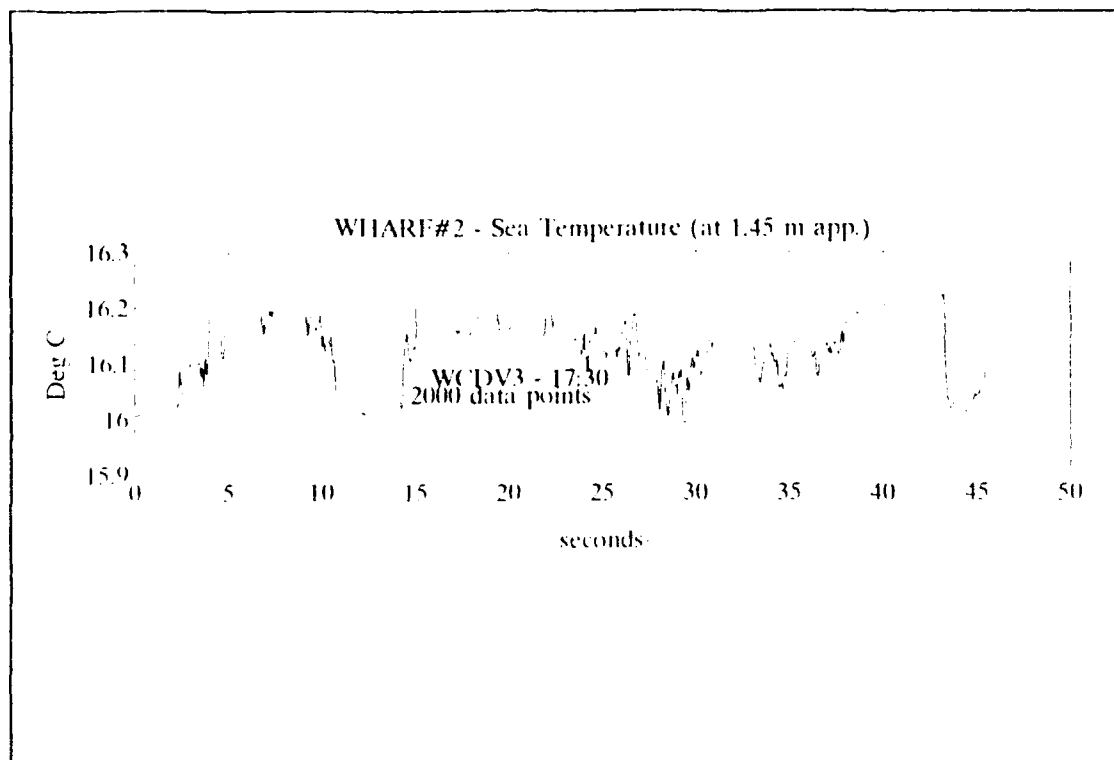


Figure 4.F.2 - Calibrated Temperature data. Simultaneous to the data shown in figure 4.F.1 .

differences and the received powers (Figure 4.F.4) shows that the bigger differences are mainly associated with low received powers, corresponding to the cases when noise from additive interference and system noise may be significant. We have two independent realizations of the same random variable (reciprocal channels) that can be used either to increase the confidence of the estimates or to validate them.

To deglitch the data and obtain a clean averaged time series of the doppler frequencies, an intelligent adaptative algorithm must be used based on the surrounding points. A procedure was implemented to compare the signal at each time with a predicted value obtained from a 4th order linear

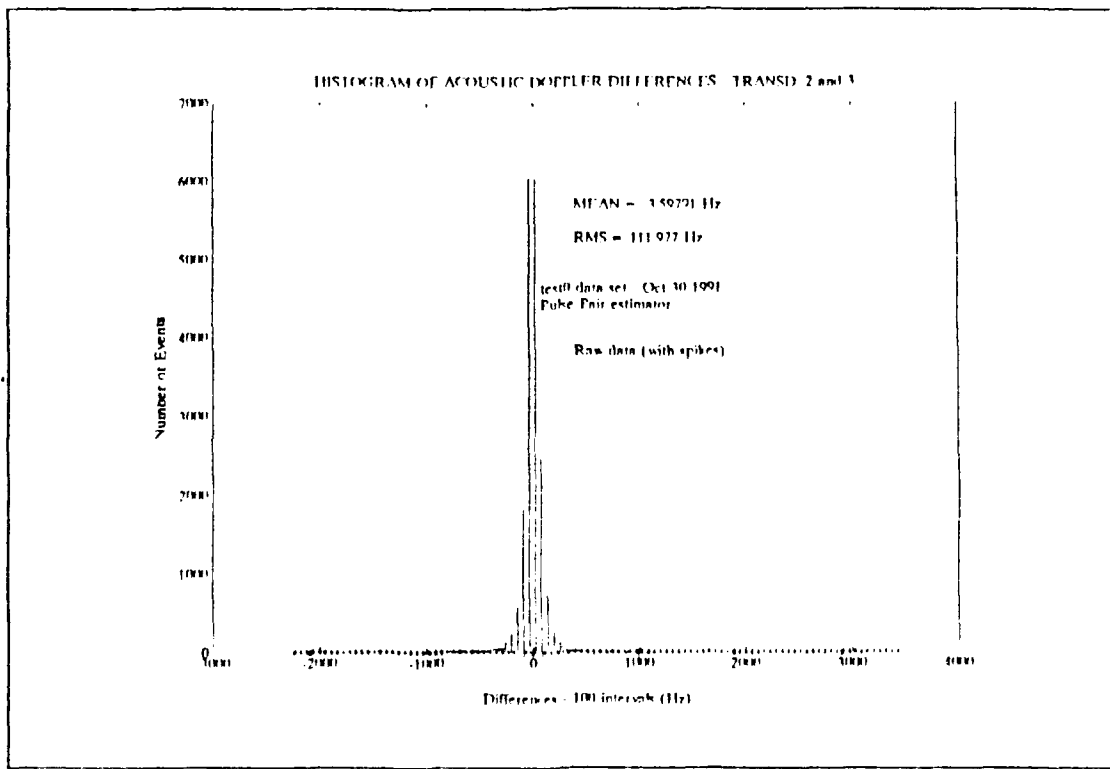


Figure 4.F.3 - Reciprocal Bistatic channels, first differences histogram.

predictor based on the previous 20 point autocorrelation function. Whenever the difference was greater than four times the standard deviation (also estimated from the previous 20 points), that point was assumed non-valid. When both channels were assumed bad, or if a first difference fixed criteria was violated, the predicted value was used. We can expect an improvement in the SNR of the estimates by using this method. Some examples of how this procedure works, are shown in the figure 4.F.5.

To transform these deglitched doppler shifts to velocity components in an orthogonal frame fixed to the instrument, a linear transformation must be performed. This transformation

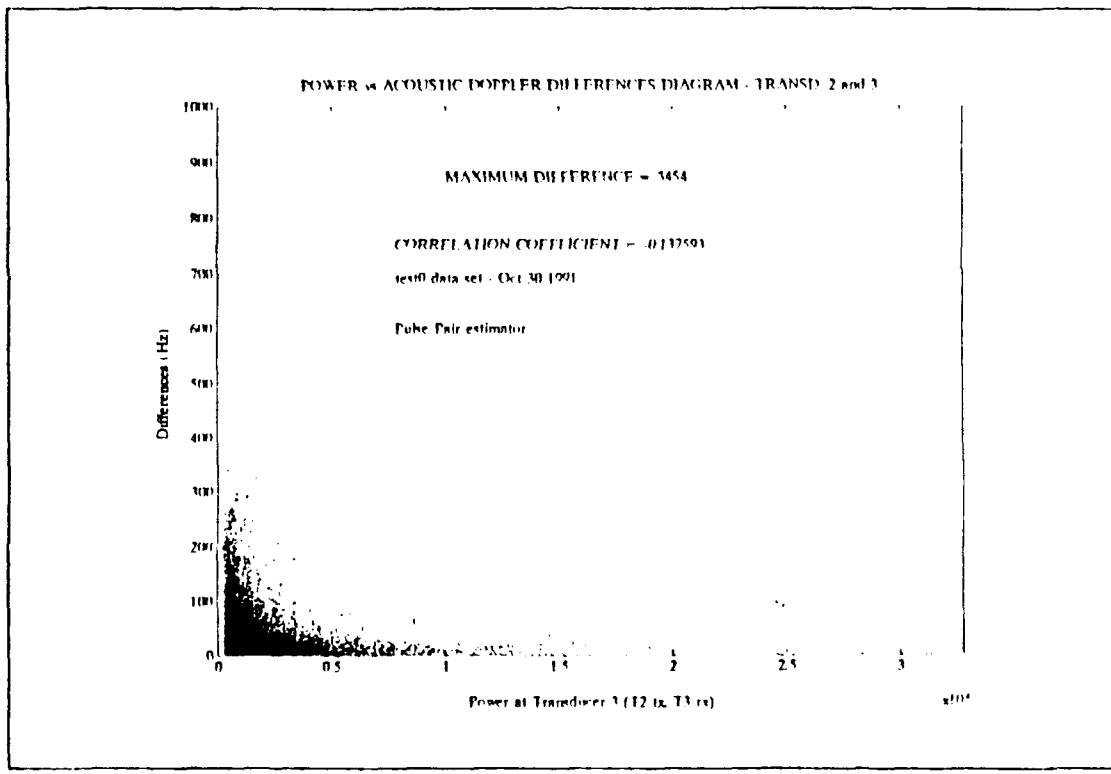


Figure 4.F.4 - Reciprocal Bistatic channels, Scatter plots between first differences and received power.

will not distribute the velocity variance evenly through the 3 orthogonal components of velocity, giving more weight to the component along the instrument vertical; this component will also have a greater statistical confidence.

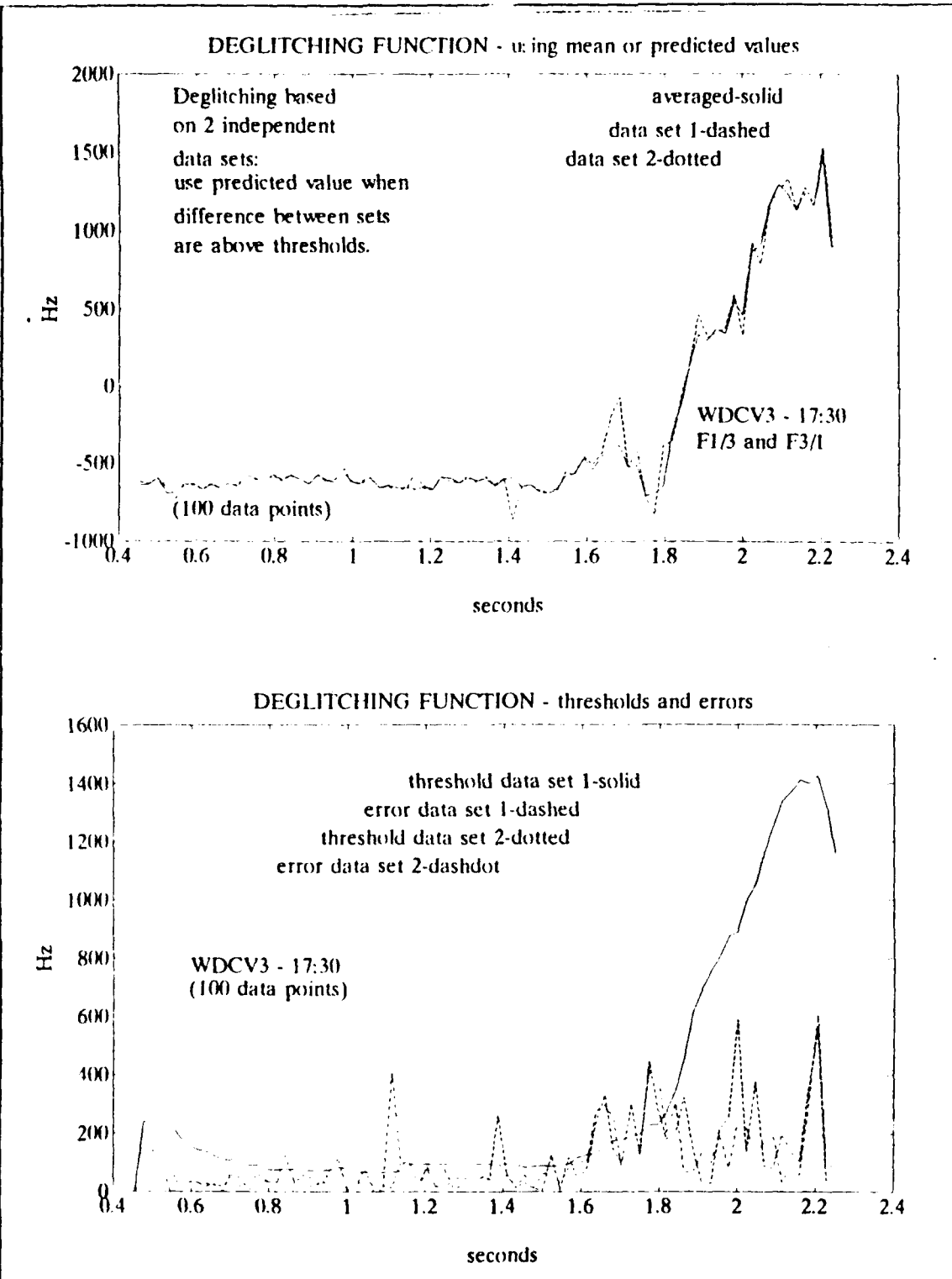


Figure 4.F.5 - Bistatic channels deglitching function.
Whenever the difference curves go higher than the threshold curves, in the lower plot, that point was assumed as bad data.

V. TURBULENCE OBSERVATIONS USING THE CDV PACKAGE

A. WHARF #2 EXPERIMENT

The purpose of this experiment was to asses the performance of the CDV package in oceanic backscatter conditions, test its ability to measure ocean fluxes and surface wave fields, and to study the forcing mechanisms in ocean surface layers.

The CDV package was deployed off the Monterey Wharf #2 on 2 and 3 August 1991. The tripod-mounted CDV was placed on the sand-bed with the top of the instrument at depths ranging from 0 to 0.75 meter. The depth changed with the tide, and the total water depths ranged between 1.7 to 2.5 meter.

The package was controlled and monitored from a van parked on the wharf, from which observations of air temperature (moist and dry), bucket sea surface temperature, short and long wave radiation and wind direction and speed. The equipment deployment is sketched on figure 5.A.1.

The air temperature was measured using a mercury psychrometer and the sea surface temperature using a protected mercury thermometer. The wind speed and direction was recorded using a MRI anemometer and wind vane, while the short and long wave radiation was obtained from an Epply radiometer.

MONTEREY WHARF #2 EXPERIMENT

AUG 2/3 1991

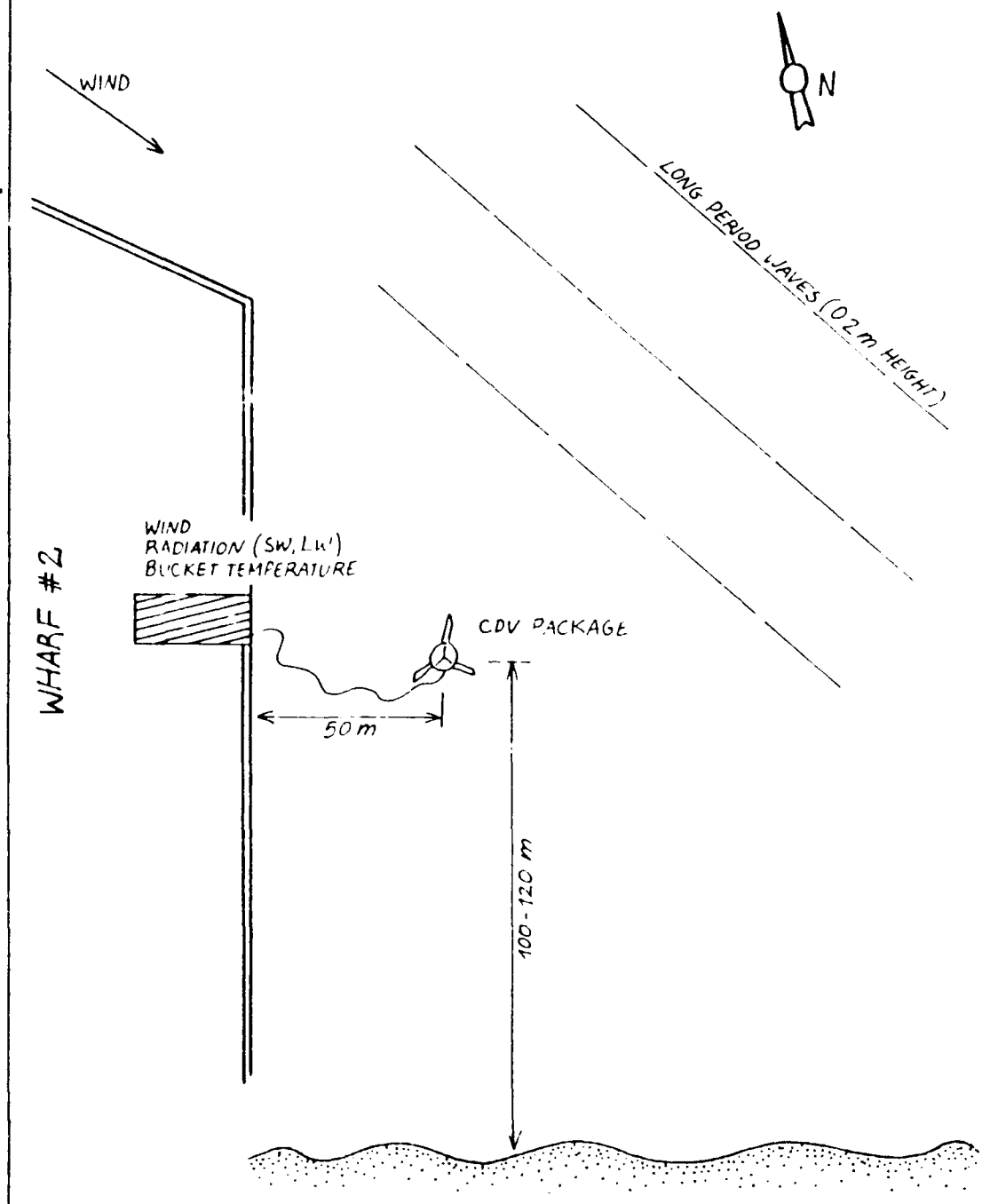


Figure 5.A.1 - Wharf #2 Experiment set-up

The environmental conditions were characterized by an overcast sky, moderate to weak winds from WNW. Small amplitude swell from the North was being reflected from the solid walls below the wharf. Due to the barrier created by the wharf walls on the wind field, the measured winds did not correspond well to those over the CDV package. These light wind conditions were not ideal to evaluate the overall performance of the instrument, because we would not expect to find high turbulence levels in the high frequency range. Nevertheless, because we understand the physics of the linear wave fields and we do not have lateral boundary effects (as we would encounter in a tank experiment), we were able to measure the performance of the package at the low and medium frequency range using the wave field signal, and to estimate the noise floor at higher frequencies.

The CDV data were recorded on VCR tapes (labeled WCDV1 to WCDV7), from 1100 until 2300 on 2 Aug 1991, covering the afternoon high tide at 1545 pm, and from 0200 to 0800 at 3 Aug, covering the morning high tide at 0515. The short and long wave radiation and the wind data were recorded continuously from 1100 am of 2 Aug until 0800 am of 3 Aug, sampled at 8 Hz and spooled by an HP 332 computer to an optical drive for further processing. The air and bucket temperature were recorded every hour from 1600 2 Aug to 0800 3 Aug.

After a careful analysis, only the afternoon CDV data from 1300 to 1800 show high data quality, while the morning data show large data gaps due to the fact that the equipment was only partially submerged.

Following DSP preprocessing, all the data were spooled to an HP VECTRA 386 and the CDV bistatic data to a SUN SPARC STATION for further processing.

After calibration, the 8 Hz sampled wind and radiation data were 10 min averaged and decimated at a 1/min sampling rate. The CDV sea temperature was calibrated and used for cross-spectral analysis and computation of fluxes over 20 minutes averages. The bistatic doppler frequency estimates were deglitched using the adaptative procedure described in the previous chapter, and used to estimate the velocity vector in an instrumental reference frame. The instrumental velocities were then properly rotated to a vertical reference frame. All the processed data (intermediate and final), spectral and flux estimates and output plots were stored on an optical disk.

B. METEOROLOGICAL DATA

This section describes and analyzes the tide, wind, radiation, air and sea surface temperature data. It will focus only on the period from 1100 to 2000 of 2 Aug 1991, simultaneous with the useable CDV data.

As is shown in the Figure 5.B.1, within this period there was a high tide at 1545 pm. The tide height determines the depth of the CDV measured quantities; so in Figure 5.B.1, the expected mean depth of the top of the CDV is shown, assuming that at 1100 it was at a 0 m depth. Also shown as vertical straight lines are the times of the evaluated ocean fluxes.

Due to problems in the radiation sensors, long wave radiation data was not available. This fact restricts our ability to compute the surface buoyancy fluxes; however, we can use the short wave radiation and wind stress as indicators

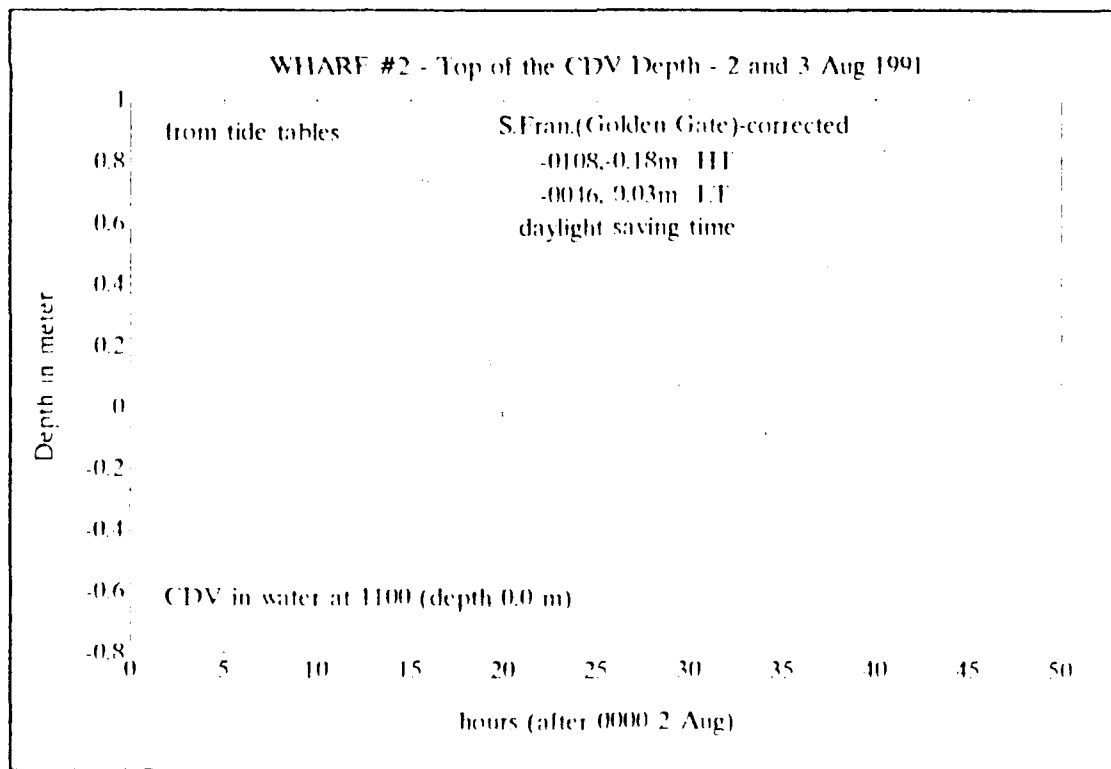


Figure 5.B.1 - Wharf #2 Experiment: depth of the top of the CDV package at 2 August 1991.

of the forcing mechanisms in the ocean upper layer. The wind data does not accurately reflect wind stress at the CDV location due to the barrier created by the wharf walls, but it will show the maximum expected mechanical forcing of the ocean surface. The time evolution of these variables is shown in Figure 5.B.2, for the period from 1200 to 2000 pm at 2 Aug 1991, based on measurements made from the top of the wharf.

These plots show that the wind stress was decreasing slightly after 1500. Due to the overcast conditions during almost all the period of the experiment, we should not expect a large variability on the long wave radiation, so the changes in the surface buoyancy flux should be determined primarily by the short wave radiation and by the surface layer stability. The short wave radiation followed a cloud covered diurnal cycle increasing until 1500, and decreased thereafter. The peak shown at approximately 1420 corresponds to a short period of time of partially clear sky. From these conditions, we may expect a decrease in the weak mechanical steering due to decreasing winds and a reduction in the stability of the upper layer and due to a reduction of solar heating. Therefore, we should not expect to find high levels of turbulent energy in the form of scalar fluxes and Reynolds stresses, i.e. we should not expect to observe an active mixing layer, so that the ocean conditions should be dominated by surface gravity wave fields.

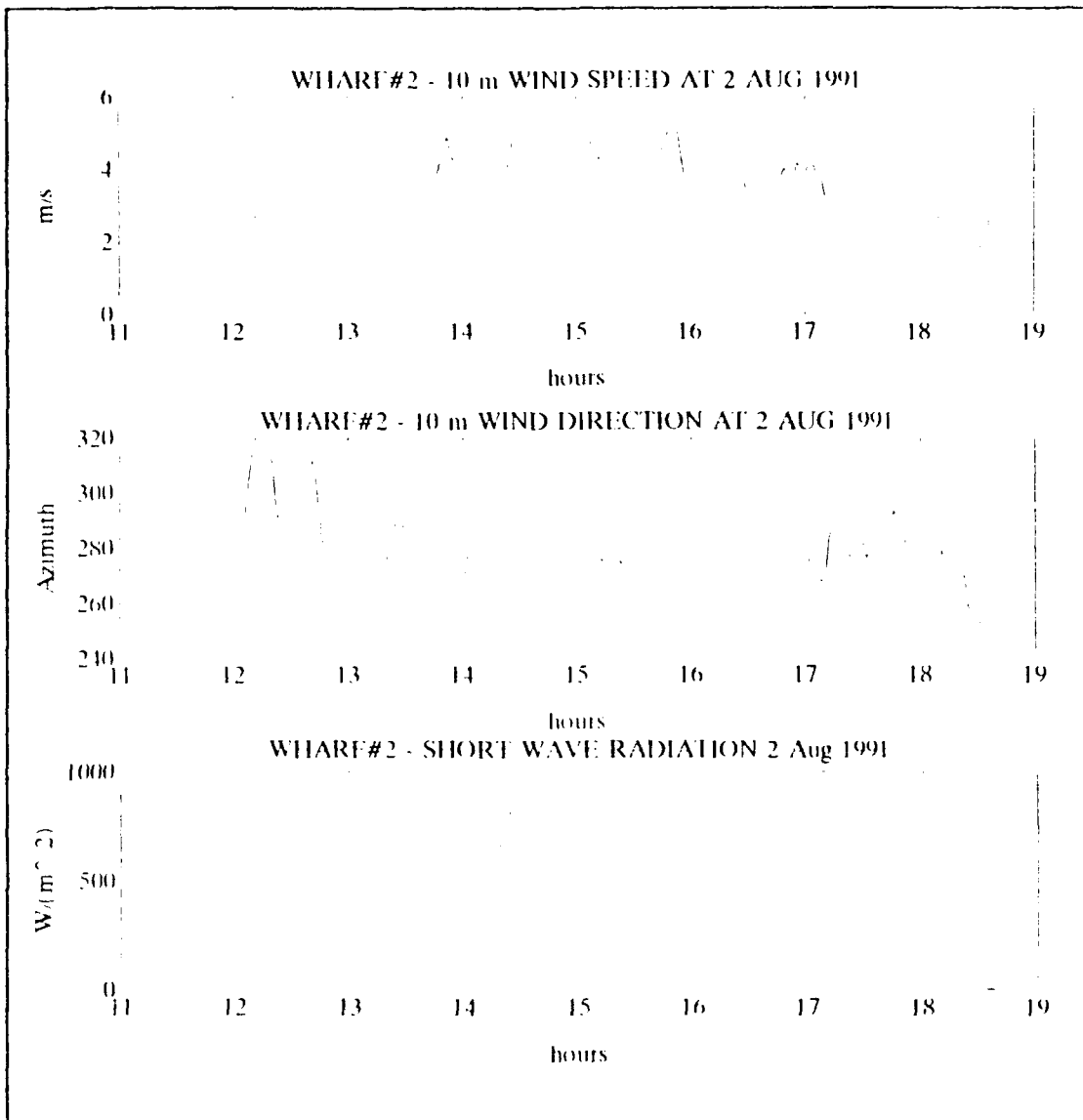


Figure 5.B.2 - Wharf #2 Experiment: Wind stress and short wave radiation, from 1200 to 2000 at 2 Aug 1991.

C. CDV DATA

The data between 1500 and 1800 of 2 Aug 1991 were analyzed in more detail and the ocean fluxes computed using an eddy flux correlation method [Ref.2]. The first step was to select 20 minutes ensembles every 1 hour. These data sets were then

spooled to an optical drive, and the data analyzed in more detail using C programs and MATLAB software.

After conversion to engineering units, the acceleration and temperature data were averaged over all the 20 minute ensembles; the tilt angles were computed and the mean temperatures compared with the observed bucket temperature.

TABLE 6 - CDV AVERAGED DATA

Hour (2 Aug)	15:30	16:30	17:30	18:30
Acceleration-X (m/s ²)	0.1626	0.1588	0.1630	0.1553
Acceleration-y (m/s ²)	-0.6645	-0.6647	-0.6718	-0.6787
Acceleration-z (m/s ²)	-9.8278	-9.8330	-9.8277	-9.8288
Direction-Deg (ref.to x-axis)	-76.25°	-76.56°	-76.36°	-77.10°
Tilt (Deg) (from vertical)	3.98°	3.976°	4.02°	4.05°
Mean Temperature (bucket)	17.1°C	16.8°C	16.3°C	16.0°C
Mean Temperature (CDV sensor)	16.24°C	16.23°C	16.17°C	15.82°C

Hour (2 Aug)	15:30	16:30	17:30	18:30
CDV Depth (Tide Table)	0.74m	0.71m	0.64m	0.36m

We can see that over the full deployment there was a constant tilt of 4 degrees from the vertical, and an offset of -76.6 degrees from the x-axis, defined as the bisection of transducers 1 and 2. These values were used to rotate the velocity data to obtain a vertical reference frame. Examples of the measured velocities are shown in Figure 5.C.1. The small magnitude and variability of these values is consistent with the observed conditions of low or nonexistent turbulence and small amplitude wave field.

The mean temperature compares well with the bucket temperature, but the 44 Hz measured temperature, shows some high gradients (as is shown in Figure 5.C.2) not correlated with the vertical velocities, suggesting high horizontal stratification. The strong and sharp variations of temperature, by itself, suggest horizontal advection of warm patches of water. This hypothesis is further discussed in the next section, when the temperature fluxes are discussed.

D. OCEAN FLUXES AND STRATIFICATION

Figures 5.D.1 to 4, show the spectral evolution of temperature and of the 3 velocity components. The frequency

density units of all spectral quantities are such that the integration over the full frequency range gives the total variance. These spectra are characterized by a broad peak, more evident in the velocity spectra, at frequencies between 0.2 and 0.6 Hz. They represent short period, surface gravity waves, with wavelengths of the order of 6 m with e-folding

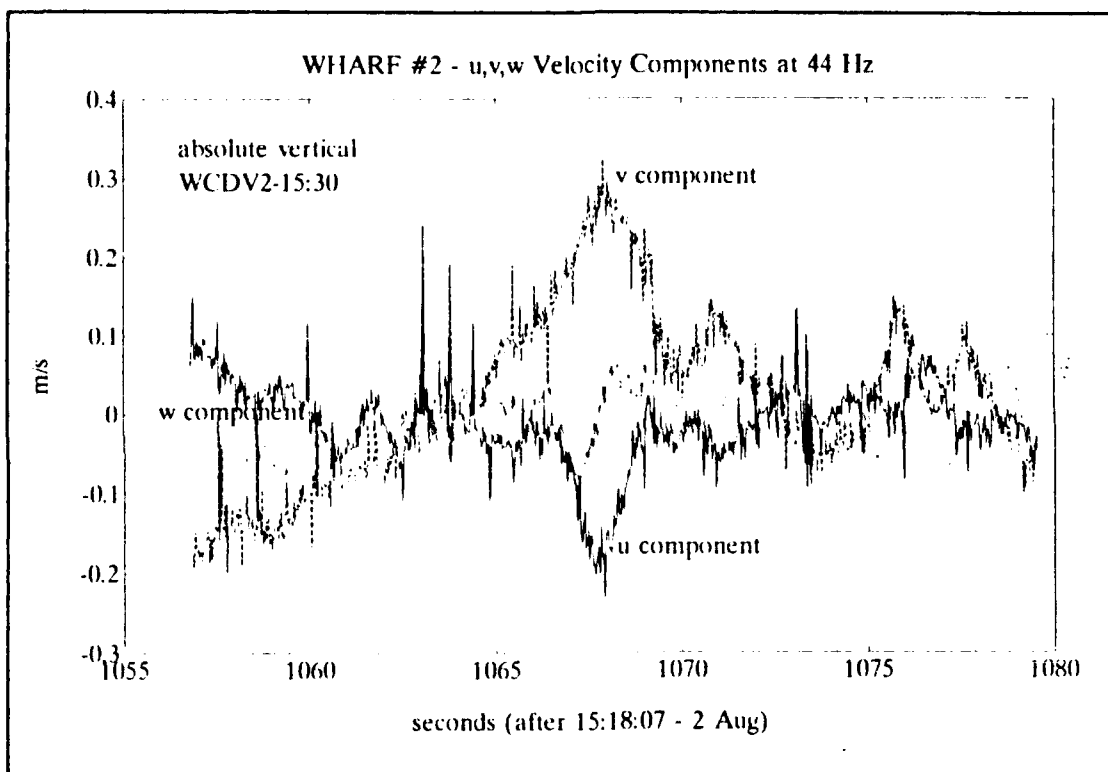


Figure 5.C.1 - Wharf #2 Experiment: Velocity data, sampled at 44 Hz.

depths of the order of 1 m (i.e. deep water waves). This fact is consistent with the observed similar energy content in the vertical and horizontal velocity components ($10^{-4} \text{ (m/s)}^2/\text{Hz}$). The broad band shape of the spectrum suggests that this energy

is due to wind waves starting to shoal, probably generated in the near field.

There are also three peaks, possibly associated with low frequency swell or seiche, at the frequencies of: 2.5×10^{-2} Hz, 4.5×10^{-2} Hz and 7×10^{-2} Hz: these spectral peaks can be seen in the figure 5.D.5, which shows the high resolution spectra of the variables at 1530. These peaks are more noticeable in the

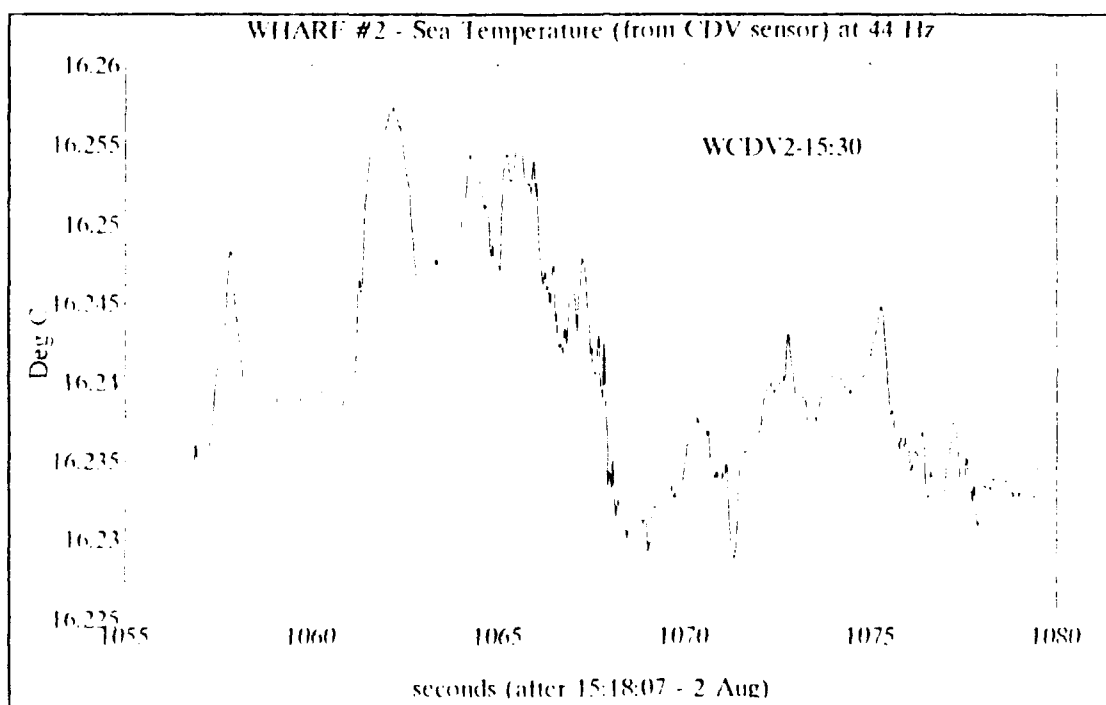


Figure 5.C.2 - Wharf #2 Experiment: Temperature data, sampled at 44 Hz.

spectra of the horizontal velocity, significant to a 80% confidence level, and are highly attenuated in the vertical velocity spectra as we can expect for a shallow water wave. These harmonically related frequencies suggest weak non-linear interactions (resonance), with energy being transferred,

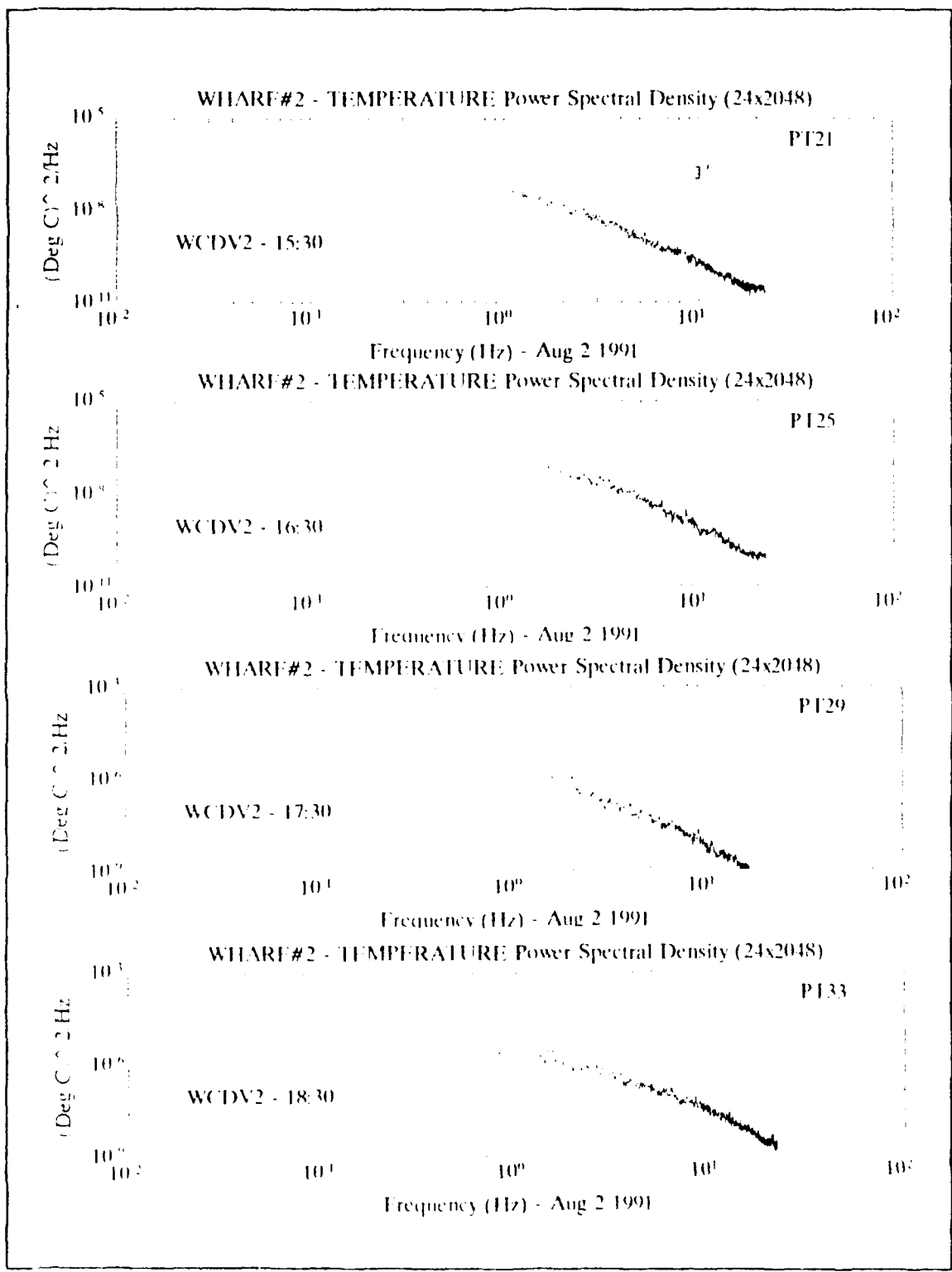


Figure 5.D.1 - Wharf #2 Experiment - Spectral evolution of temperature.

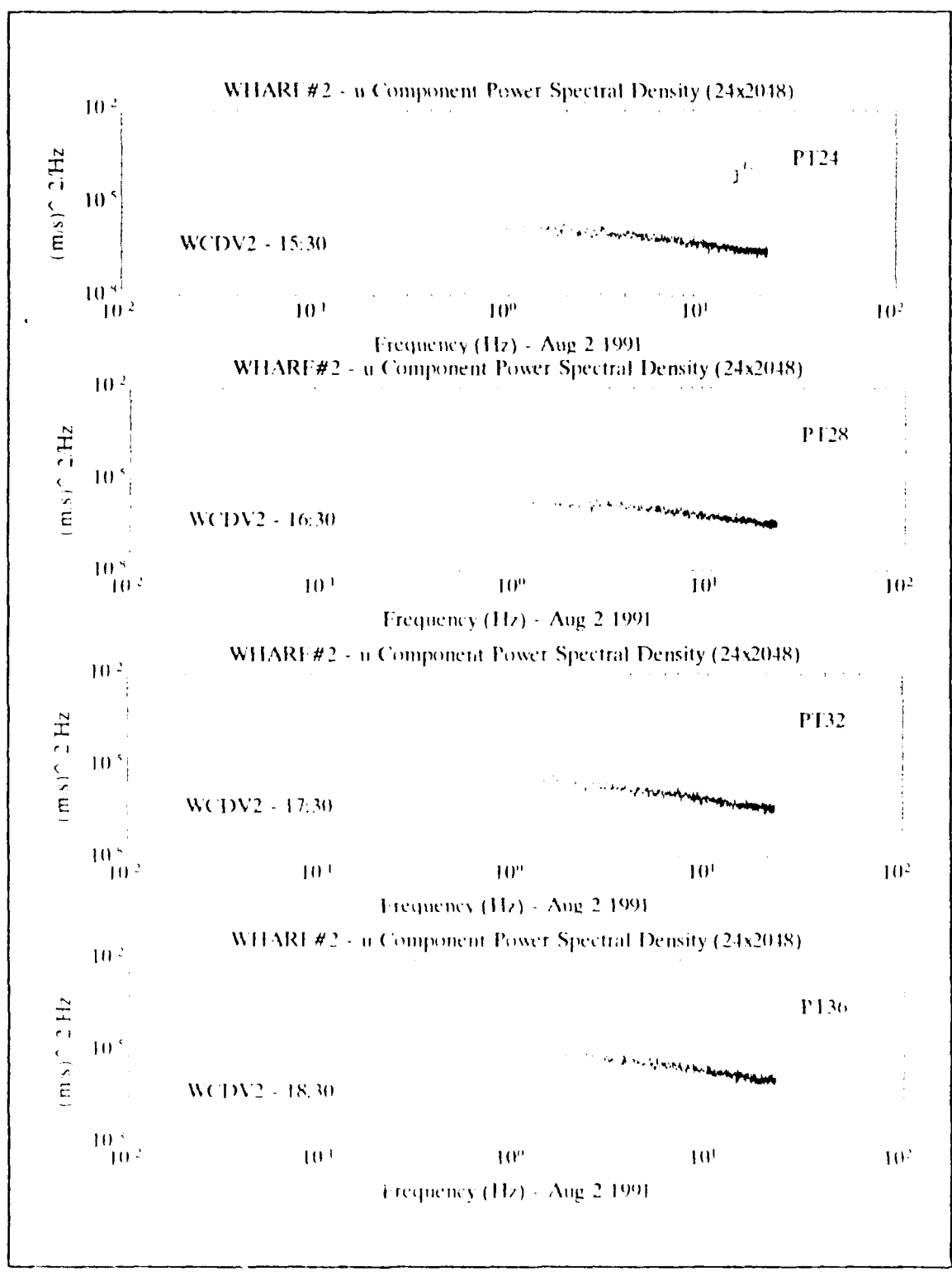


Figure 5.D.2 - Wharf #2 Experiment - Spectral evolution of u-velocity.

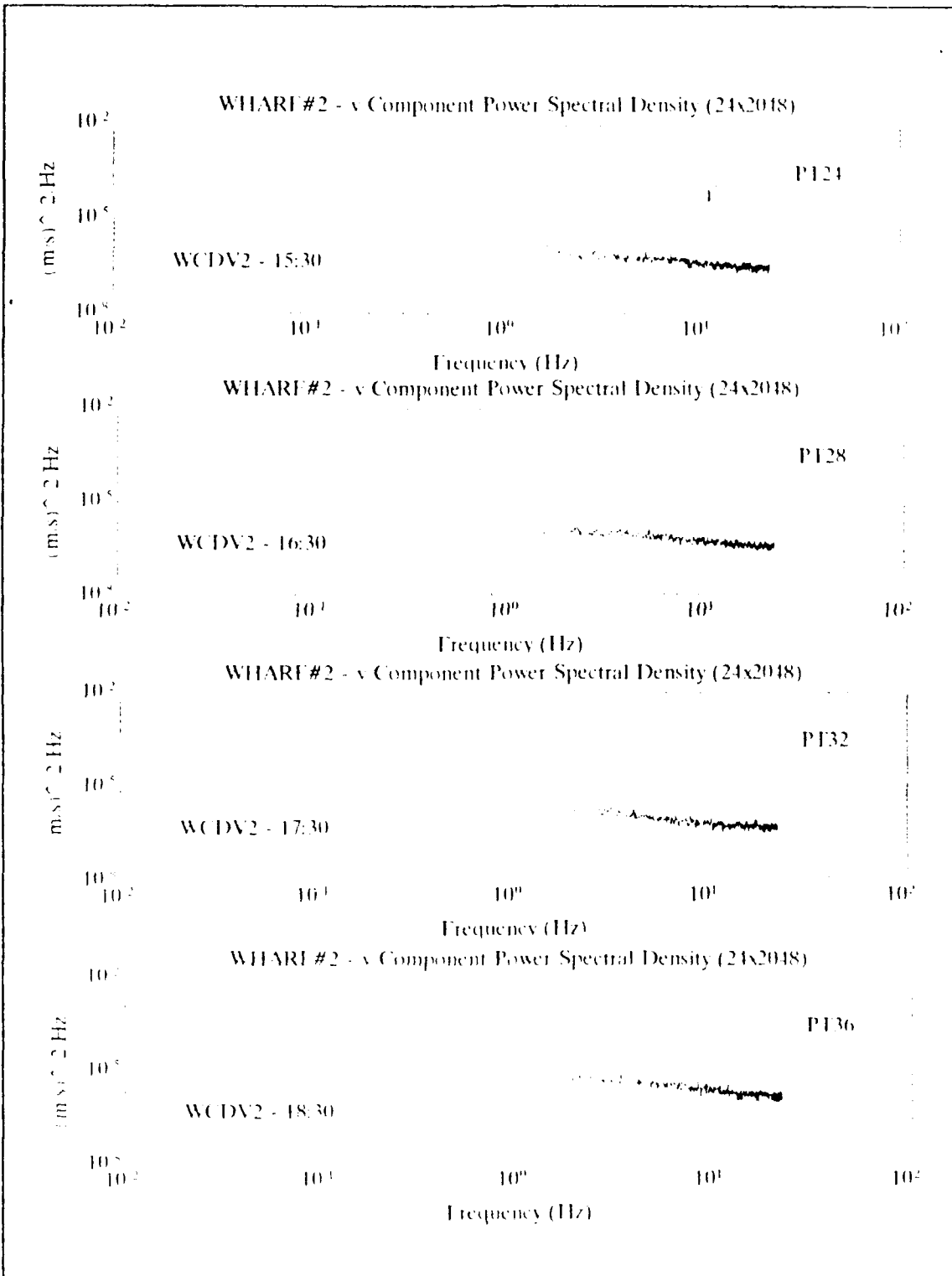


Figure 5.D.3 - Wharf #2 Experiment - Spectral evolution of v-velocity.

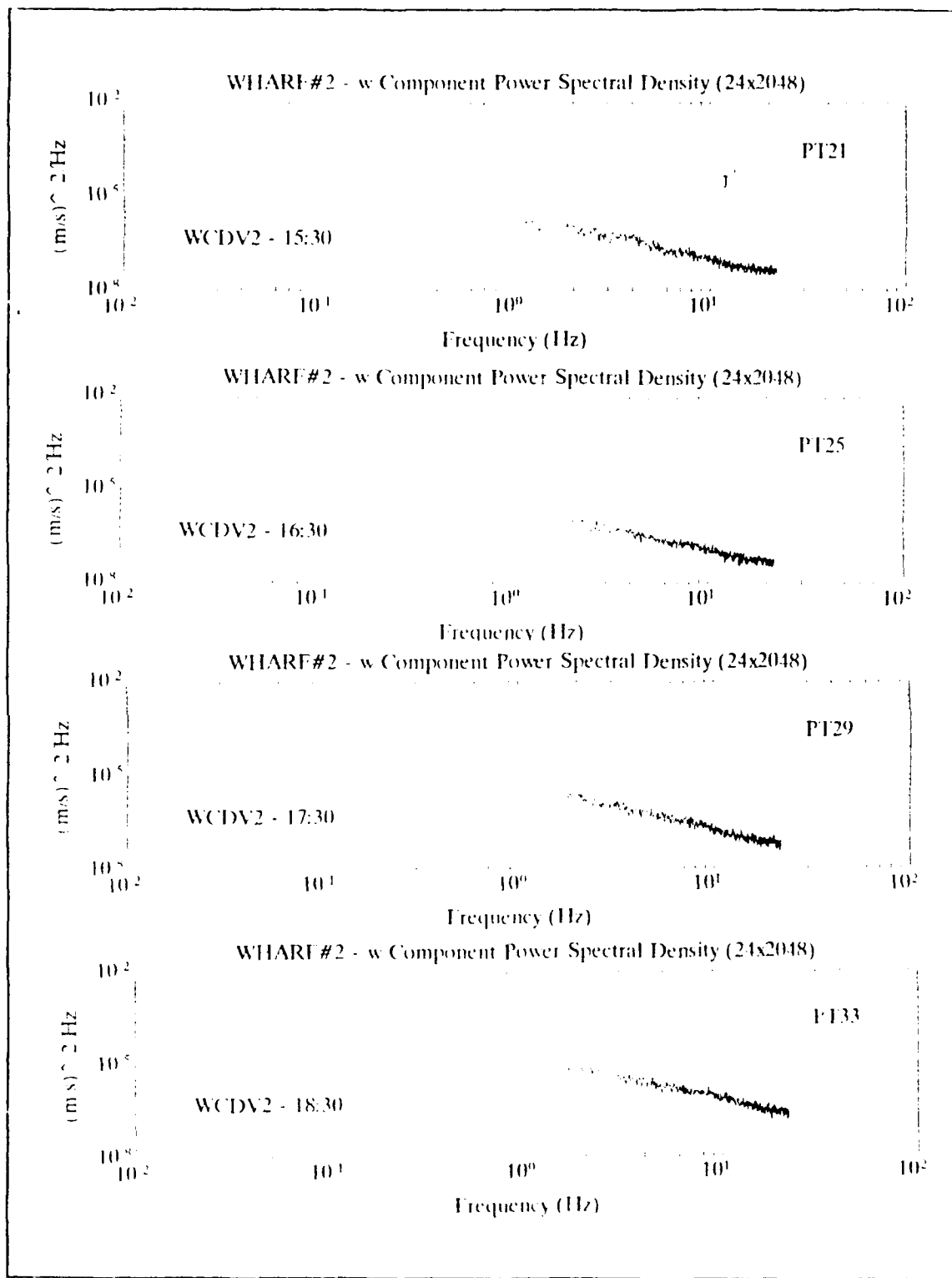


Figure 5.D.4 - Wharf #2 Experiment - Spectral evolution of w-velocity.

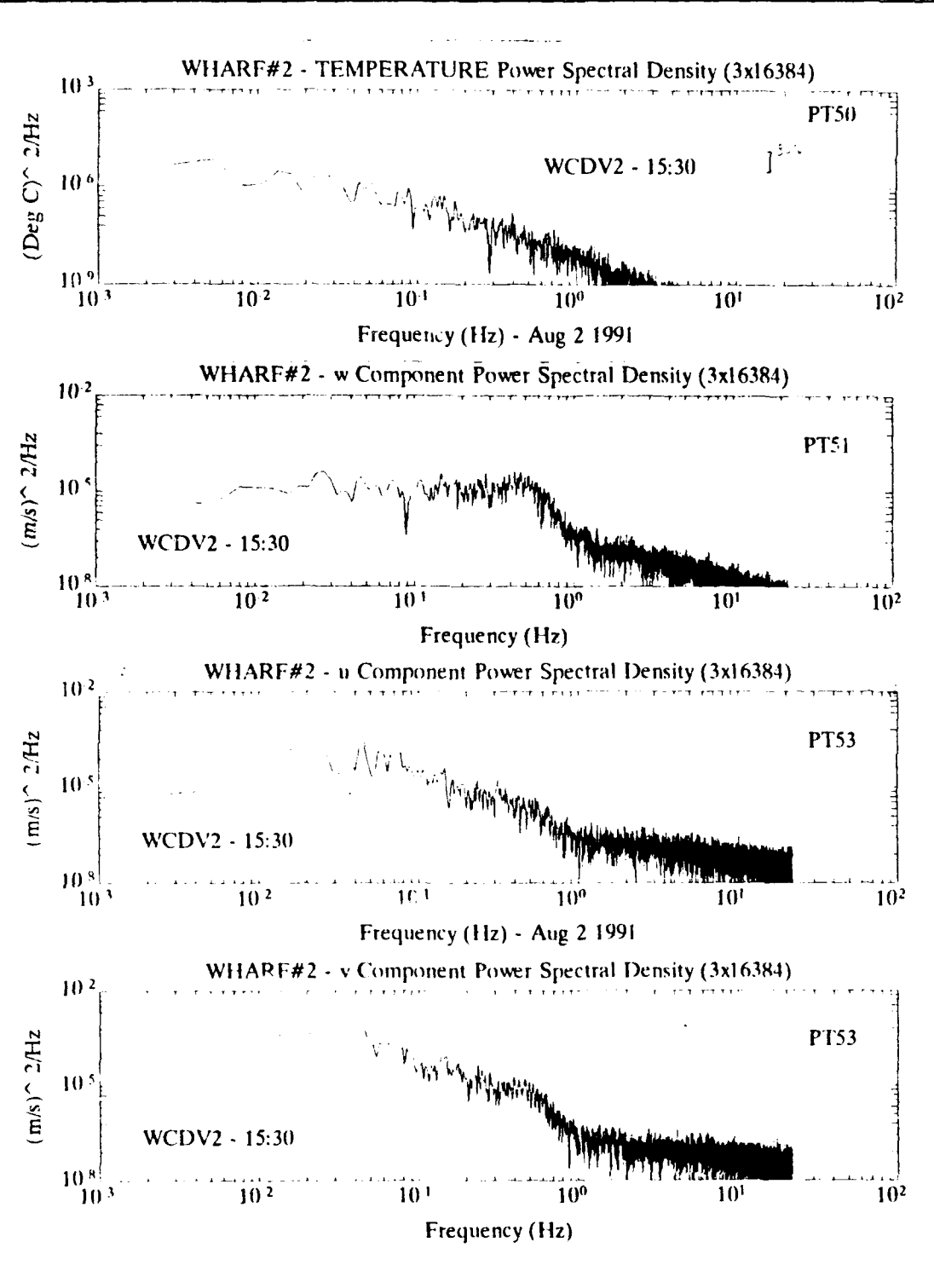


Figure 5.D.5 – Wharf #2 Experiment – High resolution spectra at 15:30.

between the different waves components. If ressonance is occurring, these components will contribute to the presence of stresses in the upper layer.

Besides telling us that the velocity field was dominated by the surface gravity waves, the low energy levels at high frequencies also shows the noise floor of the instrument with energy density on the order of 10^{-7} $(\text{m/s})^2/\text{Hz}$ in the velocity spectra, and 10^{-10} $(\text{Deg C})^2/\text{Hz}$ in the temperature spectra. This value represents noise significant velocities of the order of 0.005 m/s, that are smaller than typical velocities associated with active oceanic turbulence, typically of the order of 0.01 m/s [Ref.22]. Therefore, for turbulent flux observations we should expect to obtain good SNR performances with this instrument.

Integrating the velocity spectra, we obtain the kinetic energy for each ensemble. These values and their evolution over the 4 analyzed hours are important in the characterization of the observed fields. We can see that the total horizontal kinetic energy was significantly larger than the vertical, due to the nature of the wave fields.

TABLE 7 - KINETIC ENERGIES

HOURS	15:30	16:30	17:30	18:30
w-component (m^2/s^2)	0.0035	0.0040	0.0073	0.0179

HOURS	15:30	16:30	17:30	18:30
u-component (m^2/s^2)	0.0044	0.0049	0.0062	0.0119
v-component (m^2/s^2)	0.0107	0.0118	0.0149	0.0238

In order to compute and interpret the fluxes of temperature and the Reynolds stresses, the co-spectra, phase spectra and coherence were computed for the several combinations of variables. Using Parseval theorem [Ref.14], integrating the co-spectra over frequency provides estimates of the scalar fluxes or the Reynolds stresses. Therefore, the co-spectrum will tell us how these fluxes are distributed over frequency. In figures 5.D.6, 7.a, 7.b and 7.c, we can see the evolution of the co-spectrum between the perturbed quantities of the temperature (t') and vertical velocity component (w') hereafter designated by $t'w'$, and between the three velocity components $u'w'$, $v'w'$ and $u'v'$. The low values in the co-spectrum and the negligible energy above 1 Hz are characteristic of a linear wave field with low turbulence levels.

The negative peak found at the very low frequency range in the co-spectrum of the horizontal velocity components, Figure 5.D.7.a, confirms the presence of non-linear interactions

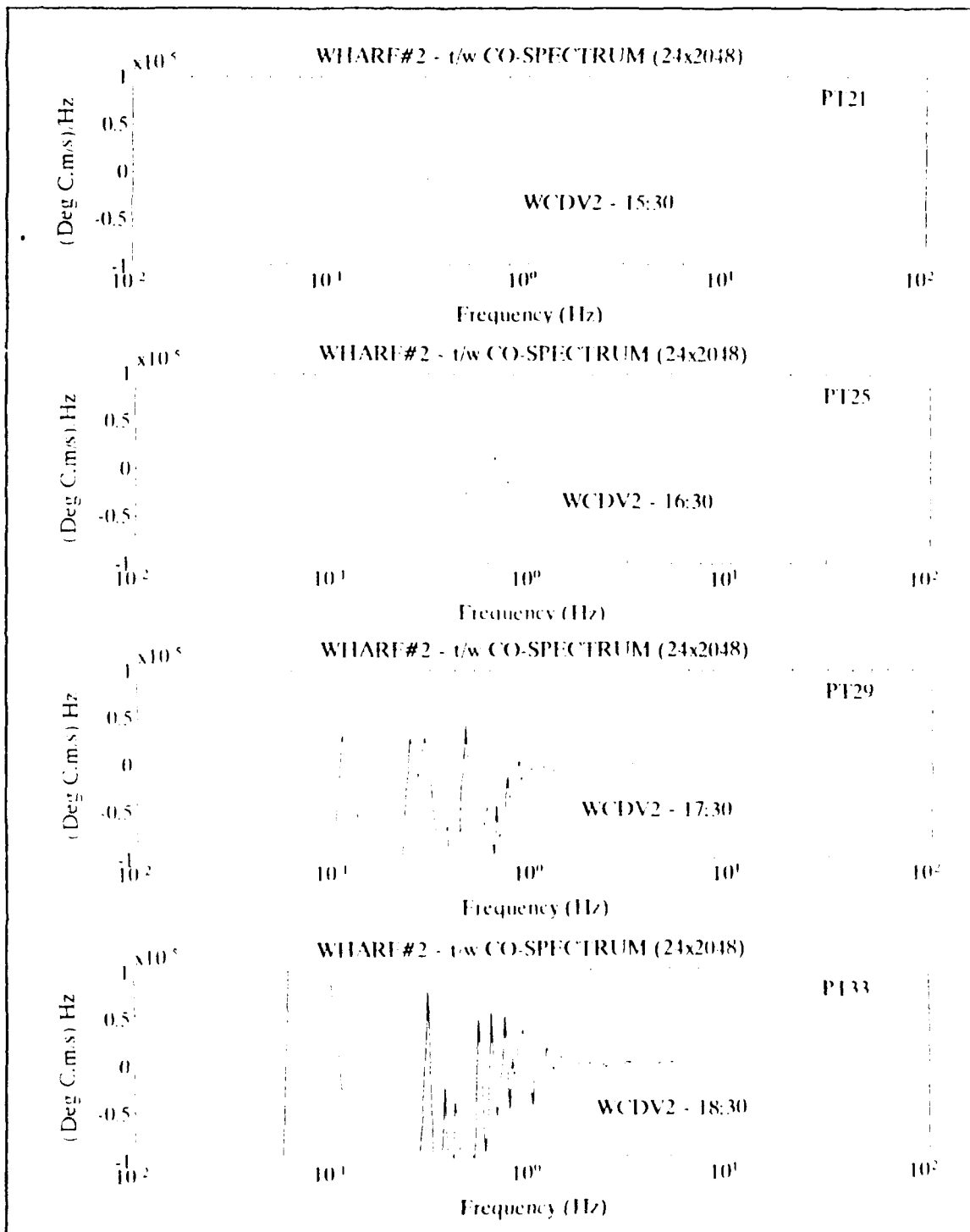


Figure 5.D.6 - Wharf #2 Experiment - Time evolution of the co-spectrum, between temperature and vertical velocity

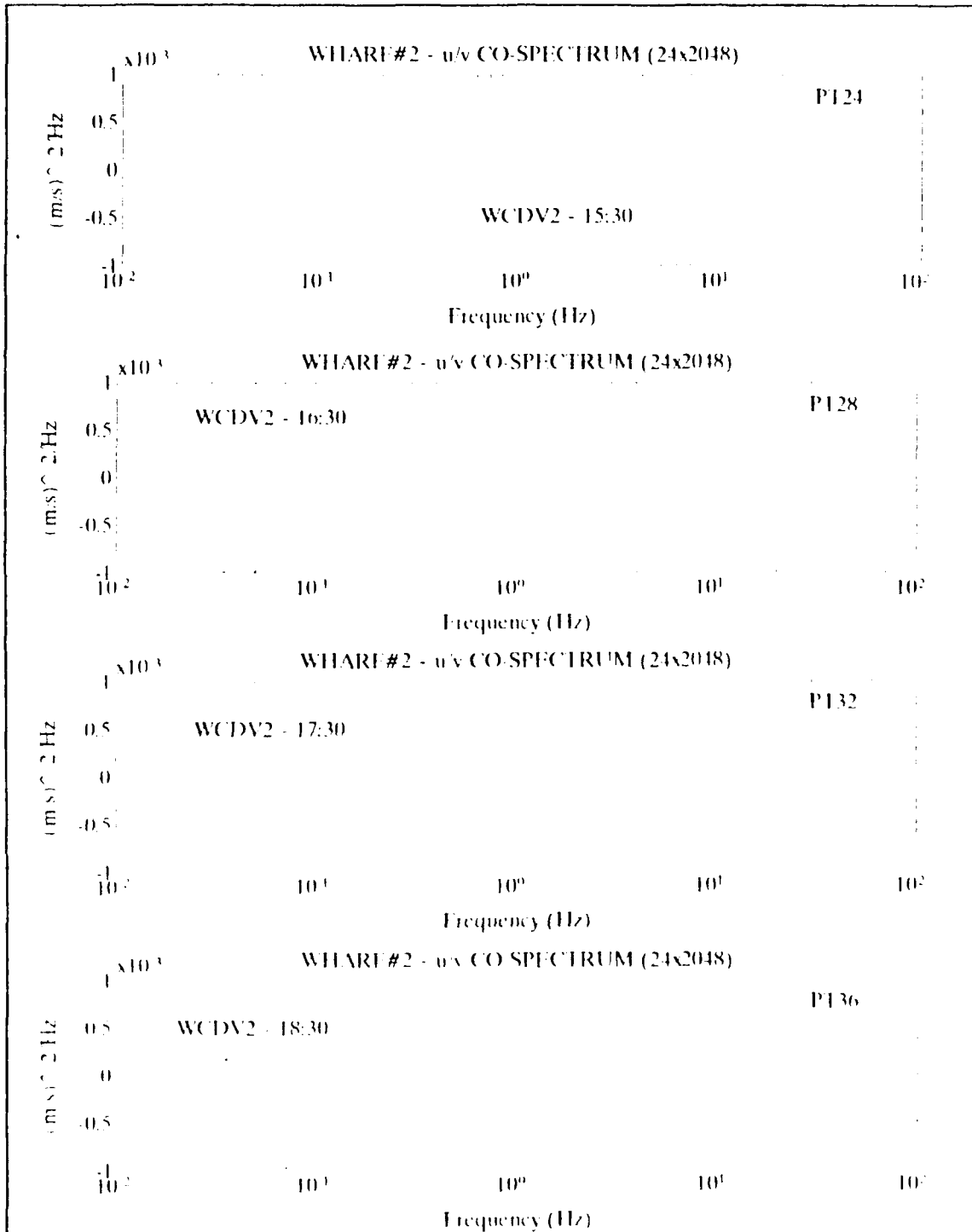


Figure 5.D.7.a – Wharf #2 Experiment – Time evolution of the co-spectrum, between horizontal velocity components

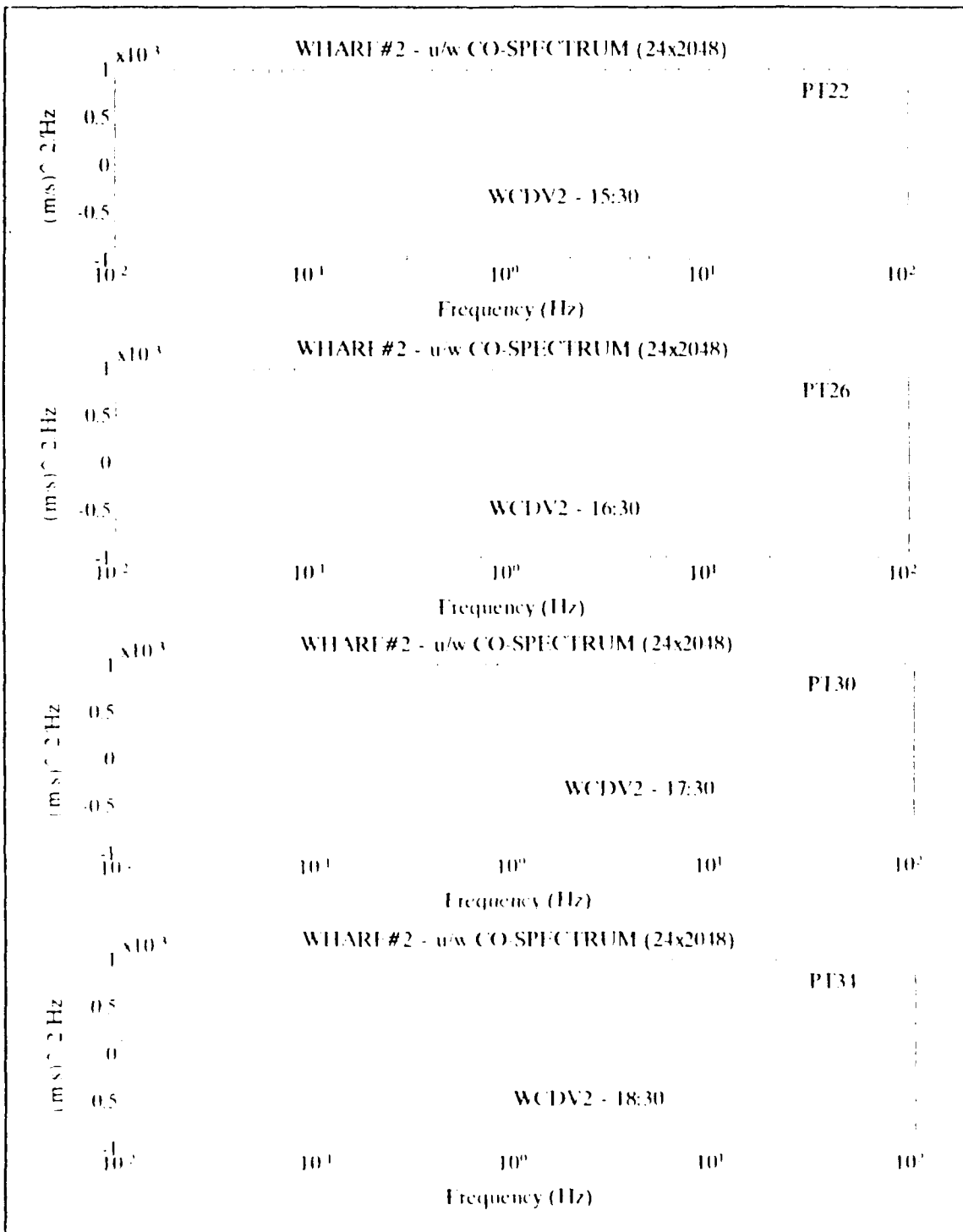


Figure 5.D.7.b - Wharf #2 Experiment - Time evolution of the co-spectrum, between u and w velocity components

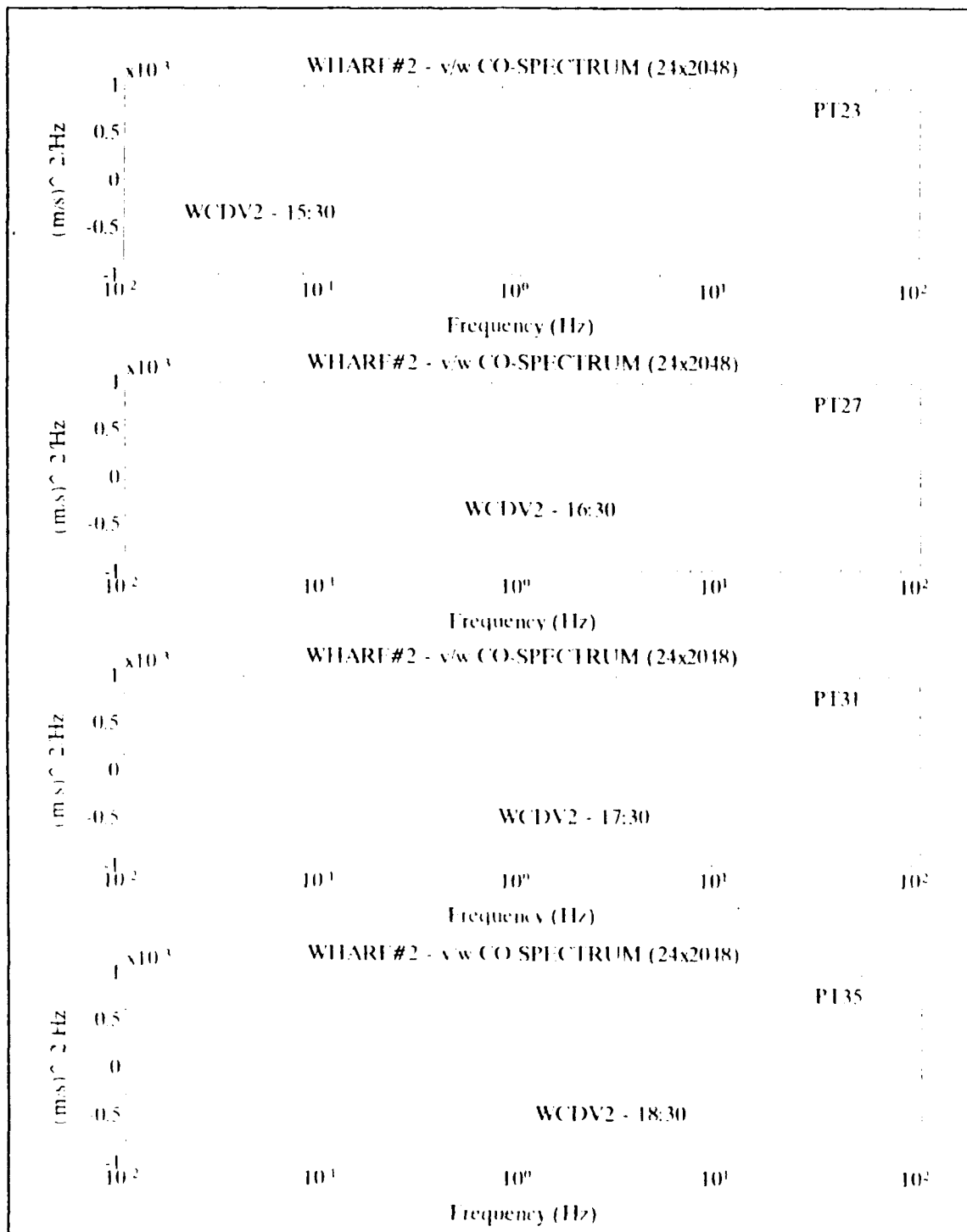


Figure 5.D.7.c - Wharf #2 Experiment - Time evolution of the co-spectrum, between v and w velocity components

between harmonically related wave components [Ref.23], as suggested by the velocity spectra in Figure 5.D.5.

The co-spectra of temperature and vertical component of the velocity, shows that the thermal energy flux is negative in the short period wave range (deep water waves), and positive over the long period waves range at the 1530 and 1630 hours. Later energy starts cascading into the smaller scales, where previously the co-spectral density was almost zero (Figure 5.D.6). This is partially consistent with an increase in the horizontal momentum flux, though it remains restricted in the low frequency range. No significant changes are seen in the vertical momentum flux. This picture suggests that after the 1730, due to the shallow depth of the instrument and to the reduction of insolation generated stratification, turbulent levels tend to increase.

After integrating equivalent estimates for each data set, the time evolution of the temperature fluxes and stresses were calculated:

TABLE 8 - TEMPERATURE AND MOMENTUM FLUXES

HOURS	15:30	16:30	17:30	18:30
$\langle u'v' \rangle$ (m^2/s^2)	-0.0046	-0.0051	-0.0063	-0.0108
$\langle u'w' \rangle$ (m^2/s^2)	-0.0001	-0.0000	0.0002	0.0015

HOURS	15:30	16:30	17:30	18:30
$\langle v'w' \rangle$ (m^2/s^2)	0.0011	0.0014	0.0020	0.0012
$\langle t'w' \rangle$ ($m \cdot ^\circ C/s$)	-2.2277 $\times 10^{-5}$	-1.0943 $\times 10^{-5}$	-2.5964 $\times 10^{-5}$	-10.5082 $\times 10^{-5}$

This table shows that the Reynolds stresses and temperature fluxes slightly increased with time, as stratification was decreasing.

The phase spectra and coherence are tools that help the interpretation of the co-spectrum. The phase spectra quantify the phase lags between variables, showing departures from the in-phase components shown in the co-spectra. These spectra are useful in the identification of quadrature conditions, characterizing linear wave components, and in the analysis of non-linear characteristics. The coherence spectrum shows whether cross-spectral components have constant phase relationships in time. For linear wave fields, coherence should be high, near 1 (no fluxes or stresses), while for turbulent or non-linear fields the coherence should have low values. Examples of these estimates are shown in the figures 5.D.8 and 9 for the temperature vertical flux and Reynolds stresses at 1530. The features shown in these figures are similar to the characteristics of the other data sets, with

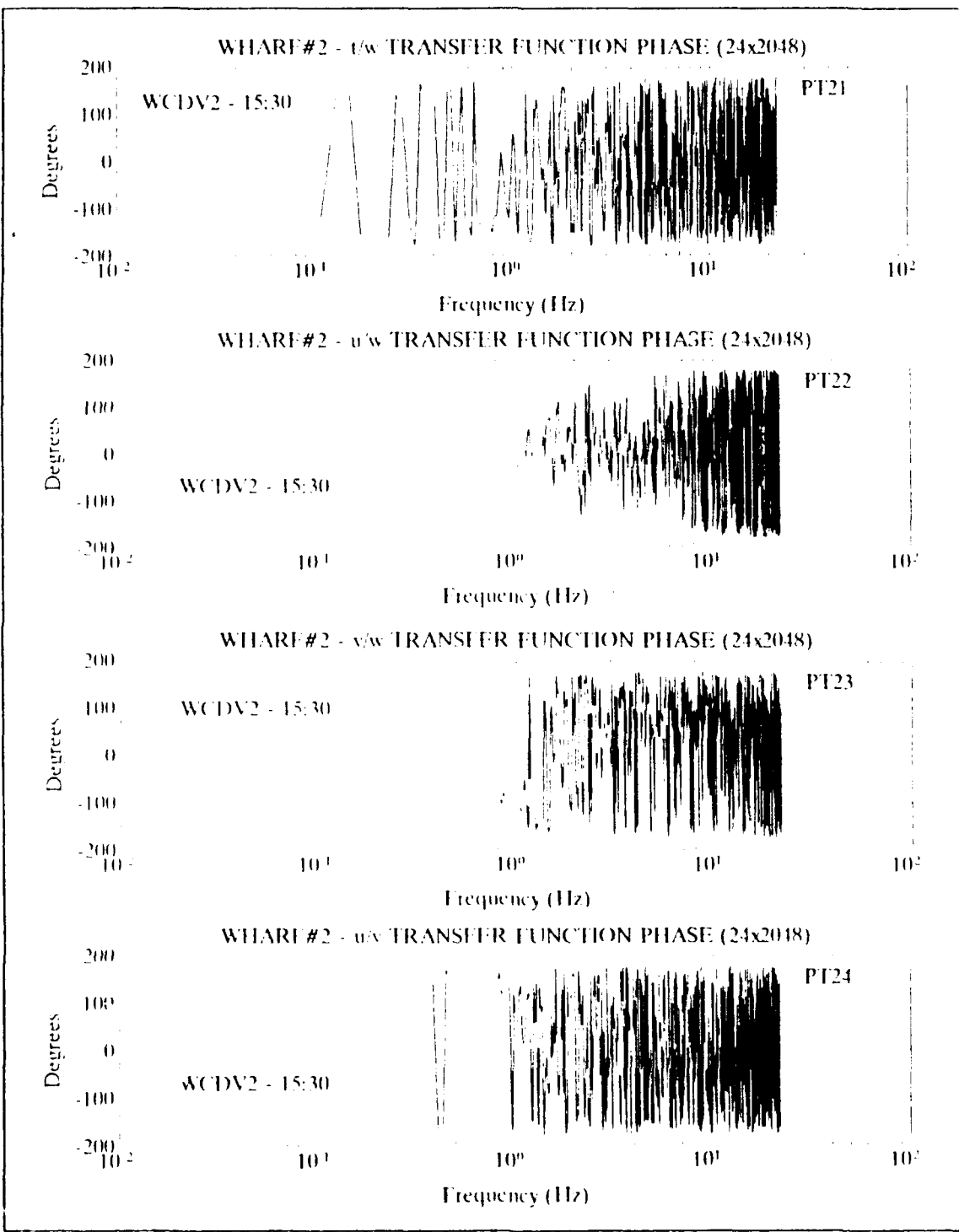


Figure 5.D.8 - Wharf #2 Experiment - Phase spectra between velocity components and temperature at 15:30.

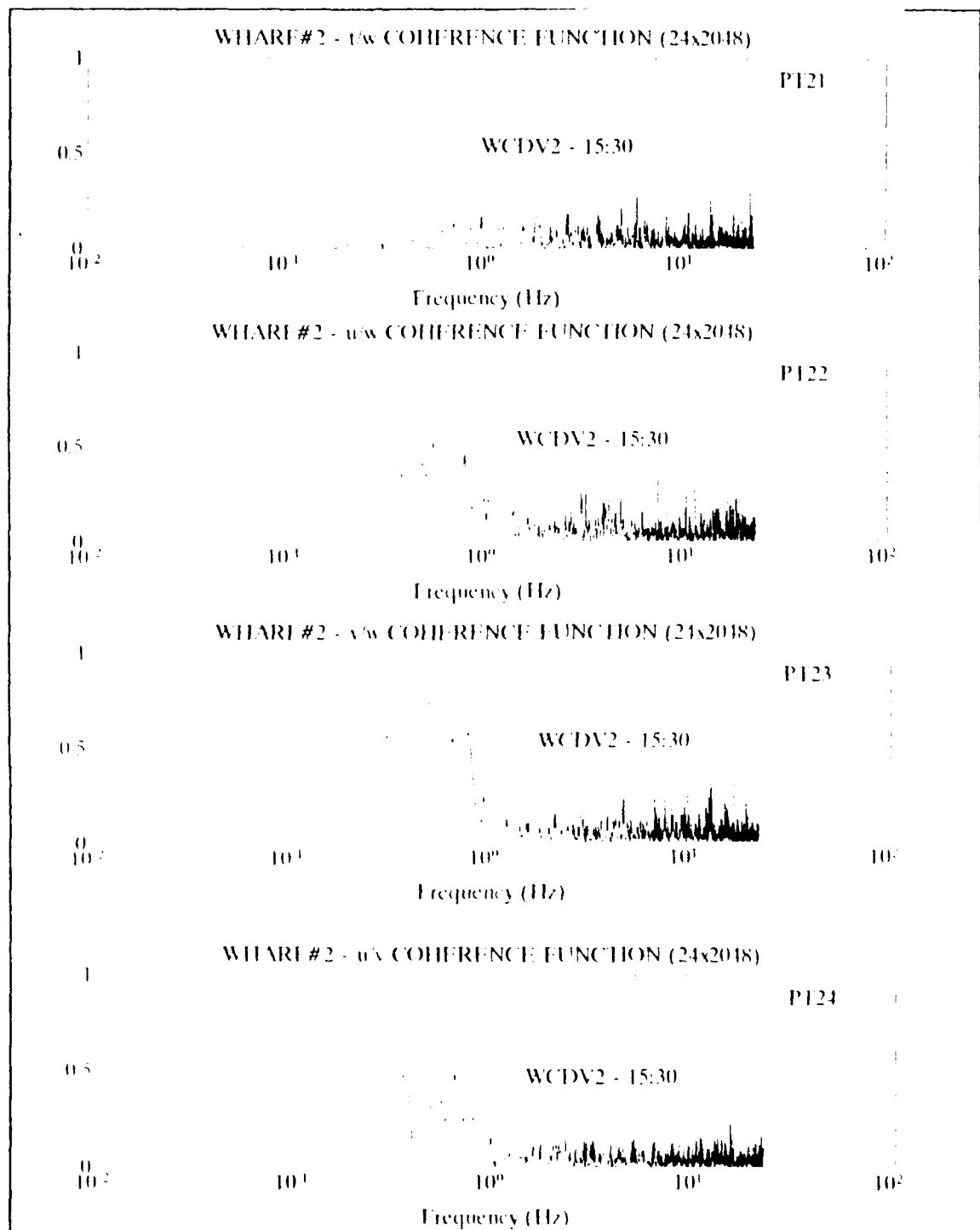


Figure 5.D.9 - Wharf #2 Experiment - Coherence of velocity components and temperature at 15:30.

quadrature phase and high coherence through the spectral peaks range, as expected for a linear wave field.

The low correlation between temperature and vertical velocity hint that we cannot explain the observed temperature variability only from the vertical stratification, in which water is pumped up and down past the sensor following the wave orbital motion. On other hand, if we assume that horizontal stratification exists, then the horizontal velocities may explain this variability, with patches of warmer or colder water being advected by the mean horizontal flow and wave orbits. To test this hypothesis, the horizontal temperature fluxes were computed as is shown in the figure 5.D.10 for the 1530 data set. In fact, they do not show a stronger correlation; however, the probable high variability on the horizontal density gradient will introduce an additional effect on these estimates. These estimates may also be misleading if not computed from sufficiently long averaging intervals as the sensor was stationary in the field.

The coherence spectra(Figure 5.D.9) again reinforce the fact that the wave regime at the middle frequencies has a linear character, showing high coherence between v and w within this range. These characteristics are maintained throughout the observation period. Similarly, the coherence between the horizontal components of velocity is more significant in the low frequency wave range, but with slightly lower values.

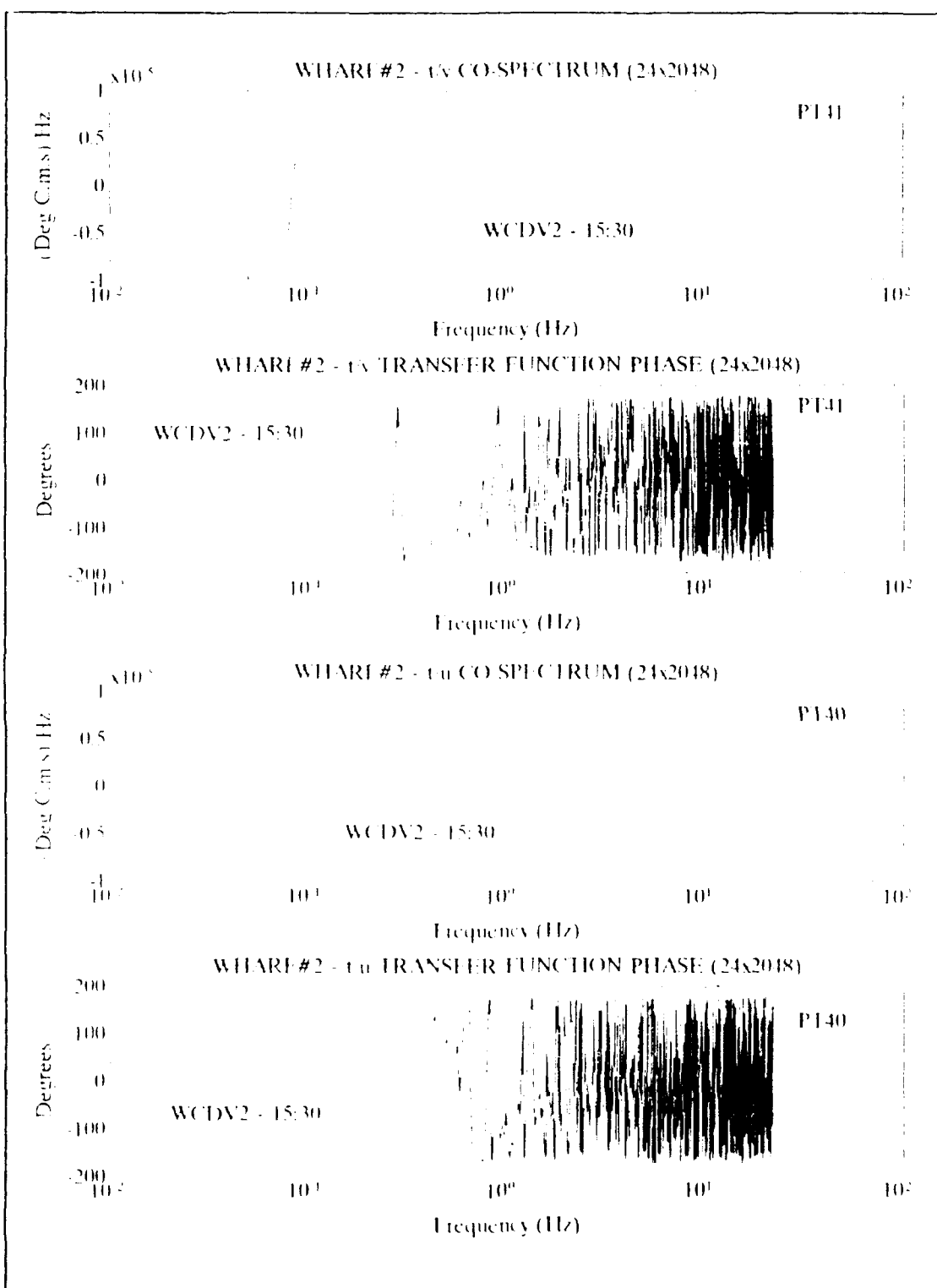


Figure 5.D.10 - Wharf #2 Experiment - Horizontal fluxes of temperature at 15:30.

VI. CONCLUSIONS

The need to explicitly observe turbulent processes arises from a wide class of problems in physical oceanography, as described in the review in chapter II. The CDV package was developed to simultaneously measure temperature, conductivity, pressure, shear and the 3 components of velocity at sub-centimeter scales.

The unique measurement techniques used in this instrument require special data processing and analysis methods. The three component velocity estimations rely on a doppler frequency spectral estimator, working in real-time, that must use a small number of coherently sampled data points. In order to choose the most suitable algorithm, and to assess its physical limitations, Monte-Carlo simulations were performed using several possible spectral estimators. From these simulations, the Pulse Pair algorithm, or equivalently the MUSIC order 2 algorithm, showed the best performance, followed by the Peak FFT algorithm. The FFT estimator, corresponds to a maximum likelihood estimator, but suffers from the fact that for a small number of points, the discretization errors are very dominant, and it's performance is seriously degraded. Using these results, the Pulse Pair estimator was implemented, together with the pre-processing of the other measured

quantities, on a Digital Signal Processor for real-time pre-processing and review.

To test the CDV software and hardware, the equipment was deployed for the first time off Monterey Wharf #2, on the 2 and 3 of August 1991, along with measured environmental conditions. This first analysis showed that the performance of the bistatic velocity estimation is below that expected, with some conspicuous spikes superimposed on valid data. By introducing a change in the transmitting cycles of the transducers this problem should be overcome in future deployments. The calibration of the other scalar variables and acceleration gave good results. To deglitch the bistatic doppler frequencies and increase its confidence, we used the redundancy in the velocity components observations, with two independent estimates from each of the two reciprocal acoustic bistatic paths. An adaptative procedure was developed, relying on a one lag linear-predictor and predictively choosing the best estimate of the doppler frequency. This procedure significantly improved the SNR of the velocity estimates.

The CDV Wharf data shows a surface gravity wave field with energy in two different ranges, superimposing near field generated high frequency wind waves with a low frequency swell. The wind waves show the expected characteristics of deep water waves while the low frequency waves clearly have shallow water waves characteristics. The high resolution spectra and the co-spectra show that resonance interactions

may be occurring at the low frequency range. The high frequency wind waves show a stronger coherence and do not contribute significantly to the momentum flux, but nevertheless the major contribution to the temperature flux occur over these frequency ranges.

The fact that the observed temperature variability did not correlate well with the measured vertical velocity, even at the deep water wave frequency range, suggest that an irregular horizontal stratification existed, with pools of warm or cold water being advected past the sensor, by the wave orbits and mean flow.

From the vertical velocity and temperature co-spectra analysis, we also observed an increase in the temperature flux associated with a shallow depth and reduction in the vertical stratification, following the decrease in the solar heating after 1730. However, due to remaining significant stratification no significant turbulence develops, as we can observe in the co-spectra of the velocity components.

At the high frequency ranges, we did not find significant energy due to the absence of strong turbulence, allowing the instrumentation noise floor to be seen. This noise floor represents velocities in the order of 0.005 m/s, values below the ones that we should expect to find during strong turbulent conditions. Because this data was the first that was analyzed with this equipment, we expect in future deployments to improve the SNR in the velocity measurements by an order of

magnitude by reducing the acoustic noise component 5 to 10 times and altering acoustic sampling methods. However, the existing noise floor is already below the minimum requirements for studying energetic turbulence.

The CDV data seems consistent with the observed environmental conditions, confirming the expected capabilities of the instrument to observe real data, including wind wave fields, and showing the noise limitations that we should expect when observing turbulence fields. However, in order to further study its precision, this data should also be compared with simultaneous observations of the ocean variables measured by independent instruments. The CDV package will be able to perform simultaneous measurements of oceanographic variables at the sub-centimeter scales, determining all terms in the Reynolds equations. This should improve our characterization of turbulent fields, with applications in a variety of oceanographic turbulence problems. These applications will be explored using the instrument in a loose-tethered profiling mode.

LIST OF REFERENCES

1. Tennekes, H., and Lumley, J.L., First Course in Turbulence, MIT Press, 1972
2. Stull, R.B., Boundary Layer, Kluwer Academic Publishers, 1988
3. Cavaleri, L., and Zecchetto, S., Reynolds Stresses Under Wind Waves, J. Geophys. Res., Vol. 92, 3894-3903, 1987
4. Lumley, J.L., and Terray, E.A., Kinematics of Turbulence Convected by a Random Wave Field, J. Phys. Oceanogr., Vol. 13, 2000-2007, November 1983
5. Gill, A.E., Atmosphere-Ocean Dynamics, Academic Press, 1982
6. Pond, S. and Pickard, G.L., Introductory Dynamical Oceanography, 2nd Edition, Pergamon Press, 1989
7. Garwood, R.W., An Oceanic Mixed Layer Model Capable of Simulating Cyclic States, J. Phys. Oceanogr., Vol. 7, 455-468, May 1977
8. Dewey, R.K. and Moum, J.N., Enhancement of Fronts by Vertical Mixing, J. Geophys. Res., Vol. 95, C6, 9433-9445, June 1990
9. Brink, K.H., The Near-Surface Dynamics of Coastal Upwelling, Prog. Oceanogr., Vol. 12, pp 223-257, 1983
10. Moum, J.N., Caldwell, D.R. and Stabeno, P.J., Mixing and Intrusions in a Rotating Cold-Core Feature off Cape Blanco, Oregon, J. Phys. Oceanogr., Vol. 18, 823-833, June 1988
11. Send, U., Beadsley, R.C. and Winant, C.D., Relaxation From Upwelling in the Coastal Ocean Dynamics Experiment, J. Geophys. Res., Vol. 92, C2, 1683-1698, February 1987
12. Dillon, T.M., and Caldwell, D.R., The Batchelor Spectrum and Dissipation in the Upper Ocean, J. Geophys. Res., Vol. 85, No. C4, pp 1910-1916, April 1980
13. Marple, S.L., Digital Spectral Analysis with Applications, Prentice-Hall. Inc., 1987

14. Jenkins, G.M., and Watts, D.G., Spectral Analysis and Its Applications, Holden-Day Inc., 1968
15. Kay, S.M., Modern Spectral Estimation, Prentice Hall, 1988
16. Miller, K.S., and Rochwarger, M.M., A Covariance Approach to Spectral Moment Estimation, IEEE Trans. Info. Theory, Vol. it-18, No. 5, September 1972
17. Landing, L., Spectral Analysis versus Counting, DANTEC U.S., pp 189-196, 1984
18. Kendem, B., Spectral Analysis and Discrimination by Zero-Crossings, Proc. of IEEE, Vol. 74, No. 11, November 1986
19. Caldwell, D.R., Dillon, T.M., and Moum, J.N., The Rapid-Sampling Vertical Profiler: An Evaluation, J. Atmosph. and Oceanic Technology, Vol.2, No.4, December 1985
20. Lohrmann, A., Hackett, B., and Roed, L.P., High Resolution Measurements of Turbulence, Velocity and Stress Using a Pulse-to -Pulse Coherent Sonar, J. Atmosph. and Oceanic Technology, Vol.7, February 1990
21. Alonso, M., and Finn, E.J., Fundamental University Physics, Addison-Wesley, 1967
22. Moum, J.N., The Quest for K_2 - Preliminary Results from Direct Measurements of Turbulent Fluxes in the Ocean, J. Phys. Oceanogr., Vol.20, No.12, December 1990
23. LeBlond, P.H., and Misak, L.A., Waves in the Ocean, Elsevier Oceanography Series, 1978

INITIAL DISTRIBUTION LIST

- | | | |
|----|--|---|
| 1. | Defense Technical Information Center
Cameron Station
Alexandria, VA 22304-6145 | 2 |
| 2. | Library, Code 52
Naval Postgraduate School
Monterey, CA 93943-5000 | 2 |
| 3. | Chairman (Code OC/Co)
Department of Oceanography
Naval Postgraduate School
Monterey, CA 93943-5000 | 1 |
| 4. | Chairman (Code MR/Hy)
Department of Meteorology
Naval Postgraduate School
Monterey, CA 93943-5000 | 1 |
| 5. | E.B. Thornton (Code OC/Tm)
Department of Oceanography
Naval Postgraduate School
Monterey, CA 93943-5000 | 1 |
| 6. | T.P. Stanton (Code OC/St)
Department of Oceanography
Naval Postgraduate School
Monterey, CA 93943-5000 | 4 |
| 7. | Emanuel Ferreira Coelho
Department of Oceanography
Naval Postgraduate School
Monterey, CA 93943-500 | 1 |
| 8. | Office of Naval Research (Code 420)
Naval Ocean Research and Development
Activity
800 N. Quincy Street
Arlington, VA 22217 | 1 |
| 9. | Director Tecnico
Instituto Hidrografico
Rua das Trinas 49
1296 Lisboa CODEX
Portugal | 1 |

10. Fundacao Calouste Gulbenkian
Servico de Bolsas de Estudo
1093 Lisboa CODEX
Portugal

1